EXPERIMENTAL AND MOLECULAR DYNAMICS STUDIES IN COPPER ELECTRO CHEMICAL MECHANICAL POLISHING (Cu-ECMP)

By

ANANT KANDASAMY ARULMOZHI

Bachelor of Engineering in Mechanical Engineering

Anna University

Chennai, India

2011

Submitted to the Faculty of the
Graduate College of the
Oklahoma State University
in partial fulfillment of
the requirements for
the Degree of
MASTER OF SCIENCE
July, 2013

EXPERIMENTAL AND MOLECULAR DYNAMICS STUDIES ON COPPER ELECTRO CHEMICAL MECHANICAL POLISHING (Cu-ECMP)

Thesis Approved:

Dr. Satish T S Bukkapatnam

Thesis Adviser

Dr. Lionel Raff

Thesis Co-Advisor

Dr. Zhenyu (James) Kong

Committee Member

Dr. Sandip Harimkar

Committee Member

ACKNOWLEDGEMENTS

The word "Acknowledgement" may not be the perfect word to express my thankfulness to three most brilliant and iconic personalities, who have given me a model to live life by—the late Dr. Ranga Komunduri, Dr. Lionel M. Raff, and Dr. Satish T. S. Bukkapatnam. Although Dr. Komunduri is not here with us, his memories will always be with us and keep us going further. I feel honored and privileged to work in this project started by Dr. K. Secondly, I would like to express my sincere gratitude to my adviser, Dr. Bukkapatnam, whose endless patience and encouragement motivated me to complete this work successfully, without giving it up at any time. I am so grateful to him for spending countless hours of his valuable time in mentoring and guiding me through some of the toughest moments during this work. Next, I would like to thank my co-advisor, Dr. Raff, without whom completing this work would have been a nightmare for me. I thank him from the bottom of my heart for helping me bring this work to fruition and tolerating me and resolving all my doubts in the simplest way I can understand. I would like to thank Dr. Sandip Harimkar and Dr. Zhenyu (James) Kong for agreeing to serve on my committee and for their valuable time and feedback. I would like to thank my colleagues Omer Faruk Beyca, Sakthi Jaya Rahul Ravichandran and Prahalada Krishna Rao, who have always supported me and helped me out through many tough situations. Special thanks to all my research team mates.

Acknowledgements reflect the views of the author and are not endorsed by committee members or Oklahoma State University.

My acknowledgements would be incomplete without thanking my parents, Dr. K. Arulmozhi and Mrs. Shanthi Arulmozhi, for their boundless love, sacrifices, encouragement, blessings, and prayers. I thank my uncle and aunt, Mr. Kumar and Mrs. Nirmala Kumar, for their love and support. Special thanks to Ms. Neethi Murali for her continuous support and encouragement throughout my Master's program.

I would also like to thank all my friends at Stillwater and back home, who have helped me and supported me right from the time I came to the USA and also the School of Industrial Engineering and Management for giving me the opportunity to pursue my Master's degree at Oklahoma State University, Stillwater, OK.

This project is funded by a grant (CMMI-0700680 and CMMI-1000978) from the Manufacturing Processes and Machines of the Division of Civil, Mechanical, and Industrial innovation of the National Science Foundation.

I dedicate this work to the lotus feet of my ***GODDESS ADHIPARASHAKTHI***, who has always been guiding and strengthening me, to my ***Parents*** and to all my ***Gurus*** who have enriched my knowledge right from schooling.

Acknowledgements reflect the views of the author and are not endorsed by committee members or Oklahoma State University.

Name: ANANT KANDASAMY ARULMOZHI

Date of Degree: JULY, 2013

Title of Study: EXPERIMENTAL AND MOLECULAR DYNAMICS STUDIES ON COPPER ELECTROCHEMICAL MECHANICAL POLISHING (Cu-ECMP)

Major Field: INDUSTRIAL ENGINEERING AND MANAGEMENT

Abstract:

In recent times, copper electro chemical mechanical polishing (Cu ECMP) has received a great deal of interest from electrochemists and the semiconductor manufacturing industry. This attention is primarily due to its potential for yielding relatively defect-free surfaces with improved surface integrity compared to chemical mechanical planarization (CMP). In this work, Cu ECMP apparatus integrated with a sensing and data acquisition system was developed to polish Φ4 inch (Φ100 mm) blank Cu wafer surfaces to a finish of R_a< 15nm, and continuously gather voltage and current signals during Cu ECMP process at a sampling rate of 100Hz. Experimental studies were carried out to understand the effects of anodic voltage, pH, and pad pressure on the material removal rate (MRR) and surface roughness (R_a). Understanding the process from an atomistic standpoint helps us gain better control over the process and aids us in optimizing the key process output variables (KPOV). In order to gain a better understanding of the process, the molecular dynamic simulation (MDS) technique was adopted to develop a model to depict the real-time formation of copper (II) hexa-hydrate molecule $\mathrm{Cu}[(\mathrm{H_2O})_6]^{2+}$, which is one of the key elements of the passivation layer formed over the Cu surface during ECMP. The behavior of the complex molecule under an electric force field was simulated to observe the process from a molecular perspective. From the trajectory of Cu^{2+}, it was found that the velocity of copper ion increased with increase in applied voltage. Furthermore, the current carried by a single Cu^{2+} ion was computed based on the applied voltage and velocity of the ion.

TABLE OF CONTENTS

List of Tables... ix

List of Figures... x

I. RESEARCH OVERVIEW AND OBJECTIVES 1

1.1 Significance of electrochemical mechanical polishing process 1

1.2 Mechanics of electrochemical mechanical polishing process.............................5

1.3 Advantages of electrochemical mechanical polishing 9

1.4 Challenges in electrochemical mechanical polishing.......................................10

1.5 Objective statement 11

II. BACKGROUND AND REVIEW OF LITERATURE 13

2.1 Prior experimental investigations into ECMP process mechanisms 13

2.1.1 Effect of electrochemical actions on the process 13

2.1.2 Effect of slurry composition on the process 18

2.2 Elements of the ECMP slurry 30

2.3 Relationship between the KPIV and KPOV in ECMP process 33

2.4 Molecular dynamics (MD) simulation of electrochemical systems 34

2.4.1 General principles in MD simulation..33

2.4.2 Interatomic potentials...35

2.4.3 Calculation of the trajectory and potential energy function 36

2.4.4 MD simulation of metal-water interface..41

III. EXPERIMENTAL STUDY OF Cu ECMP PROCESS 52

3.1 Machine Construction 52

3.1.1 Modifications in the machine design 54

3.1.2 Installation of sensor system..55
3.2 Wafer preparation and cleaning...56
3.3 Measurement of MRR and surface characterization 58
3.4 Experimental results and discussion 60
3.4.1 Influence of pH in the process 62
3.4.2 Effect of anodic voltage 64
3.4.3 Surface texture analysis 67
3.4.4 Characterization of electrochemical regions from I-V curves 69

IV. MOLECULAR DYNAMICS SIMULATION 71
4.1 Description of the molecular system 72
4.2 Design of pairwise interatomic potentials...72
4.3 Atomic force computation...78
4.4 Initial spherical polar coordinates assignment..85
4.5 Initial momentum assignment and kinetic energy calculations.......................89
4.6 Calculation of trajectory..92
4.7 Conservation of energy and back integration 95
4.8 Energy assignment based on vibration modes of water molecule.................100
4.9 Octahedral structural arrangement of $[Cu (H_2O)_6]^{2+}$ complex molecule.....105
4.9.1 Damped trajectory calculation...109
4.10 Water-Water interaction potential 111
4.10.1 O−O interactions (V_{O-O})..111
4.10.2 O−H interactions (V_{O-H})...112
4.10.3 H−H interactions (V_{H-H})...112
4.11 Simulation of $[Cu (H_2O)_6]^{2+}$ molecule under electrode potential................114
4.12 Simulation results and discussions..117
4.12.1 No voltage condition...118
4.12.2 Experimental voltage condition..122

4.12.3 High voltage condition..125
4.11 Computation of current carried by Cu^{2+}..128

V. SUMMARY AND FUTURE WORK 130

REFERENCES 133

APPENDIX 146

LIST OF TABLES

Table 2.1 Relationship between KPIV and KPOV 32

Table 3.1 Scientific explanation for the influence of pH on MRR 62

Table 3.2 Scientific explanation for the influence of pH on R_a 63

Table 4.1 Comparison table between Q_i values and 7-point slope method. 82

Table 4.2 Current carried by Cu^{2+} at different voltage conditions.....................129

Table 5.1 Summary of the experimental results 131

LIST OF FIGURES

Figure 1.1: Pictorial representation of Cu-ECMP process 8

Figure 2.1: I–V curve of HNO_3 electrolyte with different concentration. (A) Full I–V curve, (B) detailed I–V curve between -0.5 And 0.5 V............14

Figure 2.2: SEM surface photographs at different operating voltage in 0.1 wt. % HNO_3 electrolyte. (A) original surface of no bias, (B) active state: -1.0 V, (C) passive state: -0.25 V and (D) trans-passive state: 0.7 V 15

Figure 2.3: I-V curves as a function of electrolyte concentration of (a) KNO_3 and (b) HNO_3 for Cu...17

Figure 2.4: Pictorial representation of BTA removal mechanism....................................19

Figure 2.5 (A): Anodic polarization for oxidation of a Cu RDE with a rotation speed of 100 RPM...20

Figure 2.5 (B): Anodic polarization for oxidation of a Cu wafer on the ECMP tool operating without pad contact. 21

Figure 2.6 (A): RMS surface roughness vs pH for ECMP electrolytes containing 0.29 m HEDP, 0.13 m glycine, 1 mm PTA, and 3 wt. % colloidal silica. ECMP polishing is done at 3.5 V.......................22

Figure 2.6 (B): Cu removal rate as a function of pH for ECMP electrolytes containing 0.29 m HEDP, 0.13 m glycine, 1 mm PTA, and 3 wt. % colloidal silica. ECMP polishing is done at 3.5 V.......................24

Figure 2.7: Cross-Sectional (A) SEM image of Copper on PCB filled in narrow trenches and (B) optical microscopic image of Copper layer filled in millimeter-scale trenches before ECMP process 25

Figure 2.8: Pourbaix diagram of copper in Cu^{2+} H_2O system 26

Figure 2.9 (A): CMP process (B): ECMP process 29

Figure 2.10: Angle distribution functions P (φ, Z) and P (θ, Z) for the Cu_{27} $(H_2O)_{40}$ model...43

Figure 2.11: Distorted pentagonal water structure is observed on the upper surface. Top (a) and side (b) views. 44

Figure 2.12: Trajectories of the O- atoms corresponding to the first peak closest to the upper slab surface. 44

Figure 2.13: The wall–water angle distribution function g (cos(ϴ),cos(x)) for H_2O molecules (a) in the contact layer, and (b) the rest of the H_2O molecules.. 47

Figure 3.1: ECMP apparatus 53

Figure 3.2: Wafer carrier with anodic conditioning ring 54

Figure 3.3: Sensor integrated ECMP circuitry 56

Figure 3.4: LAPMASTER® 12 lapping machine 57

Figure 3.5: Ultra-sonic cleaner 58

Figure 3.6: Sartorius digital weighing machine 59

Figure 3.7: MICROXAM, optical laser interference microscope (from ADE phase shift technologies) 59

Figure 3.8: Pourbaix diagram of copper-water system 61

Figure 3.9: Variation of MRR with pH at different anodic voltages 62

Figure 3.10: Variation of R_a with pH at different anodic voltages 63

Figure 3.11 (a): Variation of MRR (nm/min) with anodic voltage (V) 65

Figure 3.11 (b): Variation of surface roughness (R_a) with anodic voltage (V) 66

Figure 3.12: Surface texture at (a) 1 V (R_a = 25.209 nm), (b) 3 V (R_a = 16.511 nm), (c) 4 V (R_a = 15.822 nm), and (d) 5 V (R_a = 13.709 nm) 68

Figure 3.13: Initial condition of copper wafer (left) after Cu ECMP (right) 69

Figure 3.14: I-V curves of H_3PO_4 electrolyte under different voltage conditions 70

Figure 4.1: Structure of copper (II) hydrate molecule 72

Figure 4.2: Potential energy (V_2) vs $Cu^{2+}-O$ (r_i) distance. 74

Figure 4.3: Morse potential function curve 76

Figure 4.4: Simple harmonic function curve 76

Figure 4.5: Morse potential curve for $[Cu\ (H_2O)_6]^{2+}$ system in equilibrium position 77

Figure 4.6: Bond angle potential curve for $[Cu\ (H_2O)_6]^{2+}$ system in equilibrium position...77

Figure 4.7: Graphical depiction of 7-point slope method...82

Figure 4.8: Spherical polar coordinates arrangement 85

Figure 4.9: Spherical polar coordinates initialization based on angles 86

Figure 4.10: Copper (II) hexa hydrate complex molecule with randomly assigned positions based on angles and bond length....................89

Figure 4.11: Total energy conservation of the $[Cu\ (H_2O)_6]^{2+}$ system 96

Figure 4.12: Conservation of linear momenta along X, Y and Z direction 96

Figure 4.13: Forward integrated trajectory of $Cu-O$ 98

Figure 4.14: Backward integrated trajectory of $Cu-O$ 98

Figure 4.15: Forward integrated trajectory of $O-H_1$ 99

Figure 4.16: Backward integrated trajectory of $O-H_1$...99

Figure 4.17: Symmetric stretching mode 100

Figure 4.18: Bending mode 100

Figure 4.19: Asymmetric stretching mode 101

Figure 4.20 (a): Vibration of the $O-H$ bond about the equilibrium distance (1.8085 Bohrs) 105

Figure 4.20 (b): FFT of vibration of the O−H bond..106

Figure 4.21: Octahedral structure of copper (II) hexa-hydrate complex molecule 109

Figure 4.22: Marble−bowl experiment 110

Figure 4.23: O−O interaction (repulsion) 112

Figure 4.24: O−H interaction...112

Figure 4.25: H−H interaction...113

Figure 4.26: Total energy conservation of the octahedral [Cu $(H_2O)_6]^{2+}$ system...........114

Figure 4.27: Application of external electric field 115

Snap shots at no voltage condition (at time steps of 0, 50, 150, 200, 250,
300, 350, 400, 450, 500)..118

Figure 4.28: Movement of Cu ion at no volt condition 121

Figure 4.29: Energy plot at no volt condition..121

Snap shots at experimental voltage condition (at time steps of 0, 50, 150,
200, 250, 300, 350, 400, 450, 500)..122

Figure 4.30: Movement of Cu ion at experimental voltage condition............................124

Figure 4.31: Energy plot at experimental voltage condition 124

Snap shots at higher voltage condition (at time steps of 0, 50, 150, 200,
250, 300, 350, 400, 450, 500)..125

Figure 4.32: Movement of Cu ion at higher potential condition 127

Figure 4.33: Energy plot at higher potential condition...127

CHAPTER I

RESEARCH OVERVIEW AND OBJECTIVE

Chapter I elucidates the need for an advanced integrated circuit planarization process. A review of the literature related to different planarization processes and a conceptual review of the mechanisms of the copper electrochemical mechanical planarization (Cu-ECMP) process are discussed. Lastly, the contribution of this research work to the academic and industrial knowledge is presented and the organization of the reminder of the thesis is summarized.

1.1 Significance of the electro chemical mechanical polishing (ECMP) process

"The number of transistors on integrated circuits doubles approximately every 18 months"

- Gordon E. Moore, 1965

Over the past four decades, as Moore's law played out, the size of Si-based semiconductor components decreased and the device density increased by some 4 orders of magnitude. As future technologies are increasing device density, shrinking device dimensions and integrating novel device structures, semiconductor processing has been

considered an alternative approach to effectively and efficiently accommodating this increase in transistor density. Debatably, planarization is one of the most critical, costly, and poorly understood processes in semiconductor processing.

A good planarization process is required to achieve a desirable depth of focus while patterning the wafer by lithography. In order to achieve the critical planarity required by future (sub 22nm) technology nodes, there ought to be new technology drivers in planarization, for both metal and dielectrics. After the wafer patterning, a barrier film made primarily of tungsten or tantalum is formed on the Si surface either by physical vapor deposition (PVD) or chemical vapor deposition (CVD) methods. This layer prevents the doping of Si by copper. Deposition of the barrier film is followed by formation of interconnects. Previously aluminum and tungsten metal interconnects were primarily used in IC chips because of their good electrical conductivity and low density. But as the feature sizes are being significantly reduced, better materials such as copper, which has higher electrical conductivity and superior resistance to electro migration, are needed to replace Al interconnects. Aluminum lines have been fabricated by the subtractive dry etch process but dry etching of copper is difficult. However, Cu interconnections have been incorporated successfully by means of electroplating and dual damascene techniques [1]. Copper exhibits the possibility of diffusing into Si and SiO_2, thereby degrading the device performance by introducing deep electronic levels into the Si band gap, eventually reducing the life time of the minority carrier. Moreover, the presence of Cu-Si precipitates in critical regions intensely affects the reverse leaking

current of p-n junctions. This diffusion problem was solved by using a tantalum, tungsten, titanium or Ta alloy diffusion barrier layer [2, 3], which were successfully formed on the Si wafer surface by means of physical vapor deposition (PVD) and chemical vapor deposition (CVD) processes.

To date, chemical mechanical planarization (CMP) is being used to planarize the surface. CMP combines the effect of chemical (through slurry) and mechanical (through pad pressure) processes to achieve the desired planarity. Although CMP is an effective planarization technique, several quality issues including within-wafer non-uniformity (WIWNU), surface scratches, erosion, dishing, delamination, and peeling are known to appear during the polishing of soft metallic interconnects and low-k dielectrics. These glitches eventually lead to high operation and process maintenance costs [4 − 6]. The crucial problem for CMP arose when low-k dielectric materials were introduced in the mid-1990s by the microelectronics industry to address the need for preventing gate leakage and to reduce the heat dissipation. The only way to increase the material removal rate (MRR) in CMP is by increasing the pad pressure or down force. However, higher pad pressures might lead to delamination and other defects at the Cu interconnect and with low-k dielectric materials, which have a deleterious effect on wafer yields due to the bending of the pad, as low-k dielectric materials are porous and brittle.

Electro-chemical polishing (ECP), another polishing process, has the potential to eliminate some significant defects produced in CMP such as scratches, pitting, and

dishing. ECP basically works on the principle of anodic leveling, which is associated with the removal of imperfections on the surface by the dissolution of metal ions in the presence of current, distributed evenly on the surface [7]. Though ECP was able to produce a defect-free surface, better control over the surface reactions and there-by the material removal rate could not be achieved. Hence a process which can produce a defect-free surface and also better control over the material removal rate is called for.

Many such investigations in CMP and ECP gave rise to a new revolutionary planarization process called the electro chemical mechanical process (ECMP). Sato *et al.* [8] proposed the ECMP process based on the electrochemical dissolution of Cu and reported that it could be used to form erosion-free and scratch-free damascene Cu interconnects at a pressure which is one-tenth of that used for conventional CMP technology. Semiconductor industries look for fast, efficient, and cost effective processes, and ECMP holds the key to achieving effective and efficient planarization of copper-deposited semiconductor wafers for manufacturing thin integrated chips (IC) for electronic products like cell phones, tablets, and laptops and for automobile and aerospace applications.

1.2 Mechanics of electro chemical mechanical polishing (ECMP) process

In the Cu ECMP process, the Cu wafer is made the anode and a metal such as aluminum, which can reduce hydrogen rather than undergoing oxidation when compared to copper, is made the cathode. Electrolytic corrosion ensues when the anode and the cathode (different metals) are immersed in a conductive electrolytic bath, i.e., because of the anodic electric potential, the electrons migrate from anode to cathode, and the copper at the wafer surface is oxidized, leading to the formation of Cu^{2+} ions. The oxidation reaction at the Cu anode is given by

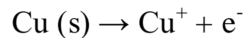

$$Cu\ (s) \rightarrow Cu^{+} + e^{-}$$

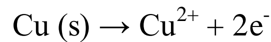

$$Cu\ (s) \rightarrow Cu^{2+} + 2e^{-}$$

In ECMP, Cu^{2+} ions are prominent than Cu^{+} ions because of the applied anodic potential, which promotes electron liberation from the anode. The Cu^{2+}combines with the oxidizer and other components such as corrosion inhibitor, a complexing agent and an electrolyte present in the slurry leading to the formation of a 0.1 - 10^{3} nm thin film of a soft copper oxide complex that serves as a passivation layer. So the basic composition of the passivation layer should have metallic oxides and hydroxides as well as metallic complexes. Formation of the oxides present in the passivation layer on the anode (the Cu wafer in this case) can be summarized as follows [9]:

$$2Cu^{+} + H_2O \rightarrow Cu_2O + 2H^{+}$$

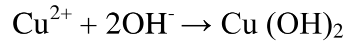

$$Cu^{2+} + 2OH^{-} \rightarrow Cu\,(OH)_2$$

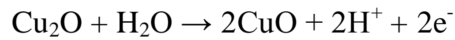

$$Cu_2O + H_2O \rightarrow 2CuO + 2H^{+} + 2e^{-}$$

Formation of hydroxides and the copper complex with phosphoric acid slurry is given as follows [10, 11, 21, and 28]:

$$Cu^{2+} + H_3PO_4 + H_2O \rightarrow [Cu\,OH]^{+}\,[H_2PO_4]^{-} + 2H^{+} + 2e^{-}$$

The passivation layer is then gently removed by the mechanical action of the polishing pad and the abrasive particles present in the electrolyte [12]. Since an electrolytic dissolution of material accompanies the chemical mechanical polishing action, a very low mechanical down force, as low as 1/10th of that applied for CMP, is sufficient to planarize the asperities [11]. Therefore, many defect-generating mechanisms in the CMP process are absent, which leads to improved wafer quality. Low down force is the most preferred process condition for polishing soft metals and low-k dielectric materials that are porous and soft. The ECMP polished surfaces tend to be devoid of defects like surface cracking, pits, and delamination.

In general, 4 electrochemical regions are observed during the ECMP process, based on an increase in anodic potential:

1) The active region, where the applied anodic voltage is very low. The material removed in this region is primarily due to the mechanical action of the polishing pad. Some authors have also claimed that there can be no material removal at this region [11, 12]. If the process is operated in a low pH region, prominent corrosion marks could be smeared over the surface rather than being removed, as the pad pressure is low in ECMP. Also there is no improvement in surface quality, and the surface quality might deteriorate.
2) The passive region is characterized by an increase in corrosion and formation of the passivation layer. More pad pressure is required to remove the continuous formation passivation layer. This removal tends to induce more scratches, delamination, and peeling defects. Although in this region the MRR might increase, the surface quality tends to be poor due to the increase in pad pressure.
3) The transient region is the best region to work with in ECMP. The passivation layer becomes softer and less stable at this region. The electrolyte present in the slurry acts against the applied anodic potential, leading to an increase in Cu^{+}/Cu^{2+} stripping from the copper surface. These copper ions further react with the components of the slurry and form a soft passivation layer over the copper wafer which can be easily removed using low pad pressure.
4) In the trans-passive region, film formation and breakdown happens as a part of a dynamic equilibrium. So with the optimal pH (near neutral), we can achieve the good surface finish with high MRR.

Figure 1.1 provides a pictorial elucidation of the working principle of Cu ECMP. With application of anodic voltage, a complex oxidation layer called passivation layer is formed over the Cu wafer surface. The passivation layer is removed by the action of polishing with very low pad pressure.

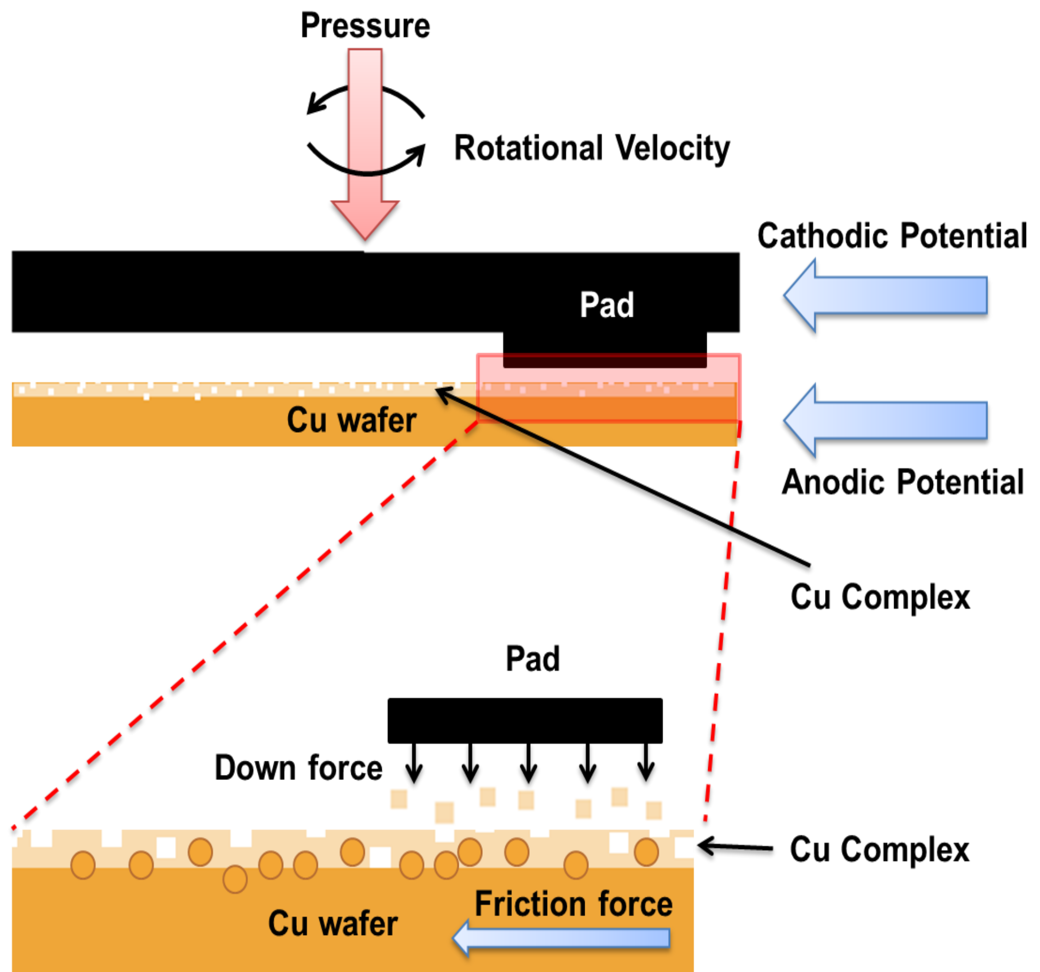

Figure 1.1: Pictorial representation of the Cu ECMP process

1.3 Advantages of the electro chemical mechanical polishing (ECMP) process

The principal advantages of ECMP over CMP are speed and efficiency. The ability to planarize the copper oxides off the wafer in less time and with better surface quality and fewer defects makes ECMP more advantageous than CMP. Such abilities can be achieved only by reducing the pad pressure applied over the wafer to planarize the excess copper. In order to tackle the slow-signal relay problem, SiO_2 was replaced by low-k dielectric materials, as a barrier between the interconnects. However, low-k dielectric materials are 4 times softer than SiO_2. CMP, which primarily relies on the mechanical force exerted on the wafer for removing material, cannot produce the desired level of planarization without destroying the underlying low-k dielectric isolations. Subsequently, ECMP has become the solution because it is able to remove the material quickly and efficiently with less force compared to CMP [13]. With CMP, precise control over the material removal and also determining the level of planarization is difficult. But in ECMP, by controlling the current density applied to the wafer, we can easily determine the material removal rate (MRR) and also the level of planarization.

After the electro-deposition process, a one-micrometer thick mound of copper is formed over the wafer surface, thicker in the middle than at the edges [14]. CMP tends to remove more material from the edge while removing the mound from the center, which consequently increases the resistance in the wires, rendering many chips useless [15]. However, as ECMP's principle mechanism of material removal is electrochemical,

it removes material globally; and by just sweeping off the surface, it gives a clean and smoother surface than can be produced in CMP.

It has been officially claimed by Allied Materials that the cost of slurry could be cut down by nearly 30% by using ECMP compared to CMP. The cost of slurry is around $15 - $20 for the CMP process and can be reduced by $4.50 - $6 in the ECMP process, which can eventually eliminate much of the processing cost from one of the most expensive processes (i.e., CMP is second only to lithography) in the IC manufacturing process.

To summarize, the chief advantages of ECMP include efficient planarization of low-k-dielectric materials with low pad pressure; less polishing time compared to CMP; elimination of surface defects like scratches, delamination, and erosion as seen in CMP; and much easier end point detection effective controlling of applied current density and efficient slurry handling and waste disposal systems [31].

1.4 Challenges in electrochemical mechanical polishing

Despite the great effort put into understanding the process characteristics, two conflicting theories are put forth to explain the formation of the passivation layer in the Cu ECMP process. The first theory proposes that the $Cu^{2+/}Cu^{+}$ ions resulting from the oxidation process interact with the inhibitor present in the slurry to form a soft passivation layer on the wafer surface, which in turn is removed easily by the sweeping action of the polishing pad with minimal pad pressure [33]. The second theory is that a

passivation layer of some sort of polymer is deposited on the Cu surface and that this layer has a higher resistance than the exposed areas, and thus mechanical removal by the pad allows for localized Cu dissolution/removal [33]. Hence there is a lack of understanding of how the passivation layer is formed. Consequently end point detection in ECMP becomes difficult.

In order to better understand the process mechanics, methods which can help us to study the interaction of atoms in the fundamental level need to be developed. Such methods can help us observe the behavior of the $Cu-H_2O$ complex ions formed during the process. Molecular dynamics simulation, one such method, can help us mimic the formation of copper complex molecules precisely in the way they are formed during the actual ECMP process. Studying Cu-ECMP from an atomistic standpoint requires attention, as it can aid us in determining the process mechanism accurately and thereby optimizing the MRR and surface quality in the ECMP process. The result might be process improvement and an ability to perform real time quality control of the process.

1.5 Objective statement

Copper electro chemical mechanical polishing (Cu- ECMP) is a relatively new polishing process which has the potential to replace the currently employed chemical mechanical polishing (CMP) in the semiconductor manufacturing industry in terms of process efficiency and the quality of surface produced. ECMP is known for its higher MRR and effective planarization at low down force. Moreover many of the defects

generated by CMP, such as dishing, erosion, and delamination, can be reduced/completely eliminated. But the optimum parameters for planarization efficiency are yet to be identified. Dynamic changes in electrochemical regions in ECMP, i.e., active, passive, transient, and trans-passive regions, require better understanding. Also the passivation layer formation mechanism is least understood and requires more insight so that we can design the process so as to achieve better qualitative and quantitative yield. The objectives of this study are as follows:

1. Improve the efficiency of the existing Cu-ECMP setup and integrate a data acquisition system with the ECMP setup to capture the time frequency patterns of V-I dynamics to identify the process mechanisms as well as to estimate the effects of various process parameters and thus optimize MRR and surface quality in ECMP.

2. Develop a molecular dynamics simulation model to study the formation of the cuprous hexa-hydrate complex molecule, i.e., $Cu[(H_2O)_6]^{2+}$, which is one of the significant components of the passivation layer and slurry formed during the Cu-ECMP process. Also to observe the behavior of the complex molecule in the presence of electrode potential to better understand the process.

CHAPTER II

BACKGROUND AND REVIEW OF LITERATURE

2.1 Prior experimental investigations into ECMP process mechanisms

Characterization of ECMP process, including the effects of applied voltage, current density, down force and chemical composition has received some attention in the literature [2, 15-18, 26, 27]. In this chapter let us discuss some of the works researchers have done related to the Cu-ECMP process.

2.1.1 Effect of electrochemical actions on the process

Work done by Seo *et al.* [14] provides vital information about the characterization of the electrochemical mechanisms of the ECMP process. He studied the voltage-activated electrochemical reactions of Cu with different concentrations of HNO_3 based slurry. From the I-V characteristic curve obtained through concentrations of HNO_3 in electrolyte sweep voltammetry (LSV) and cyclic voltammetry (CV) methods, he tried to evaluate the electrochemical characteristics of Cu, such as the active, passive, transient, and trans-passive states. His work reveals that the I-V relationship depends strongly on the concentration of the electrolyte. Also the active, passive, transient and trans- passive

regions has been clearly mapped out using I-V plots. One interesting feature of these plots is that the first V = IR drop indicates the beginning of a passive state and the second IR drop indicates the beginning of a trans-passive state, as shown in dotted boxes (A) and (B) of Figure 2.1. This drop indicates an abrupt increase in resistance at these regions and this phenomenon indicates that a passive oxide such as CuO or Cu_2O was formed on the Cu surface.

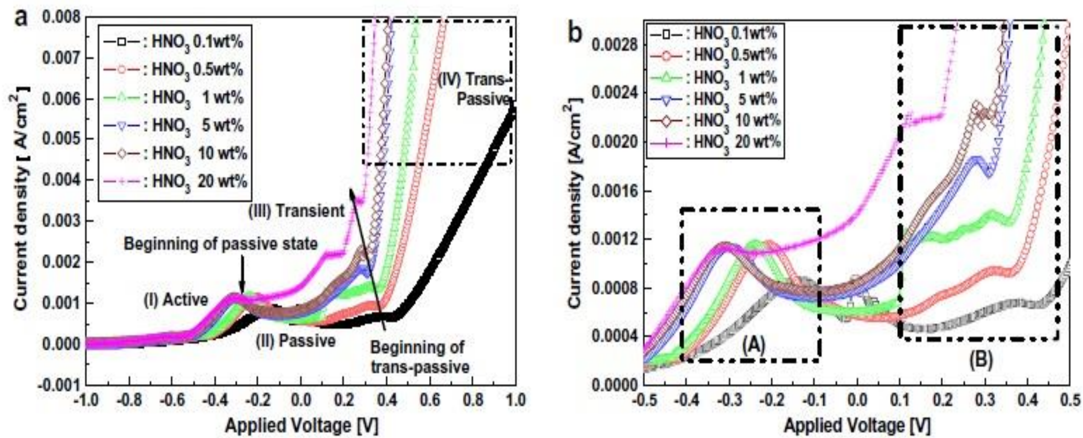

Figure 2.1: I–V curve of HNO_3 electrolyte with different concentrations. (A) Full I–V curve, (B) Detailed I–V curve between -0.5 And 0.5 V [12]

The DC voltage-controlled deposition and stripping mechanisms of Cu were investigated through the cyclic voltammetry (CV) curve. Noticeably different signs of deposition and stripping of Cu were observed. The cathodic current peaks correspond to the deposition of Cu^{2+}, whereas the anodic peaks represent the stripping of bulk and under-potentially deposited copper. Seo *et al.* [14] have concluded that the HNO_3

electrolyte acts against voltage-activated dissolution of Cu by forming a passivation layer composed of oxides on the Cu surface. Verification of the stripping and deposition mechanism through SEM analyses has clearly depicted the surface of Cu at different electrochemical states, as shown in Figure 2.2.

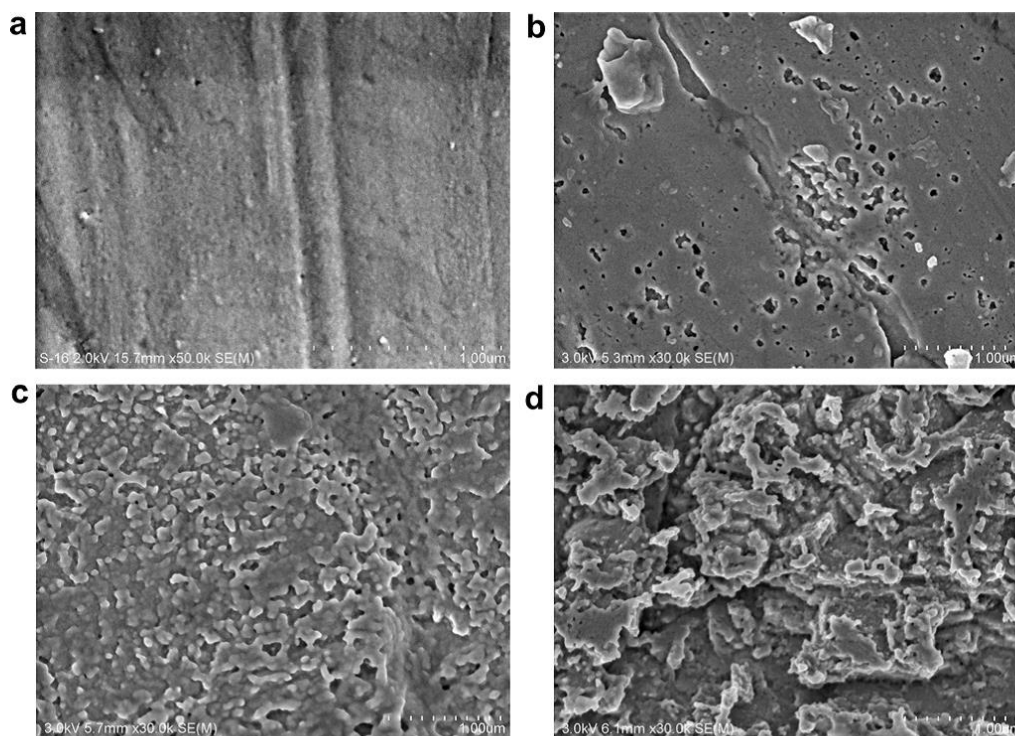

Figure 2.2: SEM surface photographs at different operating voltage in 0.1 wt. % HNO_3 electrolyte. (A) Original surface of no bias, (B) active state: -1.0 V, (C) passive state: -0.25 V and (D) trans-passive state: 0.7 V [12].

Figure 2.2 (A) shows the original Cu surface with some scratches, and no bias was applied over the surface. In the active state, as shown in Figure 2.2 (B), the number of scratches was reduced but some bubble marks along with pitting type corrosion were observed. Figure 2.2 (C) depicts the passive state, where severe corrosion and a

passivation layer composed of oxides were observed. In the trans-passive region, as shown in Figure 2.2 (D), a sponge-like non-uniform surface was observed, mainly because of the stripping of Cu as a result of electrochemical reactions on the Cu surface. Thus we can infer that by proper combinations of voltage activation and electrolyte, accurate control over the material removal rate and surface quality can be achieved in the ECMP process.

Han *et al.* [15] studied the current-voltage (I-V) curves to evaluate the effect of electrolytic concentrations of nitric acid $(HNO_3)^-$ and potassium nitrate $(KNO_3)^-$ based slurry on the electrochemical surface reaction of the Cu electrode. In order to study the electrochemical action in detail, they conducted the experiments in the absence of mechanical polishing. I-V curves were plotted as a function of slurry concentrations of 5%, 10%, and 20%. They observed that for both KNO_3^- based slurries, as the concentration increased the trans-passive voltages decreased and the current density increased. Thus a passivation region is formed because of the formation of a continuous passive film composed of oxide and metallic hydroxide which remains on the Cu surface. As the voltage is further increased, the metallic ions get pulled off through the passive film, because of the strength of the potential. This same observation was recorded for HNO_3 slurry, but the trans-passive state was steeper. From this work, we can conclude that the I-V relationship strongly depends on the concentration of the electrolyte. Han *et al.* [15] also investigated the DC voltage-controlled re-deposition and stripping mechanism of Cu from the cyclic voltammetry (CV) curve. They observed distinctly

different signs of deposition and stripping of Cu. The cathodic current peaks correspond to deposition of Cu^{2+}, whereas the anodic peaks represent the stripping of bulk and under-potentially deposited copper.

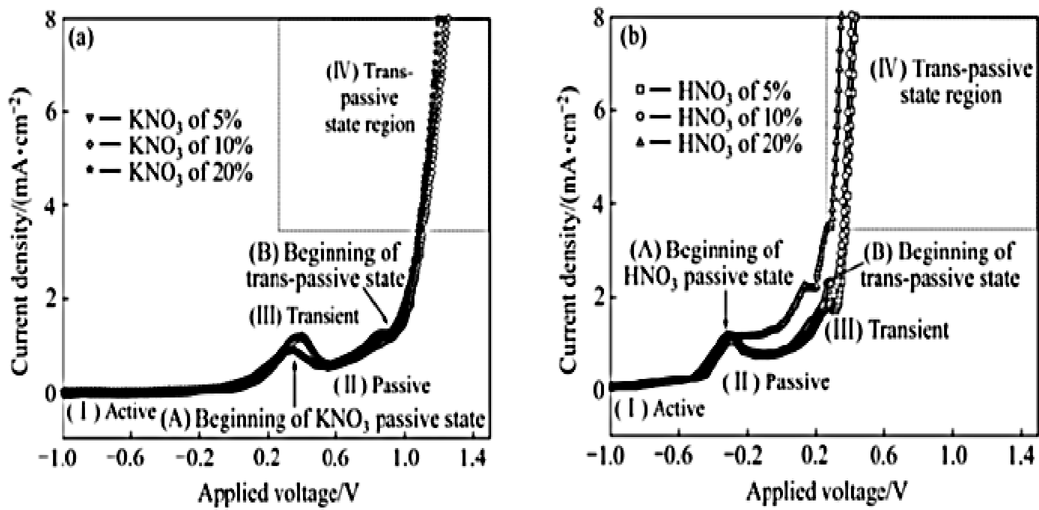

Figure 2.3: I-V curves as a function of electrolyte concentration of (a) KNO_3 and (b) HNO_3 for Cu [11]

The I-V characteristics study by Lee *et al.* [17] on ECMP of SKD11 steel suggests that the transient state is the most suitable for achieving optimal surface quality, and the trans-passive state is preferred for better polishing efficiency (i.e., MRR) [15, 24]. Recent studies in ECMP with H_3PO_4 slurry by Chen *et al.* [12] strongly suggest that at low electric potential, material removal is predominantly due to the mechanical action of the pad whereas at higher potentials, the Cu removal rate is increased due to the effect of the electric potential enhanced by mechanical force.

2.1.2 Effect of slurry composition on the process

In addition to voltage activated material removal, the slurry plays a vital role in the formation of the passivation layer. Corrosion inhibitor, oxidizer, and a pH regulator are three main ingredients of the slurry. Together they govern the formation of the passivation layer. Usually BTA is added as a corrosion inhibitor, H_2O_2 as an oxidizer, and organic salts like KOH for adjusting the pH in acidic ECMP slurry. Kristin *G et al.* [23] conducted planarization studies using phosphoric-acid-based slurry containing 1.0 M potassium phosphate salt concentration with a pH value of 2 and a benzotriazole (BTA) concentration of 0.001 M to check the planarization efficiency of patterned Cu structures. The authors claim that because the ECMP process exploits the combined effect of the anodic dissolution of a metal via an applied voltage and the delicate abrasion of the sample surface from a polishing pad, there is no need for an oxidizer and abrasive slurry particles, which are known to contribute to surface defects. They have focused their studies mainly towards the corrosion inhibition characteristics of BTA.

According to Lin *et al.* [24] and Finsgar *et al.* [25], the BTA inhibition layer can be formed by chemisorption of Cu and BTA in the form of Cu $(BTAH)^{ad}$ or by forming a polymeric BTA-Cu complex film over the Cu surface. In our case (acidic slurry), it is always BTAH, which is chemisorbed onto the surface. Though BTAH is not as strong a layer as polymeric BTA-Cu complex, it is able to protect the Cu surface from electrochemical dissolution. This layer is then easily removed by slight abrasion from a

polishing pad, as it is lightly attached to the Cu surface. This mechanism has been elucidated in Figure 2.4.

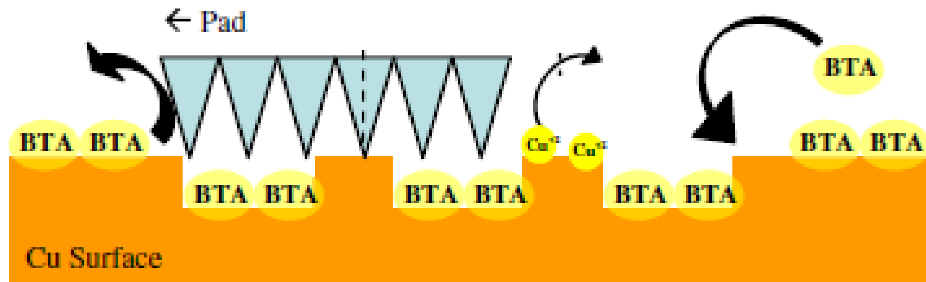

Figure 2.4: Pictorial Representation of BTA removal mechanism [20]

Initially Lin *et al.* [24] and Finsgar *et al.* [25] compared the planarization capability of a custom-built ECMP tool with a rotating disk electrode-type (RDE) method using the same phosphoric-acid-based slurry with different concentrations of BTA as corrosion inhibitors. The following equation was used to predict the planarization capabilities of the ECMP electrolyte using electrochemical methods on a bench top ECMP tool, using blanket wafer fragments, and a Cu RDE:

$$\varepsilon = \frac{S_0 - S_f}{\lambda_{Avg}}$$

where, S_0 and S_f are the pre- and post-process step heights, and λ_{Avg} is the average material thickness removed, calculated from the work piece mass before and after the process. Increasing values of ε imply an increase in feature scale planarization. In Figure

2.5 (A), the anodic polarization curves for oxidation of a Cu RDE with a rotation speed of 100 RPM have been shown.

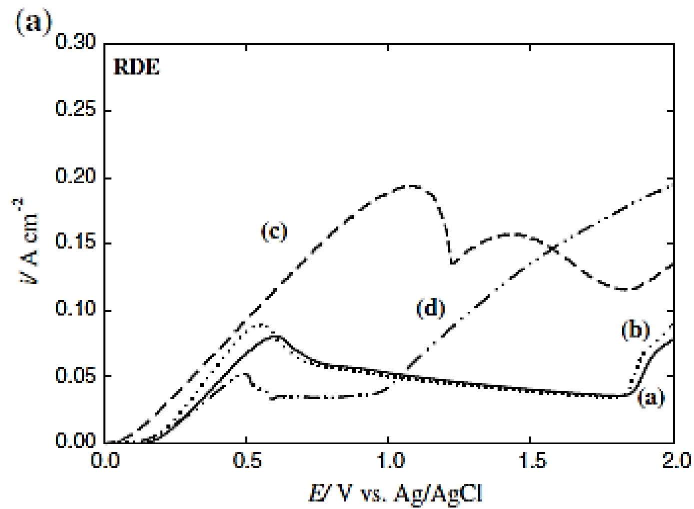

Figure 2.5 (A): Anodic Polarization for oxidation of a Cu RDE with a rotation speed of 100 RPM.

Curves (a) and (b) are electrolytes of concentrated phosphoric acid (pH ~0) containing (a) cBTA = 0, (b) cBTA = 0.01 M. Curves (c) and (d) are electrolytes containing 1.0 M potassium phosphate salt at a pH value of 2 containing (c) cBTA = 0.0 M, (d) cBTA = 0.001 M., after Kristin G *et al.* [23]**.** From these curves, we can infer that in concentrated phosphoric acid, the presence of BTA, even at a concentration on an order of magnitude higher than that in a pH value of 2, has little effect on the polarization curve. Figure 2.5 (B) depicts the anodic polarization curves for oxidation of a Cu wafer on the ECMP tool operating without pad contact.

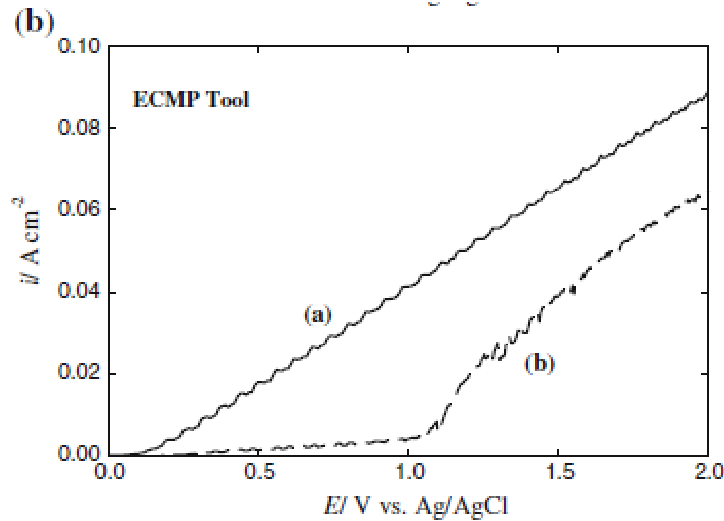

Figure 2.5 (B): Anodic polarization for oxidation of a Cu wafer on the ECMP tool operating without pad contact.

Electrolytes containing 1.0 M potassium phosphate salt at a pH value of 2 containing (a) cBTA = 0.0 M, and (b) cBTA = 0.001 M, after Kristin G *et al.* [23]. This electrochemical experiment demonstrates that in a specific electrical potential region, good passivation at low inhibitor concentrations and high MRR can be achieved; additionally with its simplified bath chemistry, this electrolytic slurry offers considerable advantages over previous electrolytes studied.

Kristin G *et al.* [23] have also conducted planarization experiments using three different pads, Suba^{TM}, IC1000^{TM}, and D100^{TM} with an electrolyte containing 1.0 M potassium phosphate salt at a pH value of 2 with a BTA concentration of 0.001 M at 0.5 V. From this work we can infer that when no potential is applied to the surface of the wafer, no Cu is removed, even with pad contact. Similarly when 0.5 V is applied, if there

is no pad contact, there is no Cu removal. Therefore consistent with *Shattuck et al.* [26], it has been shown that both potential and pad contact are required for material removal in the ECMP process.

Tripathi *et al.* [27, 28] studied the influence of pH and a complexing agent (glycine) on the surface quality and Cu removal rate during ECMP by using a blanket copper wafer. One of the major issues with Cu ECMP electrolytes was that, although they provided excellent Cu removal rates and planarization efficiencies [27], the surface roughness was considerably higher than with the Cu CMP. Tripathi *et al.*[28] used Cu ECMP slurry composed of purified terephthalic acid (PTA) at various pH values. They demonstrated a few important results concerning surface quality. One is that the surface roughness increases following Cu ECMP relative to Cu CMP, decreases as the pH of ECMP is increased from 3 to 6, and decreases with the substitution of a less aggressive complexing agent (glycine) for oxalic acid. pH is a very critical variable in Cu ECMP because it determines in part whether Cu oxide forms or not. As the pH is raised, the Cu oxide that forms on the Cu surface becomes more stable [26-29]. Due to the importance of pH in the passive film formation mechanism, the effects of pH on Cu surface roughness during ECMP were also investigated. Figure 2.6 (A) illustrates the variation of pH with surface roughness in a glycine-containing ECMP slurry.

From Figure 2.6 (A), we observe that as the pH is raised into the range where a stable Cu oxide forms, the surface roughness value is drastically decreased

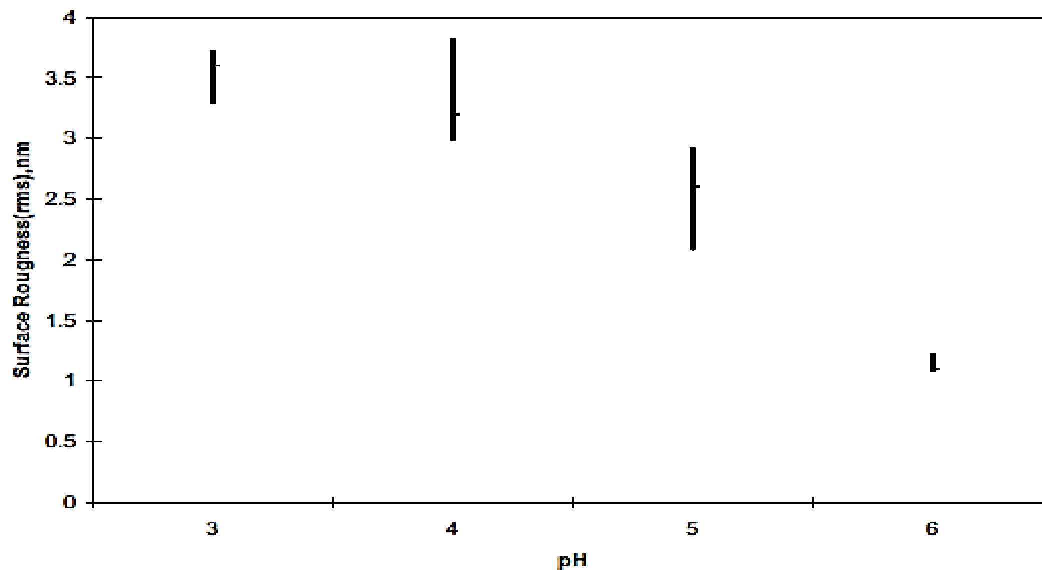

Figure 2.6 (A): RMS surface roughness vs pH for ECMP electrolytes containing 0.29 m HEDP, 0.13 m glycine, 1 mm PTA, and 3 wt. % colloidal silica. ECMP polishing is done at 3.5 V [26]

Figure 2.6 (B) shows the variation of Cu removal rate with the pH of the slurry. It can be observed that as the pH is raised from 3 to 6, the Cu removal rate declines from 620 to 400nm/min. Analysis of the passive film using Electrochemical Impedance Spectroscopy (EIS) suggests that the passive film formed at an applied anodic potential during Cu ECMP is thicker than that which forms during Cu CMP at the open circuit potential [26].

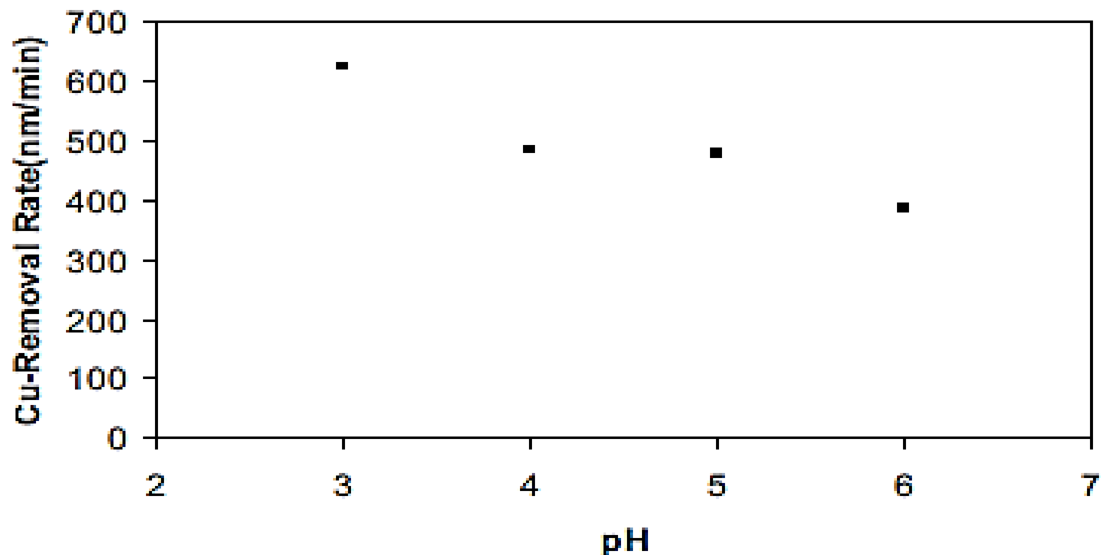

Figure 2.6 (B): Cu removal rate as a function of pH for ECMP electrolytes containing 0.29 m HEDP, 0.13 m glycine, 1 mm PTA, and 3 wt. % colloidal silica. ECMP polishing is done at 3.5 V, [26]

Kulyk *et al.* [5] studied the planarization of patterned PCB with copper interconnects with the ECMP process using an alkali based slurry containing benzotriazole (BTA) as a surfactant. They claim that the main purpose of BTA in their work is to overcome the dishing effect. They attempted to optimize the ECMP process by controlling some of the process parameters such as current, pad type, polishing time, pad rotation speed, and additives in the ECMP slurry. They used two Cu/PCB samples: one with trenches of 150 µm ~a few mm wide and 35 µm deep and one with trenches of 30µm ~a few mm wide and 30 µm deep. Both are overfilled with copper by electro deposition.

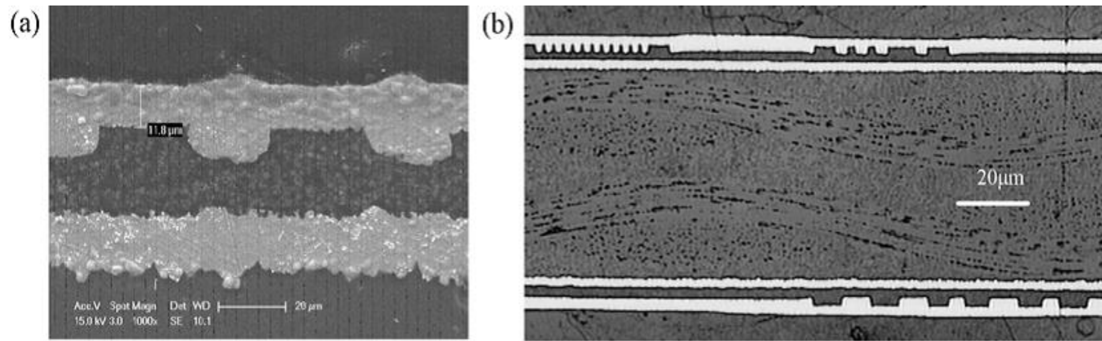

Figure 2.7: Cross-Sectional **(A)** SEM image of Copper ON PCB filled in narrow trenches and **(B)** Optical Microscopic image of Copper layer filled in millimeter-scale trenches before ECMP process.

Studies by Oh *et al.* [33] indicate that the pH value of the electrolyte should be 14 or higher in order to get a higher polishing rate. This higher polishing rate is due to the formation of mechanically soft phases such as Cu $(OH)_2$, $HCuO^{2-}$ and CuO_2^{-2} under anodic potentials. But from the Pourbaix diagram of copper, Figure 2.8, a hard phase of Cu_2O is generated mainly in the pH range of 6 – 14 at applied voltages of -0.4 – 0.3 V, as shown by Ng *et al.* [30]. In this work, the electrolyte is composed of a 20-30wt% solution of potassium hydroxide (KOH), a 0.5-3wt% of hydrogen peroxide (H_2O_2) solution, which acts as an oxidizer, and 0.005-0.02M of BTA as an additive for uniformity improvement. The pH was maintained around 6 by adding phosphoric acid to the slurry in order to avoid the hard Cu_2O phase, and the anodic potential of -0.4 – 1 V was applied.

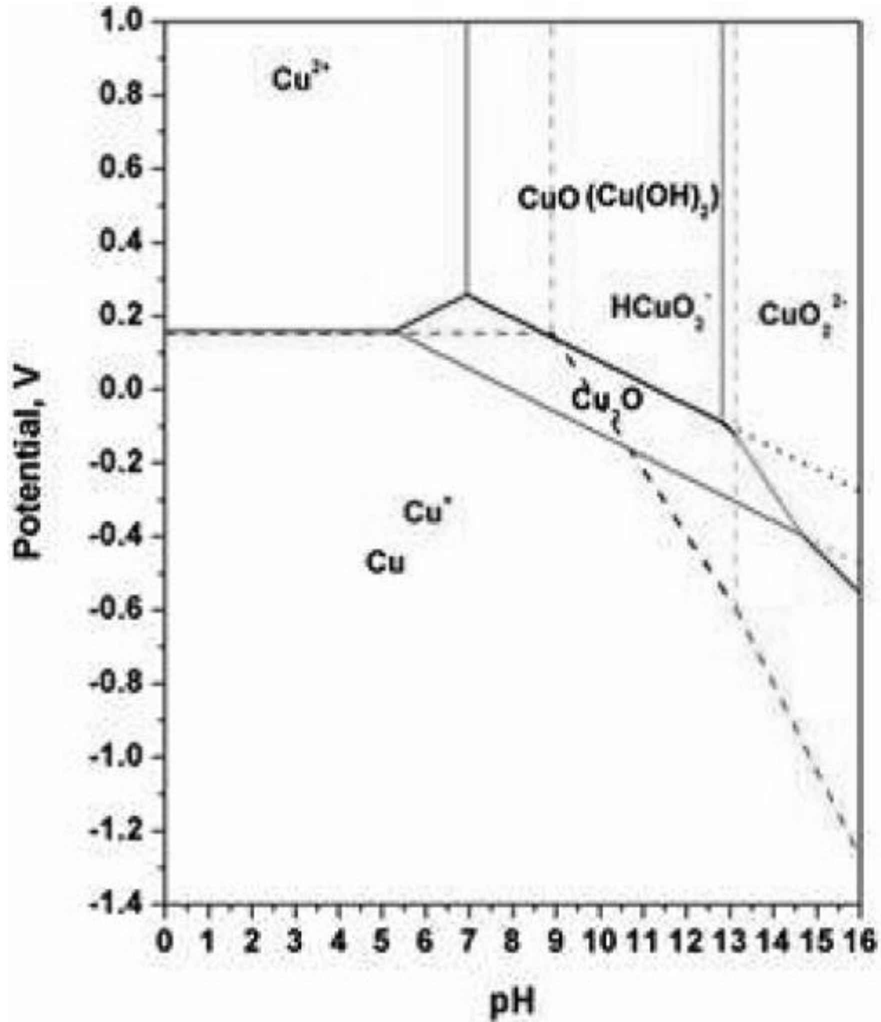

Figure 2.8: Pourbaix diagram of Copper in $Cu^{2+}-H_2O$ system [30]

Some typical slurry compositions used in ECMP are the following:

(i) H_3PO_4 6 vol. %, ethylenediamine 2 vol. %, ammonium citrate 2 wt. %, BTA 0.3 wt. %, H_2O_2 1.5 vol. %, silica abrasives 0.15 wt. % and de-ionized water was used as the solvent [9],

(ii) H_3PO_4 5.1 vol. %, ammonium citrate 2 wt. %, BTA 0.3 wt. %, polymeric inhibitor XP-1296 0.5 vol. %, PolyEthylenImine (PEI) 0.025 vol. % and rest deionized water [9],

(iii) 1 M potassium phosphate, pure ortho-phosphoric acid, potassium chloride, BTA and de-ionized water [9],

(iv) Ortho-phosphoric acid, potassium phosphate, BTA and de-ionized water [29].

2.1.3 The effect of polishing pad, down force, and polishing speed on the process

Liu *et al.*'s [13] study of the effect of down force in ECMP of patterned Cu wafers suggests that a low down force significantly reduces the erosion of dense features, which is usually observed in CMP due to high down-force polishing. Pad structure is another main determinant of the planarization quality and efficiency in the ECMP process. Polishing pads are graded based mainly on their hardness and chemical inertness. Hard polyurethane pads are generally used in Cu-ECMP as they are found to offer high resistance to acidic and alkaline slurries and also a minimal dishing effect in the center of wider trenches is observed [8, 22].

Oh *et al.* [33] studied the influence of soft and hard polymer material pads on the planarized samples keeping the experimental conditions identical. Polyvinyl alcohol pads (soft pads) were found to preferentially remove copper on the edges of the trenches and also produce a dishing effect in the center of wider trenches. Oh *et al.* observed that the "dishing effect" originates from the initial non-uniformities in the copper layer obtained

after the electroplating process. When the copper layer is polished out all the way to the wafer level, the second effect starts to appear, namely the “corner over-removal effect.” This effect is caused by the deformation of the soft pad on the copper-PCB board interface, which leads to a higher pressure in the pad-copper layer interaction and, as a result, a higher polishing rate in the interface region. Using a polyurethane pad (hard pad), such defects are reduced to a larger extent. Their observation clearly shows that uniform planarization was obtained on the copper layer and that pad structure is one of the main determinants of the planarization quality and efficiency in the ECMP process.

Liu *et al.*’s [13] study of the effect of down force in ECMP of patterned Cu wafers suggests that low down force significantly reduces the erosion of dense features, which is usually observed in CMP due to high down force polishing. ECMP can planarize porous low-k materials which would be damaged in a CMP polishing system because of the high load or down force. Lower down force serves as a main advantage of ECMP process. The copper left over from the formation of interconnects is removed from the low-k film without ripping the insulating layer.

Polishing speed is another important advantage of ECMP over CMP. Standard CMP systems cannot achieve very high speeds unless they increase the pad pressure on the wafer. But if the speed is increased, the high pad pressure cracks and peels away the low-k dielectric film [13]. However, decreasing the pad speed means an increase in the polishing time of the wafer. ECMP can achieve the same planarization in less time because the electrochemical mechanism is accompanied by mechanical polishing.

Figure 2.9 (A) shows the cracks observed in the dielectric layer in chemical mechanical polishing, after *Brown* [18] and Figure 2.9 (B) shows the ECMP with flattened wafer and no damage to the dielectric layer, after *Brown* [18].

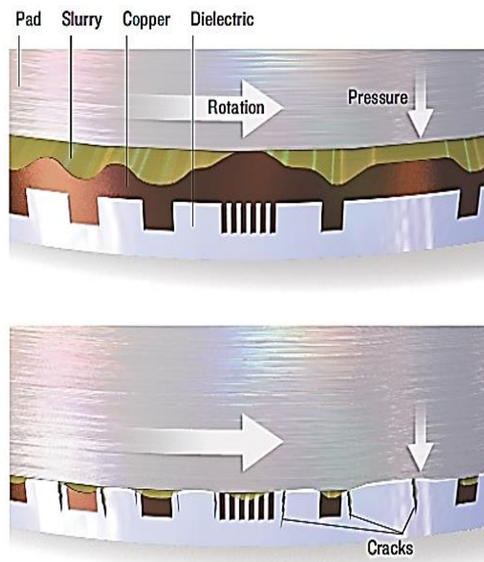

Figure 2.9 (A): CMP process

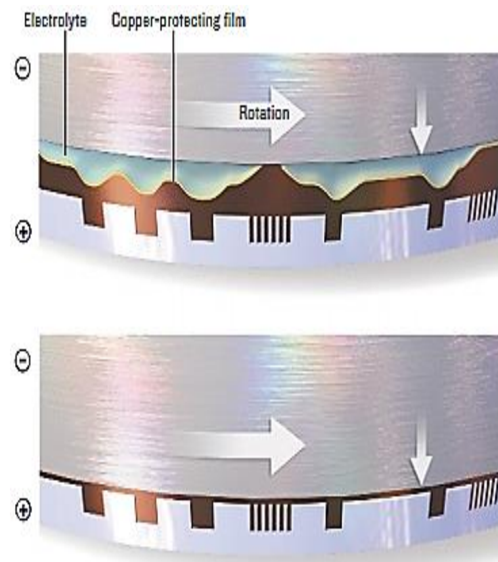

Figure 2.9 (B): ECMP process

Economikos *et al.,* [19] compared CMP process with ECMP process and have shown that ECMP exhibits low dishing than CMP process.

2.2 Elements of the ECMP slurry

The composition of the slurry is a significant factor in ECMP as it should be able to passivate the surface of the wafer [9, 10]. The chemical composition of the slurry should be appropriate so that topographical defects are not formed on the surface. The

slurry should have some fixed components, which are essential for producing a good mirror finish in electrochemical mechanical polishing.

The essential components of the slurry are:

a. Acid based electrolyte
b. Chelating agent
c. Corrosion inhibitor
d. Inorganic/organic salt
e. pH adjusting agent
f. Oxidizer
g. Abrasive particulates
h. Solvent

An acid-based electrolyte ensures electrical conductivity in the slurry. Phosphoric acid, acetic acid, nitric acid, per chloric acid, and citric acid are some of the suitable acidic electrolytes used in Cu ECMP. The slurry can contain 1-30% (Vol.) of electrolyte depending on the required conductivity for polishing [8].

Chelating agents or complexing agents form a complex compound with the copper ions and improve the material removal rate. Uniformity in anodic dissolution can also be achieved by these chelating agents. The formation of the passivation layer is also more efficient with the presence of chelating agents. Ethylenediamine (EDA), ammonium citrate, and acetic acid are some good chelating agents [8]. The concentration of these compounds can be around 0.1–15% by volume or weight of the total slurry composition

A corrosion inhibitor is another important aspect of ECMP slurry. It forms a passivation layer between the metal and the slurry, thereby reducing the chemical

interaction between them. Thus the oxidation or corrosion of the substrate is significantly reduced. The concentration of corrosion inhibitors can be between 0.001% and 5% by weight. Organic compounds like benzotriazole (BTA) and benzimidazole and polymeric inhibitors such as polyalkylaryl ether phosphate can be used as corrosion inhibitors [8].

Inorganic or organic salts enhance the formation of complex compounds in the slurry. The concentration of these salts can be between 0.1 – 15% by volume or weight of the total composition. Ammonium or potassium salts are commonly used in Cu ECMP slurry [8].

pH adjusting agents are used in the slurry to achieve and maintain a desired pH value. The permissible pH range is between 2 and 10 in the ECMP process. Usually 0.2 – 25% by volume of the slurry is composed of the pH adjusting agent. The concentration of the pH adjusting agent can be varied according to the composition of other chemicals in the slurry. Common examples include potassium hydroxide, ammonium hydroxide, and sodium hydroxide [8].

Oxidizers are used to enhance the formation of the passivation layer, which improves the material removal rate. In copper polishing, the copper ions from +1 state (Cu^{+}) are oxidized to +2 state (Cu^{+2}), which aids passivation. Hydrogen peroxide is a common oxidizing agent in ECMP slurry [8].

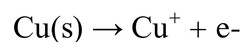

$$Cu(s) \rightarrow Cu^{+} + e^{-}$$

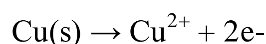

$$Cu(s) \rightarrow Cu^{2+} + 2e^{-}$$

Abrasive particles are used in the slurry to produce a good surface finish. They also enhance the material removal rate. When abrasives are used, ECMP can achieve a surface roughness equal to that of a conventional CMP process. The concentration of the abrasives can be from 0.001% to 5% by weight of the total composition. Silica, alumina, zirconia, titania and ceria are suitable examples of abrasive particles. Finally, solvent, generally deionized water is used as the remainder of the polishing composition [8].

2.3 Relationship between the KPIV and KPOV in ECMP process

Table 2.1 depicts the relationship between the Key Process Input Variables (KPIV) and Key Process Output Variables (KPOV) in ECMP process.

TABLE 2.1 Relationships between KPIV and KPOV

FACTORS	KEY PROCESS INPUT VARIABLES (KPIVS)/ PROCESS PARAMETERS	STATE VARIABLES	KEY PROCESS OUTPUT VARIABLES (KPOVS)/ PERFORMANCE/RESPONSE VARIABLES
Machine (Including the External Power Source)	Down Force, Platen speed, Wafer carrier speed, Input Voltage, Input current	Stress Distribution, Velocity Distribution, Passivation Layer formation	Endpoint thickness of the wafer, Output Voltage &Output Current
Polishing Pad	Stiffness, Topography, Conditioning, Pad Uniformity, Porosity	Contact area, Pad Pressure, Degradation and Temperature Distribution	Material Removal Rate(MRR)(nm/min)

Slurry	Acid based electrolyte, Chelating agent, Inorganic/Organic salt, Oxidizer, pH adjusting agent, Corrosion Inhibitor, Abrasive particulates, Solvent	pH drifts, Concentration, Size distribution, Dispersion, Agglomeration, Aggregation	Within Wafer Non-Uniformity (WIWNU), Wafer to Wafer Non-Uniformity, Within Die Non Uniformity (WIDNU), Erosion, Micro scratch & Pits
Wafer	Size, Curvature, Properties of coating, Coating thickness variation & Pattern Geometry	Direct contact, Hydro planning, Mixed contact	Surface finish, Roughness

2.4 MD Simulation models of electrochemical reactions

2.4.1 General principles in MD simulation

Molecular dynamics (MD) is a computer simulation method by which the physical movement of atoms and molecules and their interactions can be mapped with respect to time by integrating Newton's equations of motion. MD simulation acts as a bridge between macroscopic laboratory results and microscopic time and length scales. This simulation enables us to predict the bulk properties from the molecular interactions up to a certain degree of accuracy. Thus, physical processes can be explored and analyzed at the fundamental atomic and molecular levels. Every material, irrespective of its complexity, is composed of a large number of atoms ($\sim 10^{23}$) even when the analysis is constrained to a nano-metric scale. Such a constraint requires an enormous computing resource in order to study the atomic interactions. MD simulations also act as a bridge

between theory and experiment. A theory can be tested by conducting a simulation using the same model. This model can also be tested by comparison with experimental results. We may also carry out simulations on the computer that are very difficult or impossible in the laboratory (for example, working at extremes of temperature or pressure).

Another significant issue involves the temporal scale in available MD simulations. In order to replicate atomic vibrations precisely, the maximum time step with which Newton's equations can be integrated numerically is essentially restricted to very small values of about 1 *fs*. Because of this constraint, many notable atomic motions require a long computational time for the simulations. Such motions are comparatively slower than the fast oscillations of bond lengths and bond angles that limit the integration time step. Generally, MD simulations are limited to molecular interactions and processes that happen in relatively short times, in other words "rare event" phenomena. Such infrequent processes are simulated quickly. Dissociation of a chemical bond, one such process, is completed on the pico-seconds (*ps*) time scale. However, many experimental events occur on time scales that are orders of magnitude longer than the dissociation time. This feature makes it difficult to observe such events in MD studies. Two approaches are generally followed to overcome the time scale restriction of MD simulations. In the first approach, coarse graining, the dynamic variables are divided into slow and fast degrees of freedom and averaging is performed on the fast degrees of freedom. In the second approach fast (and rare) trajectories between desired states are

computed explicitly, and their probabilities (relative to non-reactive trajectories) are calculated.

2.4.2 Interatomic potentials

The selection of appropriate interatomic potentials plays a vital role in determining the accuracy of the MD simulation results of any lattice structure model. The accuracy level of the trajectory calculations is also affected by the choice of the potential energy functions. In general, the total energy of the system is the summation of the potential energy and the kinetic energy. The computation of kinetic energy is simple but the computation of potential energy is complex, as it relies on the interatomic distances between the interacting atoms. The computational time required to complete the simulation is determined primarily by the complexity of the potential energy functions used in the model. The force acting on an atom is proportional to the negative slope of the potential curve, i.e., the negative first derivative of the potential function. Evaluation of the forces acting on the atoms is essential to calculate new positions of atoms. The functional form of the potential is chosen in a way that can depict the actual potential in the most realistic way for specific material under specific conditions. Two important steps are involved in designing the potential function for a model:

1. Selection of the analytical form for the potential. The analytical form could be the sum of pairwise terms, where the energy of the pair depends on the interatomic

distance, or a many-bodied form appropriate for a specific type of bonding involving bond distances, bond angles, and coordination number.

2. After the analytical form is decided, the specific parameters of the functions are determined. The set of parameters which best fits the data from *ab initio* calculations or experimental properties such as density and cohesive energy, or from a data set containing a combination of both theoretical and experimental observations, is found.

2.4.3 Calculation of the trajectory and potential energy function

As discussed previously, classical dynamics involves simulating the atomic motion by integrating Newton's equations of motion. We now explore how the trajectory on an atom "i" is calculated based on integration of Newton's equation of motion. A trajectory depicts the position of an atom as a function of time. Let the position of the ith particle with respect to time be denoted as $r_i\ (t)$. Let the mass of the atom be $m_{i.}$ Then according to Newton's second law of motion,

$$F_i = m_i a_i \ = \ m_i.\frac{dv_i}{dt} = m.\frac{d^2 r_i}{dt^2}$$

where F_i is the total force acting on atom i, and v_i and a_i are the velocity and acceleration of atom i as a function of time. Force is related to acceleration and, in turn, to potential energy. Acceleration (a_i) and velocity (v_i) are further represented as,

$$a_i \ = \frac{dv_i}{dt}$$

$$v_i = at + v_o$$

The trajectory x_i (*t*) is obtained by integrating the initial positions and velocity (x_o and v_o), as shown in Equation 2.1.

$$x_i\,(t) = v.t + x_o = a\,.\frac{t^2}{2} + v_o t + x_o \tag{2.1}$$

If the force on i^{th} body due to j^{th} body is denoted as F_{ij}, then

$$F_i = \sum_{\substack{j=1 \\ j \neq 1}}^{N} F_{ij} \tag{2.2}$$

Apart from the trajectory, the accuracy of the simulation results depends primarily on the interatomic potentials used to model the lattice structure. Also the accuracy of the trajectories obtained from MD simulations is affected by the choice of the potential energy function. The total energy of the system is the sum of kinetic energy (KE) and potential energy (PE). The KE is simple to compute but the PE computation is complex since it depends on the positions of all interacting atoms. Therefore the computational time required depends on the complexity of the potential function. The force acting on an atom is proportional to the first derivative of the potential energy function. The largest part of a molecular dynamics simulation is the estimation of the forces required to calculate new positions of atoms. Two approaches are available for determining the potential energy of an interacting system. One approach is to perform *ab initio* calculations by solving Schrodinger's equation for the entire system at each integration step. The term "*ab initio*" is used to define a solution of the non-relativistic, time independent Schrodinger equation $\hat{H}\psi = E\psi$. $\hat{H}$ is the Hamiltonian operator for the

system, which is a function of the kinetic and potential energies of the particles of the system, ψ is the wave function, and E is the energy. The Hamiltonian operator for an N electron atom is shown in Equation 2.3 [44].

$$H = -\frac{\eta^2}{2m_n}\nabla_n^2 - \frac{\eta^2}{2m_e}\sum_{i=1}^{N}\nabla_i^2 - \sum_{i=1}^{N}\frac{Z_e^2}{r_i} + \sum_{i=1}^{N}\sum_{j=i+1}^{N}\frac{e^2}{r_{ij}} \quad (2.3)$$

where $\frac{\eta^2}{2m_n}\nabla_n^2$ represents the kinetic energy of the nucleus that comprises the coordinates of the nucleus and derivatives with respect to the coordinates of the nucleus. It is also called the Zero-electron term, as it does not explain either the coordinates of the N electrons or their derivatives. The terms $\frac{\eta^2}{2m_e}\sum_{i=1}^{N}\nabla_i^2$ and $\sum_{i=1}^{N}\frac{Z_e^2}{r_i}$ correspond to the kinetic and potential energy of electrons respectively. The terms together are also called one-electron term. Finally, $\sum_{i=1}^{N}\sum_{j=i+1}^{N}\frac{e^2}{r_{ij}}$ symbolizes the electron-electron repulsion and depends on the coordinates of both electrons; hence it is called two electron terms.

Even though theoretically this approach is best, it is not possible to perform such calculations for the entire system at every time step. For larger systems, comparatively simple and computationally efficient empirical potential functions are used, functions which take into account factors such as bond stretching, bending and torsions, and covalent bonding and long-range interactions such as Van der Waals and Coulombic forces. Rahman [95] used the Lennard-Jones potential and carried out perhaps the first simulation using a realistic potential in order to study the properties of liquid argon. The most common form of the Lennard-Jones potential is shown in Equation 2.4.

$$V_{LJ} = 4\epsilon \left[\left(\frac{\sigma}{r}\right)^{12} - \left(\frac{\sigma}{r}\right)^{6} \right] \tag{2.4}$$

where V_{LJ} is the Lennard-Jones potential, ϵ is the depth of the potential well i.e., the region surrounding a local minimum of potential energy, σ is the finite distance at which the inter-particle potential is zero, and r is the distance between the particles. In this representation both the repulsive and attractive natures of the atomic interaction are well represented and because of its computational simplicity, it is used extensively though more accurate potentials are available. Rahman and Stillinger [96] also carried out a simulation of liquid water. Since then, several empirical potential functions suitable for different materials have been developed. The Lennard-Jones potential is an example of a simple pair potential. Some other examples of simple pair potentials are the Morse potential and the Born-Meyer potential. For complex systems, such as the one involving covalent bonding, generally-used potential functions are the Stillinger-Weber potential, the Tersoff potential, the Bolding-Anderson potential, the Brenner potential, and the embedded atom model (EAM) and modified embedded atom model (MEAM) potentials.

In MD simulation, the trajectories of the interacting particles are defined by virtue of their position and velocity as they change with time. The propagation of position and velocity with respect to finite time intervals can be determined by integrating a couple of first order differential equations. There are time integration algorithms, such as the Verlet algorithm, the leapfrog algorithm and the Beeman algorithm, which can aid us in improving the computational efficiency of the MD simulation. The selection of the algorithm is based on the conservation of energy, the least expensive time frame, and the

integration time step. In general, these algorithms are based on the Taylor series expansion and truncated after some finite number of terms. The Taylor series development is shown in Equation 2.5.

$$x(t) = x_0 + v_0 t + a_0 \frac{t^2}{2} + a_0 \frac{t^3}{3!} + \cdots \qquad (2.5)$$

Once we know position x at time t, after a certain time passes, Δt, we can find $x(t + \Delta t)$, and from there we can get $x(t + 2\Delta t)$. In this way we can also find the change in velocity, $v(t)$ to $v(t + \Delta t)$.

To summarize, every molecular dynamics simulation should have the following components as a part of the program:

(i) A model that can depict the interactions of the constituents of the system (atomic, molecular and interaction with surfaces). It is often assumed that the molecular interactions are pair wise, examples of which are particles with fixed partial charges. These assumptions will reduce the computational time significantly and improve the efficiency of the simulation program.

(ii) An integrator to depict the propagation of particle position and velocity from t to $t + \Delta t$. The integrator is a finite difference structure which moves trajectories discretely in time. In order to ensure stability of the integrator, i.e. the time step, Δt has to be precisely chosen so that there is no drift in the system's energy.

(iii) A statistical ensemble, with a large number of systems each of which, when considered all at once, represents a possible state that the real system might be in and which are required to control thermodynamic quantities like temperature,

pressure or the number of particles in the system. Normally for any MD simulation, a micro canonical ensemble (all the systems are maintained in the same energy state within the total system) is preferred because the system's Hamiltonian potential without external potentials is a conserved quantity.

These components are essential to describe an MD simulation. With this technique, it is possible to obtain exact results with numerical precision.

2.4.4 MD simulation of metal-water interface

With recent advancements in technology, the number of experimental and theoretical studies directed towards analyzing the structure of the metal-water interface has significantly increased. The literature contains a wealth of information and summarizes findings related to the adsorption of water on different metal surfaces, including low coverage adsorption and mono, multilayer and thin water films [78-80, 83, 87, 91 and 93].

The controversy prevailing in the adsorption surface size in Cu-H_2O interaction simulations motivated Nadler *et al.* [91] to investigate monomeric H_2O adsorption in the low coverage regime to determine the size of the large super cell surface needed to obtain converged adsorption parameters. They indicate that the simulation of adsorption geometry of a single molecule can be compared to the adsorption geometry of H_2O in condensed form over the Cu surface.

Based on the X-ray scattering experiments done by Toney *et al.* [92] to study the water density profile of an Ag(111) surface, we learn that the first solvent layer is denser compared to the bulk layer not only for charged surfaces but also when the system is uncharged. Furthermore, based on their work, Schnur *et al.* [93] concluded that the structure and density growth depend on the interaction strength between the surface metal and the adsorbed water molecule. The authors reported a theoretical study of a water-Cu (111) interface based on quantum mechanical calculations performed by means of density functional theory (DFT). First, they calculated the binding energy and structure of water monomers deposited on the metal. Then, they performed first-principle MD simulations on the Born-Oppenheimer surface at two different temperatures to obtain trajectories in order to estimate the relevant interface properties such as the electrochemical potential, the planar distribution functions g(z), the angular probability distribution functions p(φ,z) and p(θ,z), the water layer structure, and the vibrational spectra . The adsorption energy is calculated by the formula

$$E_{ads} = (E_{tot} - E_{Cu} - n.E_{H_2O})/n \qquad (2.6)$$

where E_{tot} is the energy of the total system, E_{Cu} is the energy of the slab alone, E_{H_2O} is the energy of one molecule of H_2O, and n is the number of water molecules adsorbed. The molecules are assumed to be adsorbed on one side of the slab. The negative adsorption energies are equivalent to exothermic adsorption. A p (3×3) three-layer super-cell model is used for the MD simulation of the water layer. Forty H_2O molecules

resulting in a 23.6 A° are utilized for the model. The Lorentz-Berthelot mixing rules are applied to get the Lennard-Jones parameters for the Cu-H_2O interactions. These simulations are done using the molecular mechanics driver FIST that is part of the CP2K package. To get a clear understanding of the orientation of hydrogen and oxygen with the water molecule, the angle probability distribution function on P(Φ, Z) and P(Θ, Z) are analyzed and the authors conclude that the H atoms are located roughly at the same height and, therefore, the molecular plane is tilted away from the slab surface by 30°. Figure 2.10 illustrates the angle distribution function P (φ, Z) and P (θ, Z) for the Cu27 (H2O) 40 model

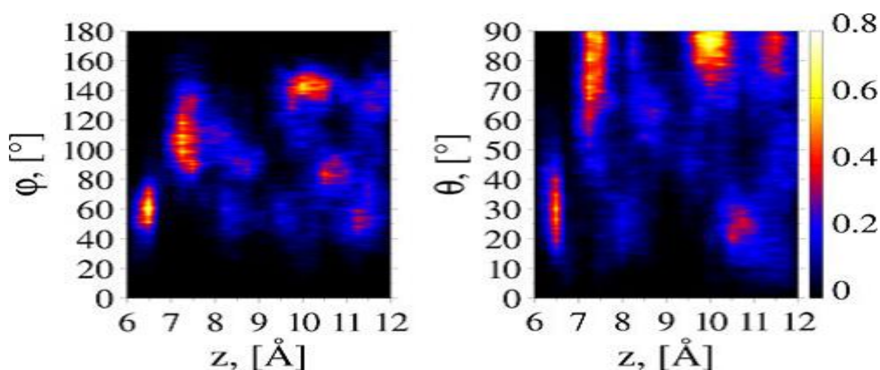

Figure 2.10: Angle distribution functions for Cu_{27} $(H_2O)_{40}$ model [45]

The authors also conclude that the adsorption energies, Eads, and the tilt angle α of water monomers on the Cu (111) surface are sensitive measures and vary strongly with the coverage. Figure 2.11 shows the top view and side view of a distorted pentagonal water structure, which is observed on the upper surface. In Figure 2.11 (a), the super-cell is indicated in yellow. Only the outermost Cu layer is shown in Figure 2.11 (b).

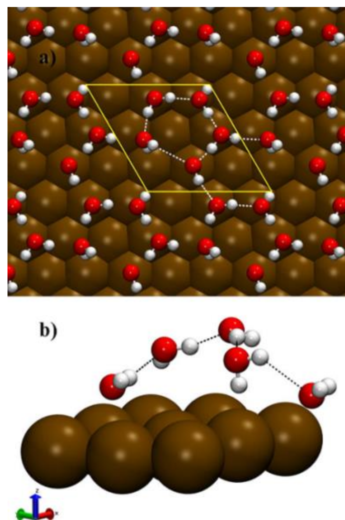

Figure 2.11: Distorted pentagonal water structure Top (a) and side (b) views [45]

Figure 2.12 further depicts the trajectories of the O- atoms corresponding to the first peak closest to the upper slab surface. The lines might be discontinuous as the molecules move further away from the surface. The gray shades indicate the mean location of the corresponding Cu surface atoms

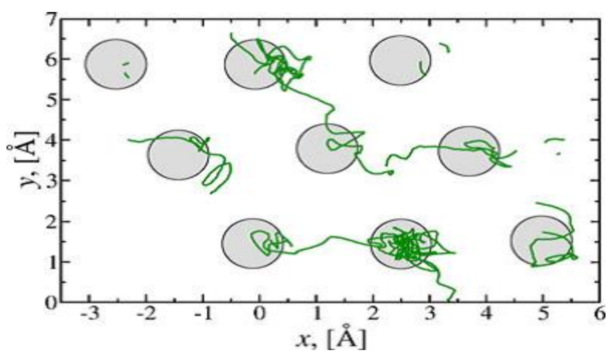

Figure 2.12: Trajectories of the O- atoms corresponding to the first peak closest to the upper slab surface. [45]

The analysis Schnur *et al.* [93] conducted based on Θ and Φ angles reveals that in the first solvent layer, the molecules are mainly arranged in an O- down orientation with their molecular plane tilted away from the metal surface, which is similar to the adsorption geometry of the H_2O monomer at low coverage. The preferred site for adsorption is on top of the Cu surface atoms. In the second solvent layer the molecular planes are nearly parallel to the z-axis and one or two OH-bonds point toward the surface. Finally the authors conclude that the presence of the Cu surface alters the H-bond network, which is similar to the condition observed while increasing the temperature. They suggest that the increase in energy is mainly caused by the weakening of the H-bond network and simultaneous strengthening of the OH bonds.

The accuracy of the MD simulation technique relies mainly on how well the dynamics of the metallic phase and metal-electrolyte interactions are represented. Another important work in the simulation of the interaction between Cu (110)−H_2O was done by Izvekov *et al.* [83], who claim that it was the first fully *ab initio* simulation of a metal-electrolyte interface. Ab initio MD simulations are very efficient in depicting the interfacial structure. They also provide insight into the electronic structure of each species in the system. To investigate whether in a metal–electrolyte contact, the interface structure is governed by water–water and ion–water interactions rather than direct interaction between the water and the metal, the authors have carried out an *ab initio* Car–Parrinello MD simulation of the Cu (110)–water interface. The calculations were done using a plane-wave-based pseudo potential formalism with a generalized gradient

correction to the local density approximation of the exchange-correlation energy as proposed by Becke and Lee, Yang, and Parr (BLYP) [83]. This approach has been shown to provide a reasonable description of hydrogen bonding in water. The system was represented by a tetragonal super cell having dimensions 0.76683 × 1.08433 × 1.8690 nm and containing a seven-layer slab of metal atoms with H_2O molecules filled into the nonmetal region. The exposed face of the slab was the Cu (110) surface of the FCC structure, with 9 atoms per layer, so that the total number of metal atoms per cell was 63. The liquid phase was represented by 24 H_2O molecules. The simulation was carried out using the code ‘‘CPMD Version 3.0f.’’ Analysis of the wall-oxygen distribution function, together with the individual trajectories of the H_2O molecules, showed that the interface had a bilayer structure. Through their simulation, Izvekov *et al.* [83] have showed that the H_2O molecules in the first layer are chemisorbed on the top metal sites of the topmost metal layer, and that these metal sites are partially occupied. The chemisorbed H_2O molecules in the over layer are significantly inclined relative to the normal metal surface and appear to form a square ice-like network through hydrogen bonding. Also the authors have addressed the way the water interface affect the crystal and surface electronic states in the metal slab. Figure 2.13 depicts the wall-water angle distribution function g (cos(ɵ),cos(x)) for H_2O molecules in the contact layer, as well as the rest of the H_2O molecules. The view of the distribution function for the molecules in the contact layer along the cos(ɵ) axis, is shown as an insert in the figure.

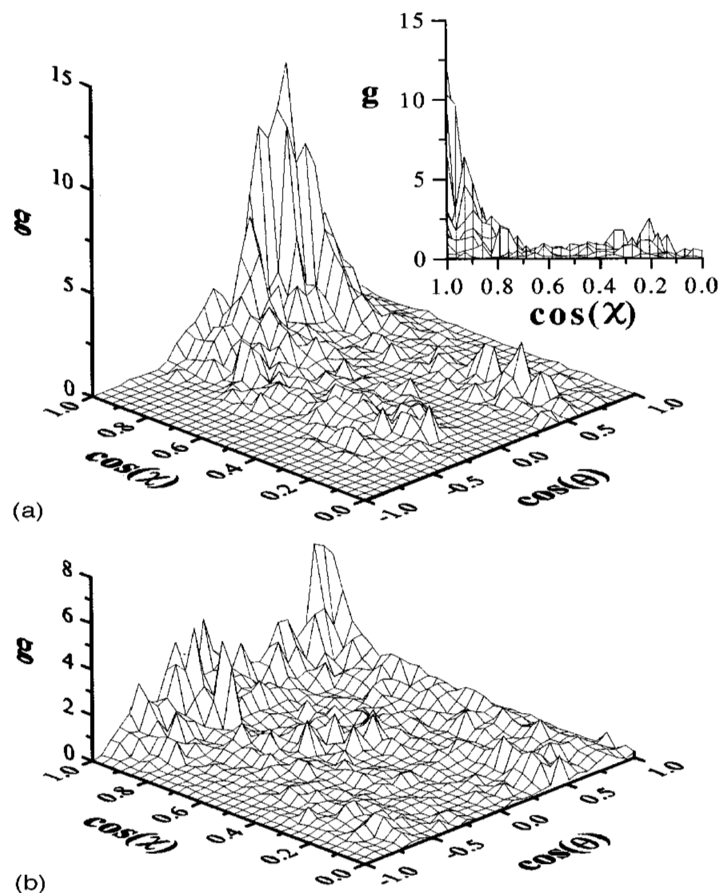

Figure 2.13: The Wall–Water angle distribution function (a) in the contact layer, and (b) the rest of the H_2O molecules. [83]

The work done by Natalia *et al.*[98] and Gonzalez-Lafont *et al.* [99] provides significant insight into the atomic interaction between the Cu^{2+} ion and water molecules. Their work addresses two important aspects of Cu^{2+}–H_2O interaction: The first aspect is whether non-additive terms sufficient for describing solvation of four bodies (e.g. Ion – $(H_2O)_3$) and higher order terms should also be considered. In general, ab initio calculation of a set of trimers is the preferred method for estimation of three-body

interactions i.e., the difference between the interaction energy of the trimer and the sum of the interaction energy of the dimers therein. During non-pairwise additive electrostatic calculation, the remainder of the interaction energy is largely a pairwise additive, especially in the intermediate to longer range. At shorter distances, the intrinsic nonadditivity is represented by the exchange terms in the interaction energy or through intermolecular perturbation theory.

The second aspect is that the average ion water binding energy is markedly lower than the corresponding interaction energy of the ion water dimer. This imbalance of energy has to be corrected by the introduction of a three-body or higher order correction. If it is not corrected, the attraction of the water molecules to the metallic ion will be unreasonably high. This high attractive force can be avoided if an effective potential is introduced to represent the average ion-water interaction energy in a typical solvation condition, instead of a conventional ab initio two-body potential. Gonzalez-Lafont *et al.* [99] introduced an effective two-body potential model function, to the *ab initio* interaction energies of the ion – water clusters while the non-pairwise additive polarization is considered, and a comparative study between conventional and effective ab initio potentials is done. The effects of the counter poise (CP) correction on the ab initio gas surfaces used in the fitting procedure are also examined. Next, two and (two + three body) model potentials for a simulation of Cu^{2+}-$(H_2O)_{20}$ clusters at T = 298 K are tested. The performance and validity of these models are also discussed. Natalia *et al.*

[98] described the Cu^{2+}-H_2O pair-additive interaction energies by a potential function similar to that done by Gonzalez-Lafont *et al.* [51]

$$V_2 = c_1\left[\frac{2q_0}{r_a}+2q_H\left(\frac{1}{r_b}+\frac{1}{r_c}\right)\right]+c_2\left[\frac{1}{r_a^2}-\frac{1}{2}\left(\frac{1}{r_b^2}+\frac{1}{r_c^2}\right)\right]+c_3\left[\frac{1}{r_a^3}-\frac{1}{2}\left(\frac{1}{r_b^3}+\frac{1}{r_c^3}\right)\right]+\frac{c_4}{r_a^4}$$
$$+c_5\left(\frac{1}{r_b^4}+\frac{1}{r_c^4}\right)+\frac{c_6}{r_a^5}+c_7\left(\frac{1}{r_b^5}+\frac{1}{r_c^5}\right)-\frac{c_8}{r_a^6}-c_9\left(\frac{1}{r_b^6}+\frac{1}{r_c^6}\right)+\frac{c_{10}}{r_a^{12}}$$
$$+c_{11}\left(\frac{1}{r_b^{12}}+\frac{1}{r_c^{12}}\right)$$

where, atomic charges q_0= -0.684 & q_H= +0.342

r_a, r_b and r_c are the $Cu - O$ and $Cu - H$ interatomic distances.

Coefficients c_i (i =1,2….,11) were determined by fitting the two body V_2 function to the ab initio-calculated interaction energies of the dimer Cu^{2+}-H_2O for 5 planar and 6 nonpolar orientations of the water molecule around the Cu(II) ion

Gonzalez-Lafont *et al.* [99] studied the energetic and structural properties of Cu^{2+}-$(H_2O)_{20}$ clusters in Monte Carlo simulations at 298K. The same properties are analyzed for a diluted aqueous solution of Cu^{2+} by MC simulation of a Cu^{2+}-$(H_2O)_{200}$ complex. All simulations are carried out with an NVT ensemble using a Metropolis algorithm and cubic boundary conditions with minimum cutoff. The authors claim that if good energetic results are required, then repulsive exchange non-additivity should also be included. In addition, they suggest that the effective pair potential proposed in this work might be

improved by increasing the number of configurations used in the fit with non-octahedral structure.

In this work, water molecules have been assumed to have a rigid structure and the interaction between O-H is not included. Hence the exact depiction of Cu^{2+} ions in water under electric potential cannot be fully visualized.

In a similar work, Lybrand and Kollman [100], developed potential functions for water-water and water-ion interactions that include terms to model nonadditive or a variety of body effects. They used the potentials to estimate solvation enthalpies and coordination numbers for several ionic species: Na^{+}, K^{+}, Mg^{++} and Cl^{-} They used Coulombic or electrostatic interactions to account for the repulsions for O-O and H-H and the Morse-potential function for the O-H interaction. They indicate that many body potentials enable us to model water-solute interactions (specifically water-ion interactions) more realistically than any set of potential functions developed in the past. One important point they did not consider is inclusion of intramolecular degrees of freedom (i.e., bond stretching and angle bending) for the water molecules to correct for the inadequacies of rigid water molecule models.

Natalia *et al.*'s [98] paper discusses the effects of three-body and, in a few cases, four-body and higher-order terms for several Cu^{2+}-$(H_2O)_n$ (n up to 8) clusters proposed as models of the first hydration shell of the Cu^{2+} ion. Their many-body results show that the three-body terms are non-negligible and lead to strong repulsive contributions to the total

pairwise additive interaction energy of the Cu^{2+}-$(H_2O)_n$ system. This work is one of the pioneering systematic studies of three-body and higher-order effects on the interaction between a transition metal ion and water. The authors emphasized the use of intermolecular potentials, which explicitly include the three-body terms, at least those of the type ion-water-water. Also they report from their experimental and computational observations that the water-water-water trimer contributions to the total interaction energy of the metal clusters are small relative to those of the metal-water-water trimers, and consideration of water-water-water three-body contributions will make the simulations of the ionic solutions far slower. Moreover, the effects of non-additivity discussed in this paper are limited to the first hydration shell, and the authors claim that some other divalent metal solutions may require inclusion of metal-water-water trimers with one molecule in each of the first two hydration shells to accurately run the ionic solution simulation.

The effect of voltage on the shape and trajectory of the complex ion-water molecules has received the least attention in the literature, but holds the key to understanding any electrochemical process subjected to an electric potential. Such studies will enable us to predict the ionic mass transfer and material removal rates in electrochemical-mechanical planarization process and will help us optimize the process in a better qualitative way.

CHAPTER III

EXPERIMENTAL STUDY OF THE Cu-ECMP PROCESS

The prime objective of this experimental study is to identify the different electrochemical phases as stated by several authors [12, 13, 14, and 15] and observe the influence of those electrochemical phases on the ECMP process. Through this study, we will be able to identify the best region to work with in ECMP so that it will be possible to optimize the KPOV, which is outside the scope of this work. This study focuses on understanding the ECMP process by exploring the various electrochemical phases.

3.1 Machine Construction

A face-up ECMP apparatus (as shown in Figure 3.1) was designed and fabricated for polishing Φ100 mm blank Cu wafers. Two mini vertical milling machines (Model 44991 from Central Machineries) were arranged such that one milling machine housed the wafer carrier and the other provided rotary motion for the wafer carrier by means of a drive pulley and a V-belt. The axes of the wafer and pad holder tables were offset so that the complete wafers are polished as they rotate relative to each other. An aluminum bar was used as a cathode, considering its electro negativity relative to Cu. The rotational

speeds of the polishing pad and wafer carrier were controlled using the knobs in the first and second milling machines, respectively. The working table was moved with the cross feed handle wheel and the longitudinal feed handle wheel to adjust the position of the wafer carrier with respect to the polishing pad. The pad was offset so that the complete wafer is polished as wafer and pad holders rotate relative to each other. A Shenzhen Mastech power supply, having a range of 0.1–12 V, was used to power the wafer (anode) and the cathode. A wooden base was used to insulate the first mini milling machine from the positively charged anode in the wafer carrier assembly. The apparatus was placed in a fume hood to exhaust chemical fumes formed during the process.

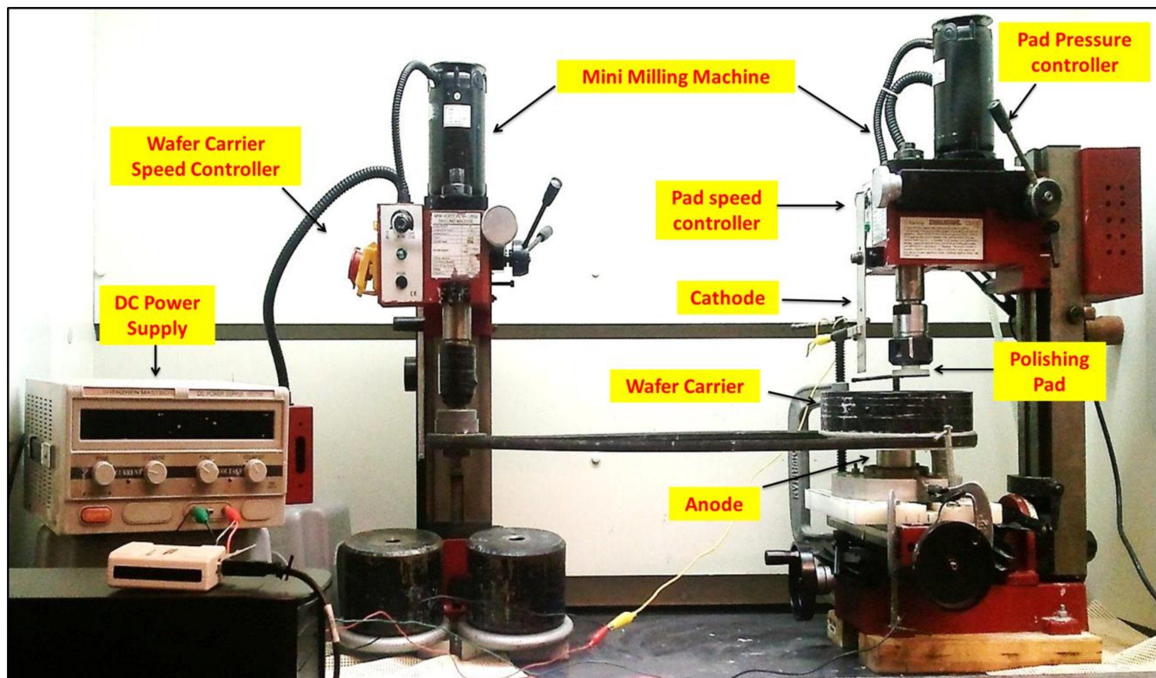

Figure 3.1: Cu ECMP Apparatus

3.1.1 Modification in the machine design

A few modifications were made to the existing ECMP setup in order to accommodate the data acquisition system and ensure that the sensor data is free of errors.

(i) The wafer carrier provided a 4 inch diameter and 0.25 inch depth in order to house the copper wafer. The retaining ring had not been properly designed, initially, so the wafer exhibited some movement during the process. This movement was caused by the simultaneous rotation of the wafer carrier and polishing pad. This movement hindered the current supply to the wafer and thereby affected the electrochemical reaction at the surface of the Cu wafer. To stop this wafer movement during the process and to ensure continuous flow of current, a retaining ring was designed, machined out of aluminum, and placed around the anode so that the entire surface of the Cu wafer was in full contact with the positive potential, i.e. the anode. The wafer carrier after being fitted with the conditioning ring is shown in Figure 3.2.

Figure 3.2: Wafer carrier with anodic conditioning ring

(ii) To stop the vibrations of the wafer relative to the polishing pad, the pad carrier was secured to a 1-inch-diameter collet and then attached to the spindle of the milling machine housing the wafer carrier. This arrangement ensured a constant and uniform contact between the polishing pad and Cu wafer, so that the material removal would be even and no defects produced with respect to the polishing pad over the surface of the Cu wafer.

3.1.2 Installation of the sensor system

The voltage and current signals from the setup were collected by means of an NI DAQmx data acquisition driver. The basic circuitry used for signal acquisition from the ECMP process is shown in Figure 3.3. Three nodes – a_0, a_1 and a_2, of the DAQ driver were assigned to the process current (I), the output voltage from process (V_1), and the input anodic potential (V), respectively. The DAQ was linked to LabVIEW software so that the analog outputs could be digitized and continuous signals could be recorded from the process. These signals were then discretized with a sampling rate of 100Hz. A DC power supply was used to control the anodic potential (V). As shown in Figure 3.3, a 10Ω resistor was connected across the system to measure the process current (I).

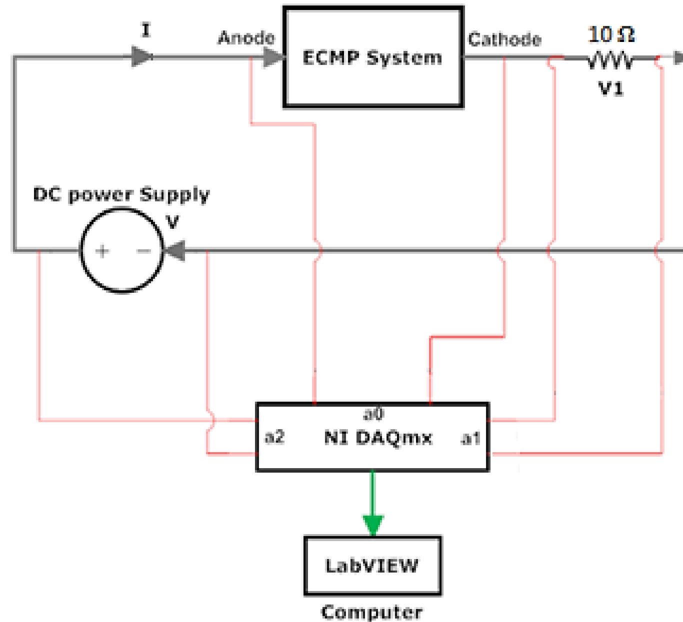

Figure 3.3: Sensor integrated ECMP Circuitry

3.2 Wafer preparation and cleaning

Copper wafers 4 inches (100 mm) in diameter and 0.05 inch thick were used in this study. Copper has the tendency to react with the oxygen present in the surrounding air and the surface becomes oxidized, which prevents the underlying copper from being oxidized. For our study we needed pure copper, so the surfaces were initially cleaned with distilled water and acetone to remove the oxidation products. Some of the wafers undergo deep oxidation in air and bluish/green marks are left on the surface. These marks were removed by fine abrasive paper of grit size 15.3 µm. The abrasive paper was rubbed smoothly, with very light pressure, so as not to scratch the surface. Generally, processes like CMP and ECMP are final finishing processes and hence the material removal rate is

generally lower compared to grinding and lapping processes. The cleaned wafers were then subjected to a lapping procedure to reduce the initial wafer surface roughness to ≈20-30 nm. The wafers were lapped in a bench-mounted LAPMASTER® 12 lapping machine (see Figure 3.4). The wafers were lapped using 1200 grit SiC sheets and then Imperial cloth polishing sheets loaded with fine grit alumina particles. Finally, the wafers were cleaned with distilled water before they were used in the experiments.

Figure 3.4: LAPMASTER® 12 lapping machine

After conducting the ECMP experiments, the copper wafers were cleaned immediately using de-ionized water to remove the slurry debris from the surface. Then the wafers were subjected to ultra-sonic cleaning to ensure that they were completely devoid of oxidation layer residues, which generally are not removed by acetone cleaning. Figure 3.5 shows the ultra-sonic cleaner used for wafer cleaning.

Figure 3.5: Ultra-sonic cleaner

3.3 Measurement of MRR and surface characterization

The weight of the Cu blanket wafers was measured in micrograms (μg) using a Sartorius digital weighing machine (see Figure 3.6) and then converted to grams (g). Then the material removal rate (MRR) was calculated using the following formula:

$$\text{MRR} = \frac{\text{Initial Wt of the Cu wafer (before polishing)} - \text{Final Wt of the Cu wafer (after polishing)}}{\text{Polishing Time (in min)}} \text{ grams}$$

The MRR was then converted to a appropriate unit i.e., nm/min

The surface roughness (R_a) of the copper wafers was obtained using MicroXAM, an optical laser interference microscope from ADE Phase Shift Technologies. R_a was measured in nm.

Figure 3.6: Sartorius Digital Weighing Machine

Figure 3.6: MICROXAM, Optical laser interference microscope (From ADE phase shift technologies)

3.4 Experimental results and discussions

This experimental study focuses on understanding the process mechanism, under different experimental conditions. A phosphoric-acid-based slurry with a composition of 6% (vol.) of phosphoric acid, 2% (vol.) of ethylene glycol, 0.3% (wt.) of benzo tri-azole (BTA), 4% (wt.) of potassium hydroxide (KOH), 0.45 % (vol.) of hydrogen peroxide (H_2O_2), 0.15% (wt.) 0.05 and μm de-agglomerated gamma alumina particles and Buehler Chemo-met© polishing pads were used for all experiments. All experiments had an iteration time of 10 minutes. The pad speed was maintained at 325 RPM and wafer carrier speed was maintained at 22 RPM.

Figure 3.8 depicts the Pourbaix diagram of copper ECMP, which has 4 regions based on the anodic dissolution of Cu and electrochemical reactions happening at the Cu surface. In order to optimize the MRR and R_a, many experiments were carried out based on the different electrochemical regions of the Pourbaix diagram. The phosphoric-acid based-slurry was used for all experiments, as Munnangi [34] found that it provided a good surface roughness and MRR. Hard polyurethane Buehler Chemo-met polishing pads were used for all experiments, as they were found to have the desired mechanical and chemical stability.

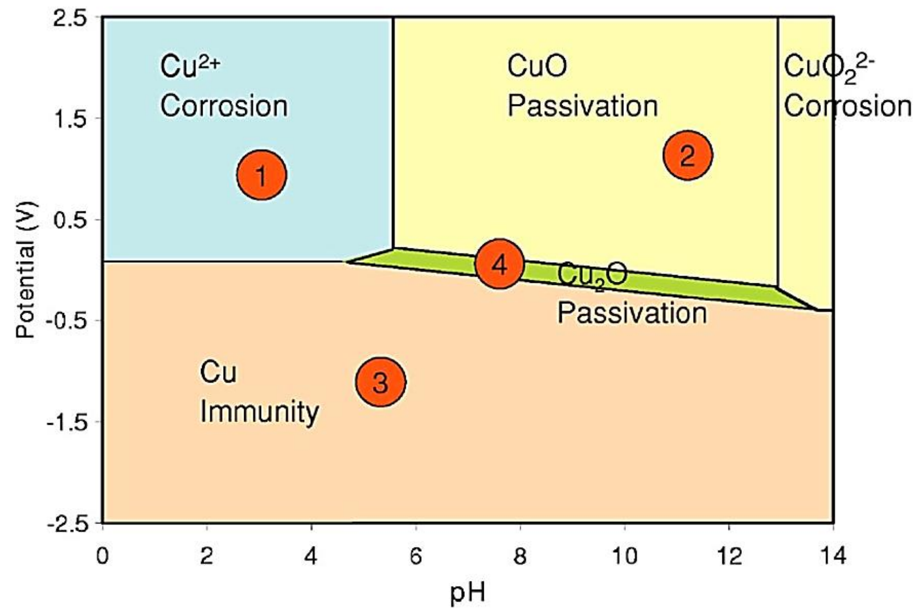

Figure 3.8: Pourbaix diagram of Copper-water system, after Ng *et al.,*

From the Pourbaix diagram, we can observe that at acidic pH (<6) and voltages above 0.5 V, copper undergoes severe corrosion because the anodic dissolution is very high and no sacrificial surface layer is allowed to form on the copper. As the pH is increased i.e., greater than 6, the solubility of the metal interface limits the mass transfer of the metal ions into the solution. A passivation layer is formed when the concentrated ions accumulate at the interface. This layer, which now acts as a sacrificial layer, is removed by pad during ECMP.

3.4.1 Influence of pH in the Process

For this study, the pH of the slurry was adjusted by varying the proportion of potassium hydroxide in the slurry. Figure 3.9 and Figure 3.10, depict the variations in MRR at different voltages and 2 different pH conditions, one acidic (pH = 2.5) and the other near neutral (pH = 6.5).

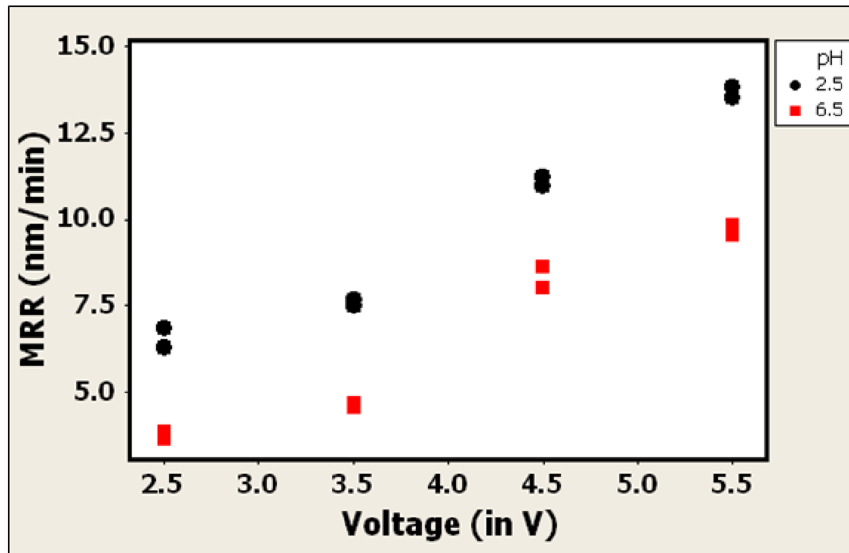

Figure 3.9: Variation of MRR with pH at different anodic voltages

Table 3.1: Scientific explanation for influence of pH on MRR

pH	Observation	Reason for the observation
2.5	• MRR is normally high. • MRR gradually increases with voltage.	• Anodic dissolution rate is very high due to rapid oxidation of the surface. • The dissolution rate is further accelerated with increase in voltage as there is no formation of passivation layer. Cu^{2+} ions are stripped out of the

		surface in a rate, that doesn't provide sufficient time for the formation of passivation layer.
6.5	• MRR is comparatively lower than that observed at pH = 2. • MRR increases with voltage.	• The solubility of the metal interface limits the mass transfer of the metal ions into the solution. • A passivation layer is formed when the concentrated ions accumulate at the interface, which is then removed by the action of polishing pad.

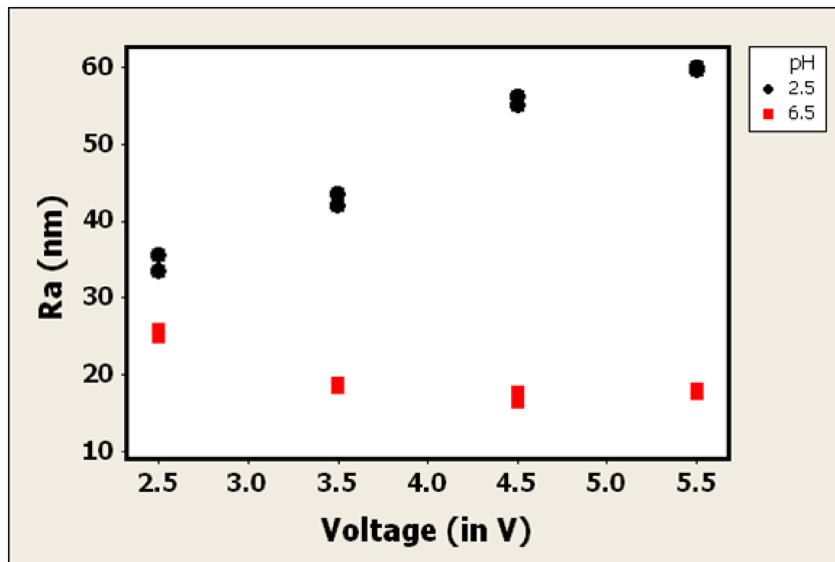

Figure 3.10: Variation of R_a with pH at different anodic voltages

Table 3.2: Scientific explanation for the influence of pH on R_a

pH	Observation	Reason for the observation
2.5	• Severe pitting is observed over the surface. • R_a is very high and increases with voltage.	• The electrochemical dissolution rate of the Cu anode is high, which leads to stripping of Cu^{2+} ions from the surface.

6.5	• Surface roughness values are low. • Occurrence of pitting is reduced and is completely absent at voltages above 4V. • R_a decreases with increase in voltage.	• Anodic dissolution is limited by the formation of passive layer. • Passivation layer formation protects the surface from severe corrosion and gets planarized by the polishing pad.

3.4.2 Effect of anodic voltage

For this study, the pH was maintained around 6.5 (near neutrality) and the other conditions were maintained as described earlier. Figure 3.11 shows the effect of applied voltage on MRR and surface quality, from a process standpoint.

As shown in Figure 3.11 (a), the MRR tends to be low in the low potential region (1−2 V). This region corresponds to the active region, which is generally characterized by low MRR. In the active region, the dissolution rate of Cu^{2+} ions from the surface is low, as the applied voltage is low; in other words, the oxidation rate is less. With very few Cu^{2+} ions available in the system to react with slurry components, the rate of formation of the passivation layer tends to be low. The MRR in this region is primarily dependent on pad pressure (which for ECMP is low) rather than electrochemical dissolution. Hence the MRR tends to be low in the active region. With further increase in anodic voltage (3−4V), the MRR is observed to increase slightly because the process has entered the passivation region. In this region, the dissolution rate of Cu^{2+} increases, which promotes the growth of the passivation layer. With more oxidation over the copper wafer

surface, the MRR tends to improve at this region even with a lower pad pressure. Figure 3.11 (a) summarizes the effect of anodic voltage on material removal rate (MRR).

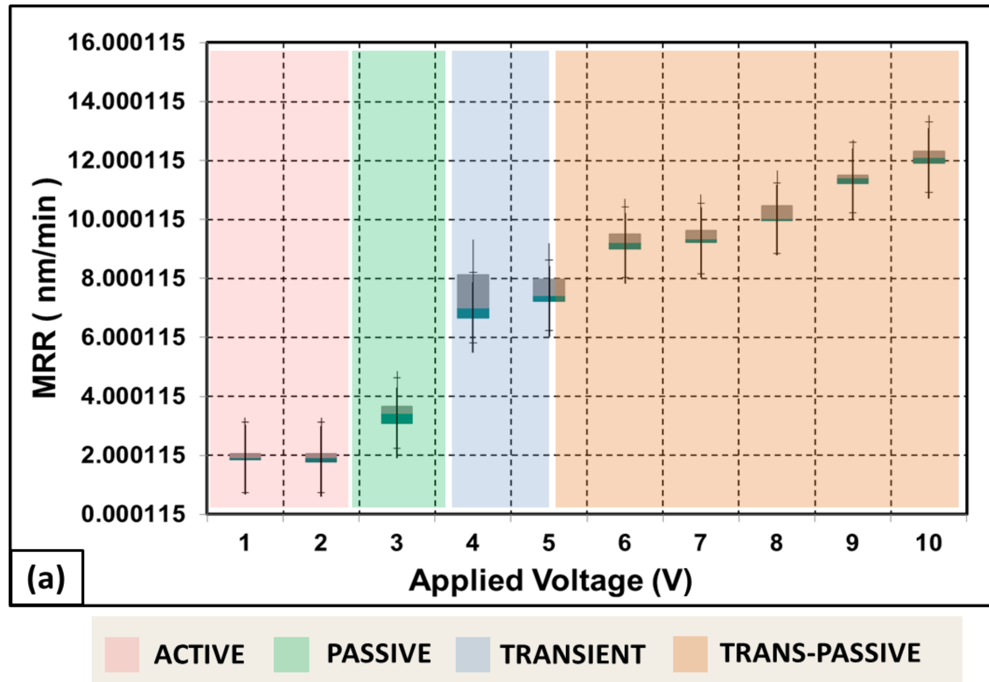

Figure 3.11 (a): Variation of MRR (nm/min) with anodic voltage (V)

At 4−5V the process enters the transient region (as shown in Figure 3.11 (a)) where the MRR increases to a larger extent, indicating that the electrolyte concentration is acting against the applied voltage leading to stripping of the Cu^{2+} ions from the surface of the wafer. Several authors have claimed that the transient region is the best region to work with if high MRR is desired [add the references]. Increasing the voltage above 5V positions the process in the trans-passive electrochemical region, where the film

formation and breakdown happen as part of dynamic equilibrium. Hence the MRR tends to increase linearly with the increase in the anodic potential.

Figure 3.11 (b) summarizes the effect of anodic voltage on surface roughness (R_a).

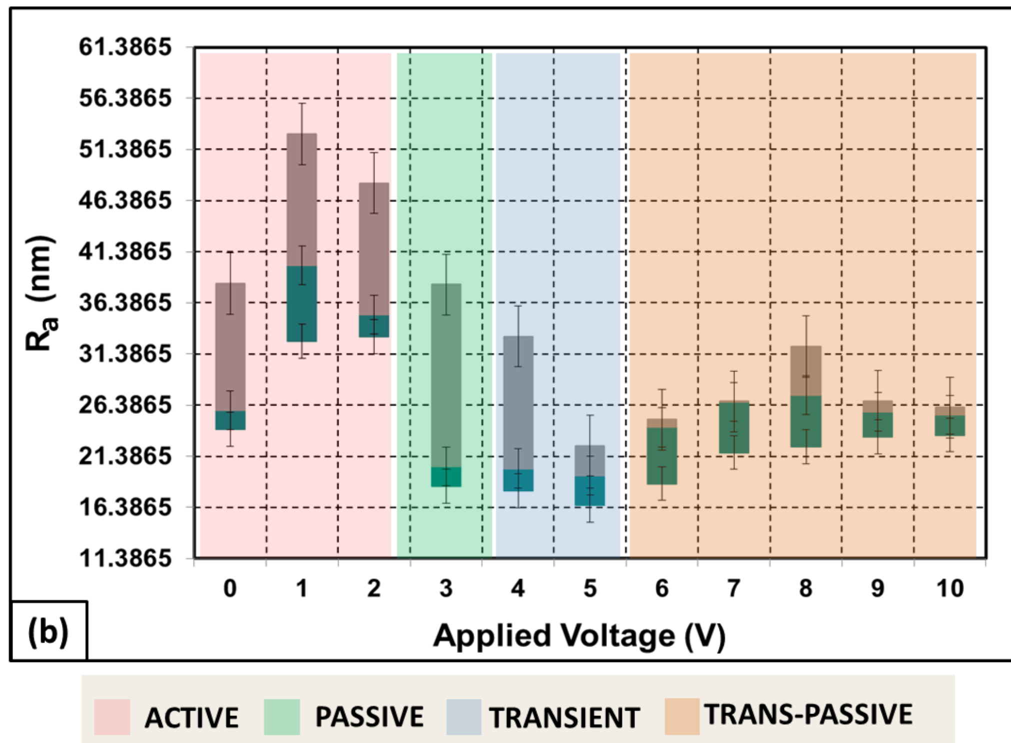

Figure 3.11 (b): Variation of Surface roughness (R_a) with anodic voltage (V)

As shown in Figure 3.11 (b), the R_a value tends to be high and does not change much in the active region (1−2 V). The surface tends to be rough (R_a ~ 25nm) due to severe pitting and corrosion accompanying ohmic oxidation. The removal of asperities is uneven in this region, and as the planarization happens only through the action of the polishing pad, because of the low dissolution rate, the surface quality is deteriorated.

With an increase in voltage (2−3 V), the process enters the passivation region, where the R_a value is comparatively low. The passivation promotes higher material removal from asperities compared to pits. Consequently the surface quality improves gradually in this passivation phase (see Figure 3.11 (b)). For applied voltage in the 3–4 V range, the passivation film becomes softer and less stable, leading to a transient phase. Here, the surface quality is much improved (see Figure 3.11(b)). For voltages above 4 V, the ECMP process follows a trans-passive electrochemical transfer, where the film formation and breakdown happen as part of dynamic equilibrium. Here surface quality deteriorates with increasing voltage because of frequent breakdowns of the film and removal of surface asperities.

3.4.3 Surface texture analysis

Figure 3.12 shows the images of copper wafer surface captured at different electrochemical regions through laser interferometer, MicroXAM. Through surface analysis, we can physically observe the effects of active, passive, transient and trans-passive regions on the Cu wafer surface. In the active region, we can observe that the surface tends to be rough (R_a ~ 25nm) due to severe pitting and corrosion. Here the dissolution rate is poor and the passivation region is not being effectively formed and removed. We can also observe smeared marks on the surface, which is the result of polishing pad smearing the poorly formed passivation region during the process. In the passive region, we can clearly see the existence of corrosion marks and parts of the

passivation layer. In the transient and trans-passive regions, we can see a clear improvement in the surface. The surface roughness values are also very low (R_a ~ 13-15nm), with most of the scratch marks, corrosion marks and pits removed. Some deep scratches still remain on the surface as ECMP process is a nano manufacturing process; it is incapable of removing deep scratch marks produced during the initial stages of slicing from the ingot.

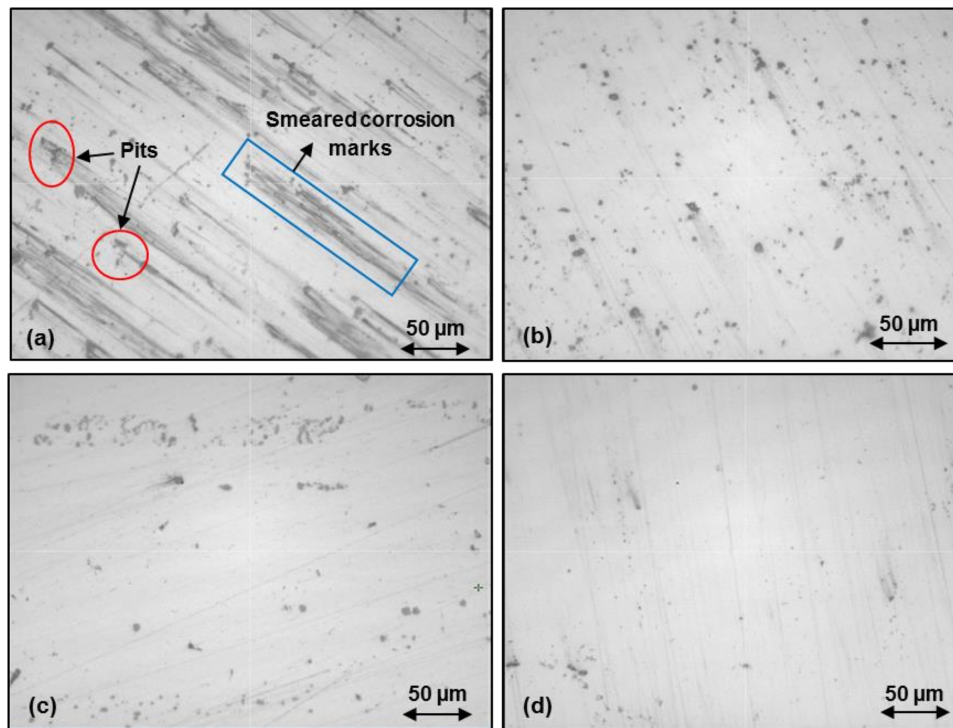

Figure 3.12: Surface Texture at (a) 1 V (R_a = 25.209 nm), (b) 3 V (R_a = 16.511 nm), (c) 4 V (R_a = 15.822 nm), and (d) 5 V (R_a = 13.709 nm)

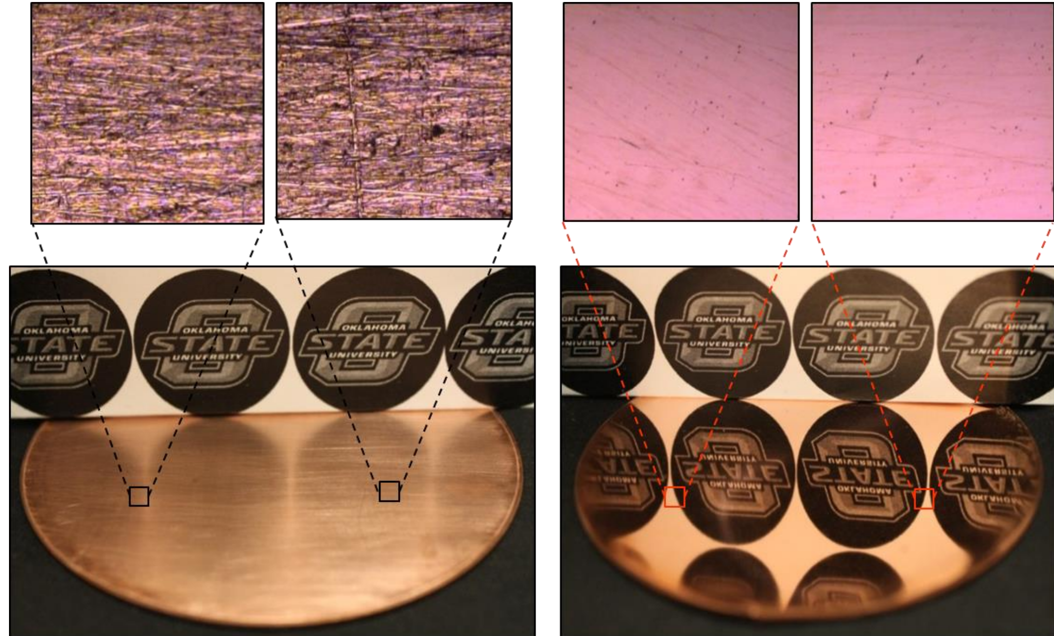

Figure 3.13: Initial condition of Copper wafer (Left) After Cu-ECMP (Right)

Figure 3.13 shows the actual and micrograph images of random regions of the wafer. The image to the left shows the initial surface of the wafer with lot of scratches. The R_a was brought down from 60-70 nm to 25-30 nm using Lapping process. The image to the right shows the surface of the copper wafer after ECMP process with a run time of 10 min and at an anodic potential of 4.5 V

3.4.4 Characterization of electrochemical regions from I-V curves

The observed variation of MRR, and the surface morphology and roughness with the applied voltage may be traced back to the electrochemical phase prevailing during the specified process conditions. The trends of the I-V characteristics (Figure 3.14) can be used to identify the process conditions, and hence track MRR, Ra and other quality and

performance variables of ECMP process in real-time. In contrast with prevailing approaches to delineate I-V characteristics, we not only capture the first moment, averaged trend, but also capture time-frequency patterns of the current signals at various applied voltage conditions. As shown in Figure 4.4, the first moment trend indicates that for low applied voltage of < 1 V; the average current of < 0.005 A was noted, corresponding to active dissolution. The average current exhibits a slight increase as the voltage is increased to 2 V. Upon further increase in anodic voltage to 3 V, the current shows a marked increase (average current of 0.08 A at 3 V), and increases linearly until 5 V. Upon further increase, the increasing trend becomes somewhat sharper, suggesting a transition from a transient to trans-passive electrochemical phase.

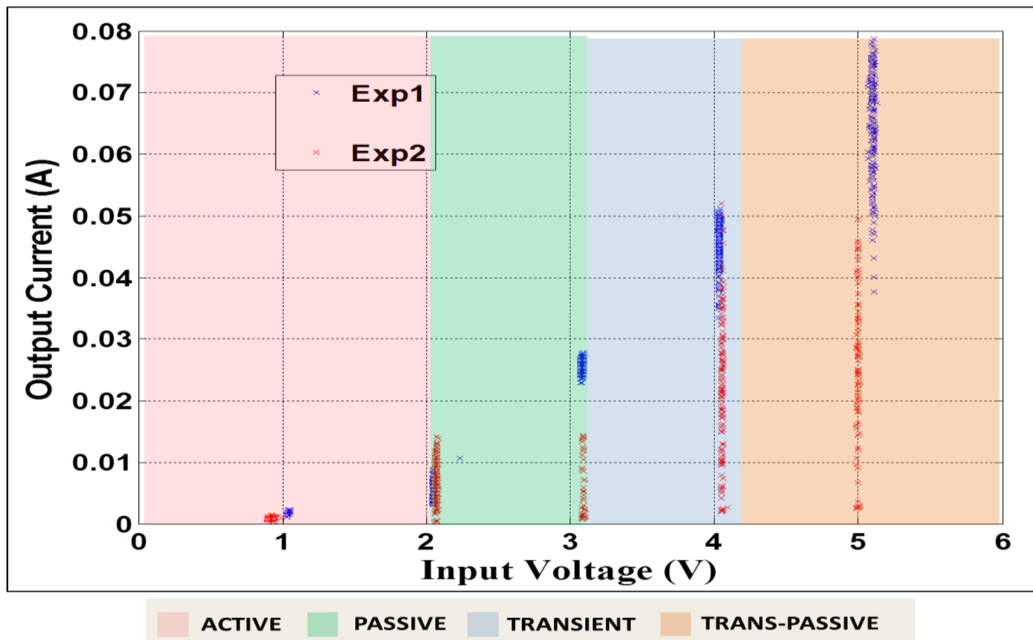

Figure 3.14: I-V curves of H_3PO_4 electrolyte under different voltage conditions

CHAPTER IV

MOLECULAR DYNAMICS STUDY ON Cu-ECMP PROCESS

4.1 Description of the molecular system

Here we consider the effects of the applied voltage on the shape and the trajectory of an isolated copper (II) hexa hydrate $Cu[(H_2O)_6]^{2+}$ complex molecular system. The potentials were adapted based on the previous work done by Natalia *et al.,* [98]. In this work, the intermolecular and intramolecular potentials depicting the water-water interaction and O-H interaction have been considered. Also harmonic potential function to depict the stretching and bending of the water molecules have also been considered. The molecule is simulated at room temperature condition (298K). From the mobility and velocity of Cu^{2+}, the current carried by the Cu^{2+} can be computed. With further extension of this model i.e., by determining the current carried by H^+ and PO_4^{3-} we can calculate the total current of the system. If MRR can be expressed as a function of total current, then the MRR can be predicted at different voltage conditions. Furthermore from I-V characteristic curve the transition of the electrochemical phase can be elucidated.

4.2 Design of pairwise interatomic potentials

Pair potentials are appropriate for metals such as copper, aluminum and silver for atomistic simulation. Figure 4.1 shows the structure of copper (II) hydrate molecule used for determining the global minima position.

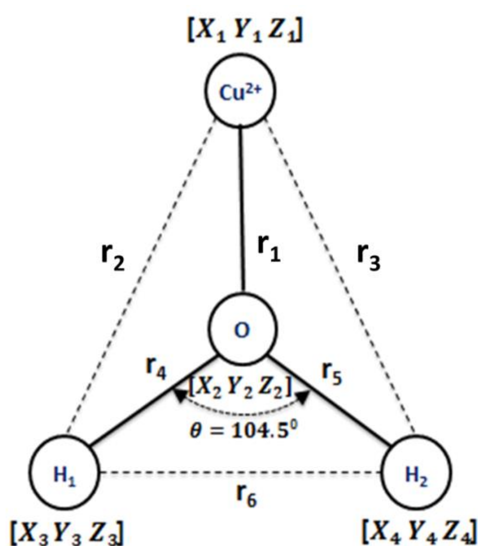

Figure 4.1: Structure of Copper (II) Hydrate molecule

The potential between Cu^{2+}—H_2O (V_2) and potential within H_2O molecule (V_{H_2O}) were modeled separately and then combined to obtain the total potential energy of the system.

The pairwise additive interaction energies between Cu^{2+}—H_2O are mathematically modeled using a multi-polar expansion, as shown in Equation 4.1. This expansion accounts for both repulsive and attractive interactions between Cu^{2+} and H_2O [98, 99].

$$V_2 = c_1\left[\frac{2q_0}{r_1} + 2q_H\left(\frac{1}{r_2}+\frac{1}{r_3}\right)\right] + c_2\left[\frac{1}{r_1^2} - \frac{1}{2}\left(\frac{1}{r_2^2}+\frac{1}{r_3^2}\right)\right] + c_3\left[\frac{1}{r_1^3} - \frac{1}{2}\left(\frac{1}{r_2^3}+\frac{1}{r_3^3}\right)\right] + \frac{c_4}{r_1^4} +$$

$$c_5\left(\frac{1}{r_2^4}+\frac{1}{r_3^4}\right) + \frac{c_6}{r_1^5} + c_7\left(\frac{1}{r_2^5}+\frac{1}{r_3^5}\right) - \frac{c_8}{r_1^6} - c_9\left(\frac{1}{r_2^6}+\frac{1}{r_3^6}\right) + \frac{c_{10}}{r_1^{12}} + c_{11}\left(\frac{1}{r_2^{12}}+\frac{1}{r_3^{12}}\right) \qquad (4.1)$$

where, q_0 is the atomic charge on oxygen = − 0.6836

q_H is the atomic charge on hydrogen = + 0.3415

r_1, r_2 and r_3 are the Cu^{2+}−O, Cu^{2+}−H_1 and Cu^{2+}−H_2 interatomic distances

Coefficients c_i (i =1,2….,11) were determined by fitting the two-body V_2 function to *ab initio* calculated interaction energies of the dimer Cu^{2+}−H_2O for 5 planar and 6 nonpolar orientations of the water molecule around Cu(II) ion [98, 99].

We can observe that from Figure 4.2 that the global minima position is at 3.8635 bohrs[1] where the energy is -0.7396 hartree[2].

[1] $1\ bohr\ radius = 5.29177 \times 10^{-11} m$
[2] $1\ hartree\ =\ 2625.5\ kJ/mol$

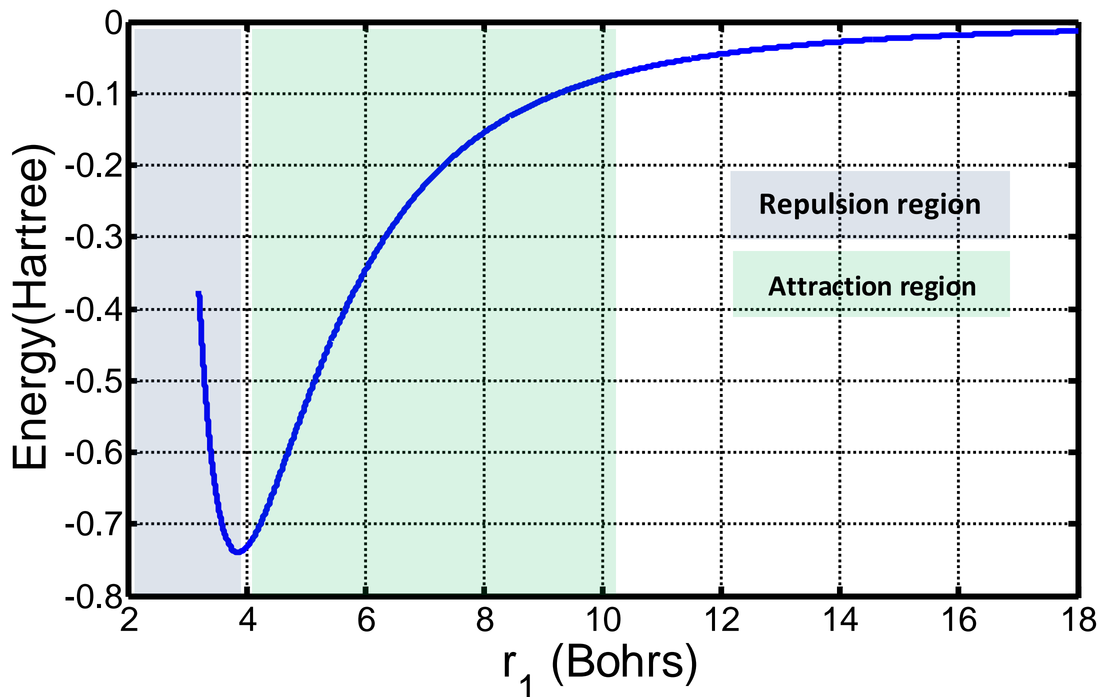

Figure 4.2: Potential Energy ($\mathbf{V_2}$) vs Cu^{2+}—O (r_1) distance.

Morse potential was used to model the pair potential between O−H_1 (r_4) and O−H_2 (r_5). A simple harmonic function of bond angle h(θ) was used to depict the bending of the H_1−O−H_2 angle ($\theta = 104.5^0$).

The mathematical expressions used for the Morse function and simple harmonic function of bond angle are given in Equations 4.2, 4.3 and 4.4.

$$V_{H_2O} = f(r_4) + f(r_5) + h(\theta)$$

where,

$$f(r_4) = D[1 - \exp(-\alpha(r_4 - r_{eq})]^2 \qquad (4.2)$$

$$f(r_5) = D[1 - \exp(-\alpha(r_5 - r_{eq})]^2 \quad (4.3)$$

$$h(\theta) = k[\theta - \theta_{eq}]^2 \quad (4.4)$$

with,

$$\mathrm{D} = \text{ Well depth (defined relative to the dissociated atoms)} = 463 \text{ kJ/mol}$$

$$= 0.1763 \text{ hartree}$$

$$\alpha = \left[\frac{2\pi^2 \mu \gamma_0^2}{\mathrm{D}}\right]^{\frac{1}{2}} = 1.145272 \text{ bohr}^{-1}$$

$$\widetilde{\gamma_b} = \text{Bending Frequency for } H_2O = 1595 \text{ cm}^{-1}$$

$$\therefore \gamma_b = \widetilde{\gamma_b}C = (1595 \text{ cm}^{-1})(2.997 \times 10^{10} \text{cm s}^{-1})$$

$$= 4.780215 \times 10^{13} \text{s}^{-1} \times \left(\frac{2.41888 \times 10^{-17} \text{ s}}{\text{Time Unit}}\right)$$

$$= 0.0015628 \text{ time unit}^{-1}$$

$$\mu = \text{Reduced mass of } H_2O = \frac{m_H m_O}{(m_H + m_O)} = 1.57 \times 10^{-27} \text{kg}$$

$$r_{eq} = \text{Equilibrium distance at stable molecular condition} = 1.8085 \text{ bohr}$$

$$k = 4\pi^2 {\gamma_b}^2 \mu r_{eq}^2 = 0.2975315 \text{ hartree}$$

$$\theta_{eq} = \text{Equilibrium bond angle at stable molecular condition} = 1.823 \text{ radians}$$

Figure 4.3 and Figure 4.4 depict the normal shape of the Morse potential and simple harmonic function of bond angle, respectively.

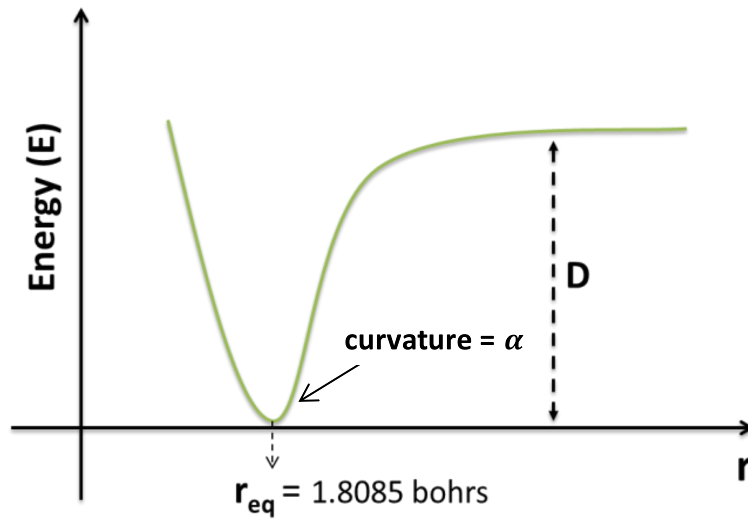

Figure 4.3: Morse potential function curve

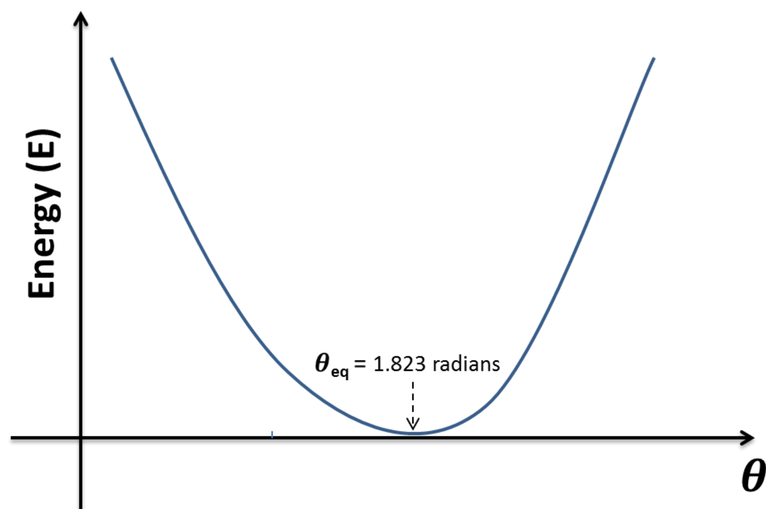

Figure 4.4: Simple harmonic function curve

Morse potential and bond angle potential were then modeled using MATLAB and the following curves were obtained with variation of length of O—H_1 (r_4) and theta (θ).

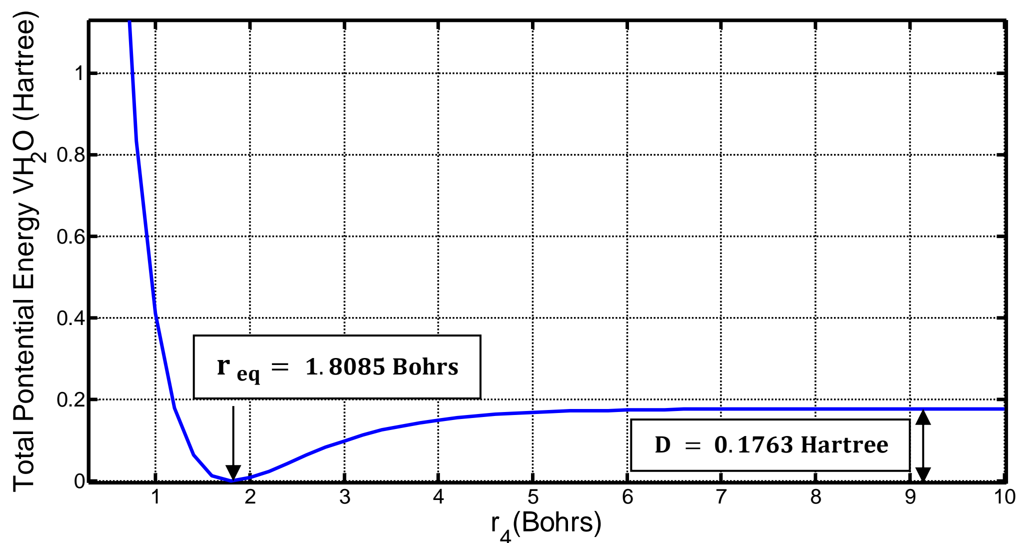

Figure 4.5: Morse potential curve for $[\mathbf{Cu(H_2O)}]^{2+}$ system in equilibrium position

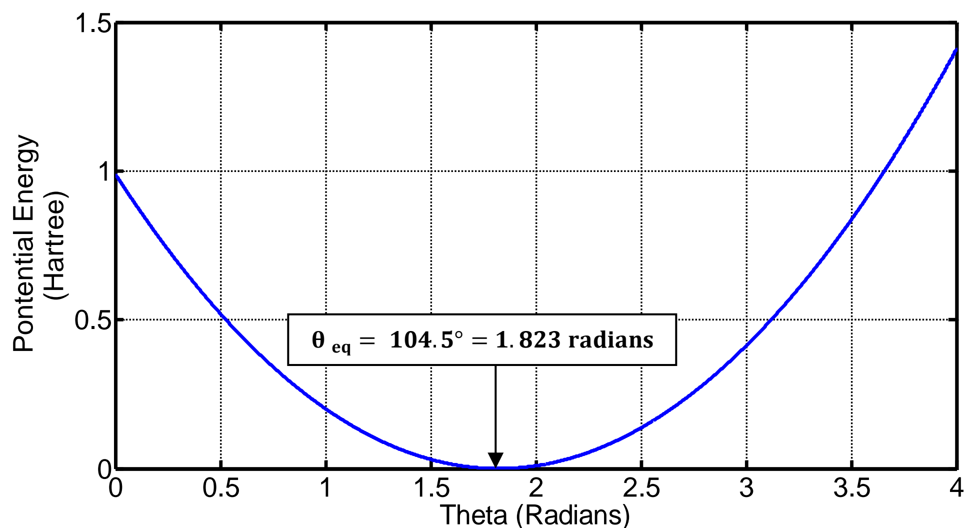

Figure 4.6: Bond angle potential curve for $[\mathbf{Cu(H_2O)}]^{2+}$ system in equilibrium position

At this point, the total potential energy of the system (V_{TOT}) is computed from the summation of V_2 and V_{H_2O} potential over 'n' water molecules.

$$V_{TOT} = \sum_{i=1}^{N}(V_2) + \sum_{i=1}^{2N}\left(V_{H_2O}\right) \tag{4.5}$$

4.3 Atomic force computation

The force on acting on an atom is computed as the negative first order derivative of the potential function V i.e., the negative slope of the potential energy curve.

The partial differential equations of $\mathbf{V_2}$ with respect to $\mathbf{r_1}$, $\mathbf{r_2}$ and $\mathbf{r_3}$ are computed as shown below,

$$\frac{\partial V_2}{\partial r_1} = -\frac{2C_1q_0}{r_1^2} - \frac{C_2}{r_1^3} - \frac{C_3}{r_1^4} - \frac{C_4}{r_1^5} - \frac{C_6}{r_1^6} + \frac{C_8}{r_1^7} - \frac{C_{10}}{r_1^{13}}$$

$$\frac{\partial V_2}{\partial r_2} = -\frac{2C_1q_H}{r_2^2} + \frac{0.5C_2}{r_2^3} + \frac{1.5C_3}{2r_2^4} - \frac{4C_5}{r_2^5} - \frac{5C_7}{r_2^6} + \frac{6C_9}{r_2^7} - \frac{12C_{11}}{r_2^{13}}$$

$$\frac{\partial V_2}{\partial r_3} = -\frac{2C_1q_H}{r_3^2} + \frac{0.5C_2}{r_3^3} + \frac{1.5C_3}{2r_3^4} - \frac{4C_5}{r_3^5} - \frac{5C_7}{r_3^6} + \frac{6C_9}{r_3^7} - \frac{12C_{11}}{r_3^{13}}$$

The partial differential equations of $\mathbf{V_{H_2O}}$ with respect to $\mathbf{r_4}$, $\mathbf{r_5}$ and $\mathbf{r_6}$ are computed as shown below,

$$\frac{\partial V_{H_2O}}{\partial r_4} = \frac{\partial f(r_4)}{\partial r_4} + \left[\left(\frac{\partial h(\theta)}{\partial \theta}\right) \cdot \left(\frac{\partial \theta}{\partial r_4}\right)\right]$$

$$\frac{\partial V_{H_2O}}{\partial r_5} = \frac{\partial f(r_5)}{\partial r_5} + \left[\left(\frac{\partial h(\theta)}{\partial \theta}\right) \cdot \left(\frac{\partial \theta}{\partial r_5}\right)\right]$$

$$\frac{\partial V_{H_2O}}{\partial r_6} = \left[\left(\frac{\partial h(\theta)}{\partial \theta}\right) \cdot \left(\frac{\partial \theta}{\partial r_6}\right)\right]$$

The distance between the Cartesian coordinates of Particle **1** $[X_1\ Y_1\ Z_1]$ and Particle $\boldsymbol{\alpha}$ $[X_\alpha\ Y_\alpha\ Z_\alpha]$ i.e., $r_{1\alpha}$is calculated as shown in Eq. 4.6.

$$r_{1\alpha}^2 = [(X_1 - X_\alpha)^2 + (Y_1 - Y_\alpha)^2 + (Z_1 - Z_\alpha)^2] \quad (4.6)$$

Differentiating (Eq. 4.7) partially with respect to $r_{1\alpha}$ we get,

$$2\ r_{1\alpha}\left(\frac{\partial r_{1\alpha}}{\partial X_1}\right) = 2(X_1 - X_\alpha)$$

$$\left(\frac{\partial r_{1\alpha}}{\partial X_1}\right) = \frac{(X_1 - X_\alpha)}{r_{1\alpha}} \quad (4.7)$$

$$\therefore \left(\frac{\partial r_{1\alpha}}{\partial X_1}\right) = \left(\frac{X_1 - X_\alpha}{[(X_1 - X_\alpha)^2 + (Y_1 - Y_\alpha)^2 + (Z_1 - Z_\alpha)^2]^{\frac{1}{2}}}\right)$$

Likewise, we can find other partial derivatives of r_1, r_2, r_3 with respect to Y and Z directions.

The force along X, Y and Z axis was then determined using 12 chain rule derivatives. They are $\left\{\begin{matrix}\left(\frac{\partial V_2}{\partial X_i}\right)\\ \left(\frac{\partial V_2}{\partial Y_i}\right)\\ \left(\frac{\partial V_2}{\partial Z_i}\right)\end{matrix}\right\}$ where $1 \le i \le 4$, so totally there will be 4 derivatives for the force calculation, along every axis.

Force along X axis i.e., $F_X = \frac{\partial V}{\partial X_i}$

$$\frac{\partial V}{\partial X_1} = \left(\frac{\partial V_2}{\partial r_1} \cdot \frac{\partial r_1}{\partial X_1}\right) + \left(\frac{\partial V_2}{\partial r_2} \cdot \frac{\partial r_2}{\partial X_1}\right) + \left(\frac{\partial V_2}{\partial r_3} \cdot \frac{\partial r_3}{\partial X_1}\right)$$

$$\frac{\partial V}{\partial X_2} = \left(\frac{\partial V_2}{\partial r_1} \cdot \frac{\partial r_1}{\partial X_2}\right) + \left(\frac{\partial V_{H_2O}}{\partial r_4} \cdot \frac{\partial r_4}{\partial X_2}\right) + \left(\frac{\partial V_{H_2O}}{\partial r_5} \cdot \frac{\partial r_5}{\partial X_2}\right)$$

$$\frac{\partial V}{\partial X_3} = \left(\frac{\partial V_2}{\partial r_2} \cdot \frac{\partial r_2}{\partial X_3}\right) + \left(\frac{\partial V_{H_2O}}{\partial r_4} \cdot \frac{\partial r_4}{\partial X_3}\right) + \left(\frac{\partial V_{H_2O}}{\partial r_6} \cdot \frac{\partial r_6}{\partial X_3}\right)$$

$$\frac{\partial V}{\partial X_4} = \left(\frac{\partial V_2}{\partial r_3} \cdot \frac{\partial r_3}{\partial X_4}\right) + \left(\frac{\partial V_{H_2O}}{\partial r_5} \cdot \frac{\partial r_5}{\partial X_4}\right) + \left(\frac{\partial V_{H_2O}}{\partial r_6} \cdot \frac{\partial r_6}{\partial X_4}\right)$$

Force along Y axis i.e., $F_Y = \frac{\partial V}{\partial Y_i}$

$$\frac{\partial V}{\partial Y_1} = \left(\frac{\partial V_2}{\partial r_1} \cdot \frac{\partial r_1}{\partial Y_1}\right) + \left(\frac{\partial V_2}{\partial r_2} \cdot \frac{\partial r_2}{\partial Y_1}\right) + \left(\frac{\partial V_2}{\partial r_3} \cdot \frac{\partial r_3}{\partial Y_1}\right)$$

$$\frac{\partial V}{\partial Y_2} = \left(\frac{\partial V_2}{\partial r_1} \cdot \frac{\partial r_1}{\partial Y_2}\right) + \left(\frac{\partial V_{H_2O}}{\partial r_4} \cdot \frac{\partial r_4}{\partial Y_2}\right) + \left(\frac{\partial V_{H_2O}}{\partial r_5} \cdot \frac{\partial r_5}{\partial Y_2}\right)$$

$$\frac{\partial V}{\partial Y_3} = \left(\frac{\partial V_2}{\partial r_2} \cdot \frac{\partial r_2}{\partial Y_3}\right) + \left(\frac{\partial V_{H_2O}}{\partial r_4} \cdot \frac{\partial r_4}{\partial Y_3}\right) + \left(\frac{\partial V_{H_2O}}{\partial r_6} \cdot \frac{\partial r_6}{\partial Y_3}\right)$$

$$\frac{\partial V}{\partial Y_4} = \left(\frac{\partial V_2}{\partial r_3} \cdot \frac{\partial r_3}{\partial Y_4}\right) + \left(\frac{\partial V_{H_2O}}{\partial r_5} \cdot \frac{\partial r_5}{\partial Y_4}\right) + \left(\frac{\partial VH_2O}{\partial r_6} \cdot \frac{\partial r_6}{\partial Y_4}\right)$$

Force along Z axis i.e., $F_Z = \frac{\partial V}{\partial Y_i}$

$$\frac{\partial V}{\partial Z_1} = \left(\frac{\partial V_2}{\partial r_1} \cdot \frac{\partial r_1}{\partial Z_1}\right) + \left(\frac{\partial V_2}{\partial r_2} \cdot \frac{\partial r_2}{\partial Z_1}\right) + \left(\frac{\partial V_2}{\partial r_3} \cdot \frac{\partial r_3}{\partial Z_1}\right)$$

$$\frac{\partial V}{\partial Z_2} = \left(\frac{\partial V_2}{\partial r_1} \cdot \frac{\partial r_1}{\partial Z_2}\right) + \left(\frac{\partial V_{H_2O}}{\partial r_4} \cdot \frac{\partial r_4}{\partial Z_2}\right) + \left(\frac{\partial V_{H_2O}}{\partial r_5} \cdot \frac{\partial r_5}{\partial Z_2}\right)$$

$$\frac{\partial V}{\partial Z_3} = \left(\frac{\partial V_2}{\partial r_2} \cdot \frac{\partial r_2}{\partial Z_3}\right) + \left(\frac{\partial V_{H_2O}}{\partial r_4} \cdot \frac{\partial r_4}{\partial Z_3}\right) + \left(\frac{\partial V_{H_2O}}{\partial r_6} \cdot \frac{\partial r_6}{\partial Z_3}\right)$$

$$\frac{\partial V}{\partial Z_4} = \left(\frac{\partial V_2}{\partial r_3} \cdot \frac{\partial r_3}{\partial Z_4}\right) + \left(\frac{\partial V_{H_2O}}{\partial r_5} \cdot \frac{\partial r_5}{\partial Z_4}\right) + \left(\frac{\partial V_{H_2O}}{\partial r_6} \cdot \frac{\partial r_6}{\partial Z_4}\right)$$

For simplicity, let us represent the first order derivatives of the potential energy with respect to all atoms in the X, Y and Z direction as Eq. 4.8

$$\left.\begin{matrix} \left(\frac{\partial V}{\partial X_i}\right) \\ \left(\frac{\partial V}{\partial Y_i}\right) \\ \left(\frac{\partial V}{\partial Z_i}\right) \end{matrix}\right\} \qquad (4.8)$$

In order to verify the correctness and accuracy of the values of derivatives, a 7-point slope method was adopted as shown in Figure 4.7.

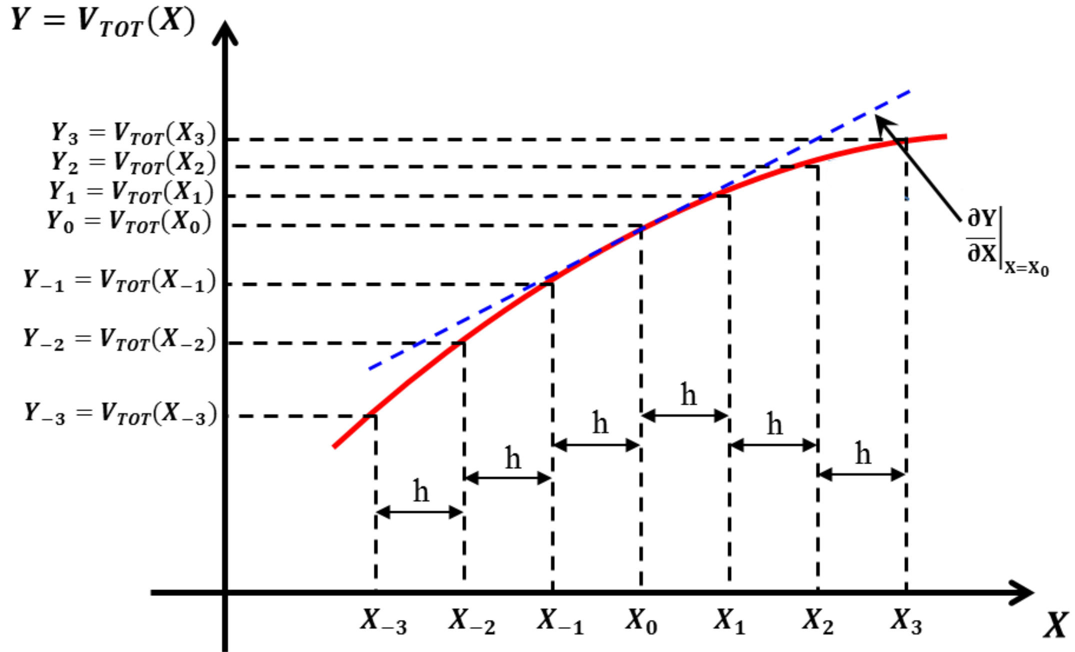

Figure 4.7: Graphical depiction of 7-point slope method

Figure 4.7 depicts a graphical representation of a 7-point slope method. The X axis represents the change in the X coordinates of the atoms. The Y axis contains the corresponding Potential energy values calculated using the V_{TOT} function (Eq. 4.5) based upon different positions of the atoms. The method is based on the computation of S_1, S_2 and S_3 can be found from Equations 4.9, 4.10 and 4.11, where h = 0.0005.

$$S_1 = \frac{(Y_1 - Y_{-1})}{h} \tag{4.9}$$

$$S_2 = \frac{(Y_2 - Y_{-2})}{h} \tag{4.10}$$

$$S_3 = \frac{(Y_3 - Y_{-3})}{h} \tag{4.11}$$

If the red curve shown in Figure 4.7 can be accurately fitted with a polynomial expansion in X of order 6 or less, then it can be rigorously shown that

$$\left.\frac{\partial \mathrm{Y}}{\partial \mathrm{X}}\right|_{\mathrm{X}=\mathrm{X}_0} = 0.75S_1 - 0.15S_2 + 0.01666S_3 \tag{4.12}$$

The results obtained from the comparison between the values computed from the derivatives shown in Eq. 8 and the values of the slope computed using 7-point slope method is presented in Table 1. Two water molecules have been considered for this test. So there are 7 atoms in this test model, which are designated as shown below,

1 – Cu^{2+} ion, **2** – O of the first water molecule, **3** – H_1 of the first water molecule, **4** – H_2 of the first water molecule, **5** – O of the second water molecule, **6** – H_1 of the second water molecule, **7** – H_2 of the second water molecule.

Table 4.1: Comparison table between Q_i values and 7-point slope method. All values are given in units of hartree $bohr^{-1}$.

Derivative of V with respect to atoms	Values computed from derivatives – Eq. 8	Values computed from 7-point slope method – Eq.12
$\partial V/ \partial X_1$	3.74647773971345E-10	3.74648789071506E-10
$\partial V/ \partial Y_1$	-4.55040393490804E-06	-4.55040393228684E-06
$\partial V/ \partial Z_1$	8.75514604295787E-09	8.75514604244237E-06
$\partial V/ \partial X_2$	2.26679800811792E-06	2.26679800728777E-06
$\partial V/ \partial Y_2$	4.46613209182386E-06	4.46613208940395E-06
$\partial V/ \partial Z_2$	-2.15011102692851E-08	-2.22631485868115E-06
$\partial V/ \partial X_3$	-2.21996213183842E-06	-2.21996213073261E-06
$\partial V/ \partial Y_3$	8.20151222379824E-09	8.20151179567898E-09
$\partial V/ \partial Z_3$	-3.19980359269939E-06	-3.19980359114016E-06
$\partial V/ \partial X_4$	6.15654086177955E-09	6.15654086482174E-06
$\partial V/ \partial Y_4$	1.59399220685803E-06	1.59399220618633E-06
$\partial V/ \partial Z_4$	1.35498613388521E-06	1.35498613379016E-06
$\partial V/ \partial X_5$	-6.52325226371036E-09	-6.57444815102026E-07*
$\partial V/ \partial Y_5$	-6.73517451912826E-07	-6.73517451390600E-07
$\partial V/ \partial Z_5$	6.41019405924549E-09	6.41019713447353E-09
$\partial V/ \partial X_6$	2.45635508271192E-06	2.45635508017717E-06
$\partial V/ \partial Y_6$	-1.97733906912618E-08	-1.97733906255392E-06
$\partial V/ \partial Z_6$	-1.21798071070880E-06	-1.21798070945804E-06
$\partial V/ \partial X_7$	-3.89824017398553E-06	-3.89824017265228E-06
$\partial V/ \partial Y_7$	8.32173805208994E-10	1.93648081453384E-06
$\partial V/ \partial Z_7$	1.94442893592877E-06	1.94442893514135E-06

*7 point slope method is based on the difference between the potential, so cannot be always accurate

From Table 1 we can observe that the accuracy is of the order of 9 significant digits for derivatives whose magnitude is ≥ 10^{-6} hartree bohr^{-1}. For derivatives whose magnitude is ≤ 10^{-9} hartree bohr^{-1}, Eq.12 is not sufficiently accurate to evaluate $\partial V/\partial X$.

4.4 Initial spherical polar coordinates assignment

Initially, the coordinates of the atoms were assigned arbitrarily to validate whether the model complies with the Law of conservation of Energy.

The initial position of Cu^{2+} ion was taken to be origin [0 0 0]. Next, the Cu−O distance for each of the N oxygen atoms was taken to be the equilibrium Cu^{2+}−O distance obtained from Figure 4.1. The rotation angle, θ and $\emptyset$, for vector $\vec{R}$ were assigned randomly. Figure 4.8 illustrates the process.

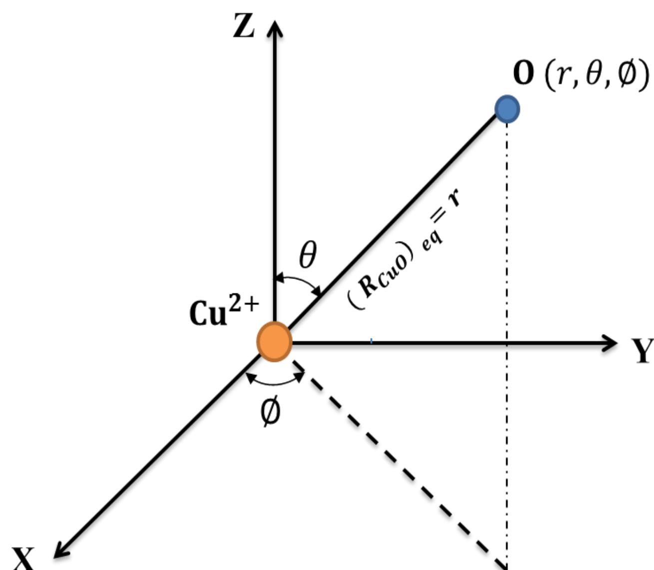

Figure 4.8: Spherical polar coordinates arrangement

From Figure 4.8, the Cartesian coordinates of oxygen are

$$X_O = R_{CuO} \cdot \sin\theta \cdot \cos\emptyset$$

$$Y_O = R_{CuO} \cdot \sin\theta \cdot \sin\emptyset$$

$$Z_O = R \cdot \cos\theta$$

We can then cover all possible angles by using,

$$0 \leq \theta \leq \pi \text{ and}$$

$$0 \leq \emptyset \leq 2\pi.$$

In order to initially position the atoms, we use a random number $0 \leq \zeta \leq 1$ and select the azimuthal and rotational angle in the following manner,

$$\theta_i = \zeta_i \cdot \pi; \quad \emptyset_i = \zeta \cdot 2\pi \quad (i = 1, 2, 3\ldots, \mathrm{N})$$

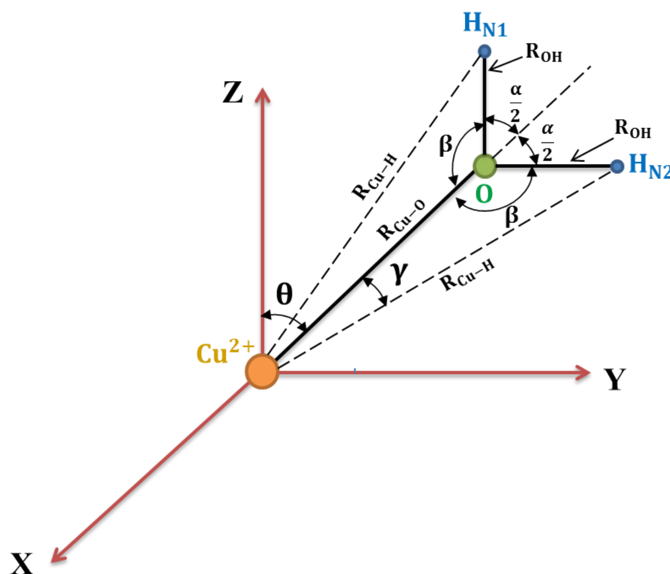

Figure 4.9: Spherical polar coordinates initialization based on angles

The hydrogen atoms attached to each oxygen are initially taken to be in the (Y, Z) plane so that we have the coordinates of the O, H_1 and H_2 as,

O coordinates = $\begin{pmatrix} 0 \\ R_{CuO}\sin\theta \\ R_{CuO}\cos\theta \end{pmatrix}$, H_1 coordinates = $\begin{pmatrix} 0 \\ Y_3 \\ Z_3 \end{pmatrix}$ and H_2 coordinates = $\begin{pmatrix} 0 \\ Y_4 \\ Z_4 \end{pmatrix}$

From Figure 4.9, using the law of cosines, we have,

$$(R_{CuH})^2 = (R_{CuO})^2 + (R_{OH})^2 - 2 \cdot R_{CuO} \cdot R_{OH} \cdot \text{Cos}\beta$$

$$(R_{OH})^2 = (R_{CuO})^2 + (R_{CuH})^2 - 2 \cdot R_{CuO} \cdot R_{CuH} \cdot \text{Cos}\gamma$$

$$\text{Cos}\gamma = \left[\frac{(R_{CuH})^2 + (R_{CuO})^2 - (R_{OH})^2}{2 \cdot R_{CuO} \cdot R_{CuH}}\right]$$

$$\therefore \gamma = \cos^{-1}\left[\frac{(R_{CuH})^2 + (R_{CuO})^2 - (R_{OH})^2}{2 \cdot R_{CuO} \cdot R_{CuH}}\right]$$

From Figure 4.8, we can also determine the values of $\boldsymbol{\theta_{H_{N1}}}$ as $\boldsymbol{\theta - \gamma}$ and $\boldsymbol{\theta_{H_{N2}}}$ as $\boldsymbol{\theta + \gamma}$, which gives

Coordinates of H_1 = $\begin{pmatrix} 0 \\ R_{CuH} \cdot \sin\theta_{H_{N1}} \\ R_{CuH} \cdot \cos\theta_{H_{N1}} \end{pmatrix}$ and coordinates of H_2 = $\begin{pmatrix} 0 \\ R_{CuH} \cdot \sin\theta_{H_{N2}} \\ R_{CuH} \cdot \cos\theta_{H_{N2}} \end{pmatrix}$

After assigning the initial coordinates of O, H_1 and H_2, we need to rotate the H_2O molecule about the Z axis through a rotational angle $\emptyset'$ selected when O atoms were positioned.

In this case, $\emptyset' = \left(\frac{\boldsymbol{\pi}}{\mathbf{2}} - \emptyset\right)$**.** The coordinates of O, H_1 and H_2 are then rotated with the aid of a rotational matrix $R_Z(\emptyset')$, where

$$R_Z(\emptyset') = \begin{bmatrix} \cos\emptyset' & \sin\emptyset' & 0 \\ -\sin\emptyset' & \cos\emptyset' & 0 \\ 0 & 0 & 1 \end{bmatrix}.$$

For instance, let us examine how the rotational operation is performed for the O_N coordinates.

The initial coordinates for O_N are $\begin{pmatrix} 0 \\ Y_o \\ Z_o \end{pmatrix}$. Let the final coordinates of O after rotation be $\begin{pmatrix} X_O \\ Y_O \\ Z_O \end{pmatrix}$.

$$\therefore \begin{pmatrix} X_O \\ Y_O \\ Z_O \end{pmatrix} = R_Z(\emptyset') \cdot \begin{pmatrix} 0 \\ Y_o \\ Z_o \end{pmatrix} = \begin{bmatrix} R_{CuO}\sin\theta\sin\left(\frac{\pi}{2} - \emptyset\right) \\ R_{CuO}\sin\theta\cos\left(\frac{\pi}{2} - \emptyset\right) \\ Z_o \end{bmatrix} = \begin{bmatrix} R_{CuO}\sin\theta\sin\emptyset' \\ R_{CuO}\sin\theta\cos\emptyset' \\ Z_o \end{bmatrix}$$

Figure 4.10 shows the structure of copper (II) hexa hydrate complex molecule used for the energy conservation verification test. The magenta sphere denotes the copper (II) ion, red spheres denote the oxygen atoms and green spheres denote the hydrogen atoms.

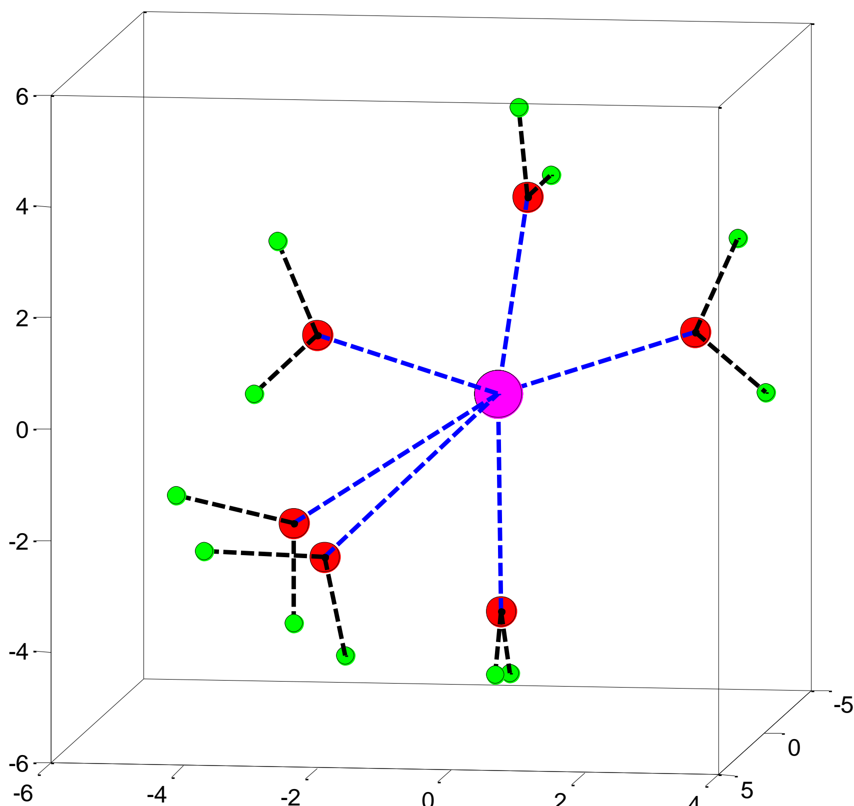

Figure 4.10: Copper (II) hexa hydrate complex molecule with randomly assigned positions based on angles and bond length

4.5 Initial momentum assignment and kinetic energy calculation

To test the derivatives and integration accuracy, we initially assign thermal energy at 298K to each of the atoms.

Let E be the initial energy assigned to the system, M be the mass of the atom, v is the velocity, R is the gas constant = 8.314 $J\ mol^{-1}K^{-1}$ and T is the system temperature = 298 K. In a thermal system, the average kinetic energy ⟨T⟩

$$\langle T\rangle = \langle\frac{1}{2}Mv^2\rangle = \frac{M}{2}\langle v^2\rangle = \frac{3}{2}\cdot RT$$

The average square velocity of the system (v) can be calculated based on the positive square root of the sum of square of velocity components along X, Y and Z directions i.e., v_X, v_Y and v_Z as shown in Eq. 4.12 (a)

$$\langle v^2\rangle = \langle\frac{3RT}{M}\rangle\ m^2s^{-2}$$

$$\langle v^2\rangle^{\frac{1}{2}} = \left[\frac{3RT}{M}\right]^{\frac{1}{2}} m/s$$

$$\langle v^2\rangle^{\frac{1}{2}} = \langle v_X^2 + v_Y^2 + v_Z^2\rangle^{\frac{1}{2}} = \langle 3v_X^2\rangle^{\frac{1}{2}} = \sqrt{3}\langle {v_X}^2\rangle^{\frac{1}{2}} \qquad (4.21\ a)$$

where, we assume an equipartitioning of kinetic energy among the three translation degrees of freedom.

$$\langle v_X\rangle^{\frac{1}{2}} = \frac{1}{\sqrt{3}}\langle v^2\rangle^{\frac{1}{2}} = \frac{1}{\sqrt{3}}\left[\frac{3RT}{M}\right]^{\frac{1}{2}} = \pm\left[\frac{RT}{M}\right]^{\frac{1}{2}} m/s \qquad (4.13)$$

The signs of $\left[\frac{RT}{M}\right]^{\frac{1}{2}}$ are chosen randomly.

The momentum components along X, Y and Z directions i.e., P_X, P_Y and P_Z are calculated based on the mass of the atom and corresponding momenta component.

$$\langle P_X\rangle = m_X\langle {v_X}^2\rangle^{\frac{1}{2}}$$

The units of velocity ($m\,s^{-1}$) are then converted into bohrs/time unit by the following conversion calculation.

$$\langle v_X^2\rangle^{\frac{1}{2}}\ \mathrm{m\ s^{-1}} \times \left[\frac{100\ \mathrm{cm}}{\mathrm{m}}\right] \times \left[\frac{10^{8}\ \mathrm{A^{o}}}{\mathrm{cm}}\right] \times \left[\frac{1\ \mathrm{bohr}}{0.5429171\ \mathrm{A^{o}}}\right] \times \left[\frac{1\ \mathrm{bohr}}{0.5429171\ \mathrm{A^{o}}}\right] \times \left[\frac{2.41888 \times 10^{-17}}{1\ \mathrm{Time\ unit}}\right] =$$

$$\langle v_X^2\rangle^{\frac{1}{2}}\ \mathrm{bohr/\ time\ unit}$$

The mass of the atoms are converted into atomic mass unit (amu) as shown below for oxygen atom.

$$m_O = \frac{16.0\ g\ mol^{-1}}{6.022 \times 10^{23} mol^{-1}} \cdot \left[\frac{1\ amu}{9.10939 \times 10^{-28} g}\right] = 1\ amu$$

From the above calculation procedure, the magnitude of the momentum along X, Y and Z direction will be equal for individual atoms whereas the signs would be randomly designated i.e., $|P_X| = |P_Y| = |P_Z|$

The kinetic energy is then calculated by the summation of momentum values and mass of atoms over 'n' water molecules.

$$\text{Kinetic Energy, } \langle T\rangle = \sum_{i=1}^{n} \frac{P_i^2}{2m_i} \qquad (4.14)$$

where, $P_i^2 = P_{X_i}^2 + P_{Y_i}^2 + P_{Z_i}^2$

m_i = mass of Cu^{2+} m_{Cu} (or) mass of Oxygen m_O (or) mass of Hydrogen m_H

∴ The total energy of the system (E_{TOT}) will be the sum of potential energy and kinetic energy.

$$E_{TOT\ \text{at time (t)=0}} = V_{TOT} + \langle T\rangle$$

4.6 Calculation of trajectory

In order to test the integration accuracy of the model, we need to numerically integrate the coupled first-order differential equations of coordinates and momentum.

From Eq. 4.8 we have the first order derivatives of potential with respect to every atom. Equations 4.15, 4.16 and 4.17 depict the first-order time derivatives used for assigning the momentum to the atoms in the new position.

$$\frac{\partial P_{X_i}}{\partial t} = -\left(\frac{\partial V}{\partial X_i}\right) = \dot{P_{X_i}} \quad (4.15)$$

$$\frac{\partial P_{Y_i}}{\partial t} = -\left(\frac{\partial V}{\partial X_i}\right) = \dot{P_{Y_i}} \quad (4.16)$$

$$\frac{\partial P_{Z_i}}{\partial t} = -\left(\frac{\partial V}{\partial X_i}\right) = \dot{P_{Z_i}} \quad (4.17)$$

For convenience, let us denote $\dot{P_{X_i}}$, $\dot{P_{Y_i}}$ and $\dot{P_{Z_i}}$ together as P_i. The time derivative for the coordinates of the atoms can be determined from Equations 4.18, 4.19 and 4.20

$$\frac{\partial X_i}{\partial t} = \frac{P_{X_i}}{m_i} = \dot{X_i} \quad (4.18)$$

$$\frac{\partial Y_i}{\partial t} = \frac{P_{Y_i}}{m_i} = \dot{Y_i} \quad (4.19)$$

$$\frac{\partial Z_i}{\partial t} = \frac{P_{Z_i}}{m_i} = \dot{Z_i} \quad (4.20)$$

Let us denote Equation 4.18, 4.19 and 4.20 i.e.,$\dot{X_i}$, $\dot{Y_i}$ and $\dot{Z_i}$ as Q_i.

P_i and Q_i together constitute the coupled, first-order differential equations known as the Hamilton's equations of motion. They constitute the working equation for most trajectory calculations. In order to calculate the trajectory, Hamilton's equations of motion have to be numerically integrated from an initial state in the configuration space to some final state that lies in the configuration space.

The general form of Hamilton's equations is,

$$\frac{dY}{dt} = f[y_1, y_2 \ldots\ldots\ldots y_{6N}, t]$$

where the elements of Y are the coordinates and their conjugate momenta:

$$Y_i = Q_i \qquad (i = 1, 2, \ldots\ldots, 3N)$$

$$Y_i = P_i \qquad (i = 3N + 1, 3N + 2, \ldots\ldots, 6N)$$

Generally, the values of all elements of Y will be known at the initial condition when time $t = t_0$. In our simulation model we are using 4th order Runge-Kutta method. In this method the value of Y_i at $t = t_0 + h$ (where h is the step size) is taken as

$$Y_i(t_0 + h) = Y_i(t_0) + \frac{h[a_1 k_1^i + a_2 k_2^i + a_3 k_3^i + a_4 k_4^i]}{(a_1 + a_2 + a_3 + a_4)},$$

where,

$$k_1^i = f_i[y_1^0, y_2^0, \ldots\ldots, y_{6N}^0, t_0],$$

$$k_2^i = f_i\left[Y_1^0 + \frac{k_1^1}{2},\ Y_2^0 + \frac{k_1^2}{2}, \ldots, Y_{6N}^0 + \frac{k_1^{6N}}{2}, t_0 + \frac{h}{2}\right],$$

$$k_3^i = f_i\left[Y_1^0 + \frac{k_2^i}{2},\ Y_2^0 + \frac{k_2^2}{2}, \ldots, Y_{6N}^0 + \frac{k_2^{6N}}{2}, t_0 + \frac{h}{2}\right],$$

$$k_4^i = f_i\left[Y_1^0 + k_3^1,\ Y_2^0 + k_3^2, \ldots, Y_{6N}^0 + k_3^{6N}, t_0 + h\right],$$

where the Y_1^0 denotes $Y_i(t_0)$, the value of Y_i at $t = t_0$

The Runge-Kutta procedure has several advantages. First, it is "self-starting" in that it is unnecessary to know the values of the elements of Y at times prior to $t = t_0$. Second, the local error in a given integration step is of the order h^5. The method therefore provides good accuracy. Finally, the method is stable and easy to program. The two major disadvantages of the this method are

(1) It provides no estimate of the accuracy being achieved during the integration, and
(2) 24N derivatives must be evaluated in each integration step, where N is the number of atoms in the model. Consequently, the method would appear to be very demanding of computer time.

In our model, there are 6 water molecules and one Cu^{2+} ion, so in total 19 atoms. Hence, there will be 57 first-order differential equations defining temporal variation of the coordinates and 57 first-order differential equations used for defining time dependence of the conjugate momentum of the atoms. The Y_i would have totally 114

elements, which have to be numerically integrated over time, t. In our simulation, 1 atomic time unit = 2.41888×10^{-17} s, which is determined by our choice of energy, mass, and distance units to be hartrees, atomic mass units, and bohrs, respectively.

4.7 Conservation of energy and back integration

The Law of conservation energy, this states that “the total amount of energy in an isolated system remains constant over time”. To verify whether the atomic model is in agreement with this law, the model was numerically integrated after providing initial momentum at room temperature as described previously. From Figure 4.11 and Figure 4.12, we can observe that the total energy (E_{TOT}) and all momentum components are constant over the entire integration time length, as required by the conservation laws. Deviations are on the order of 10^{-13} units.

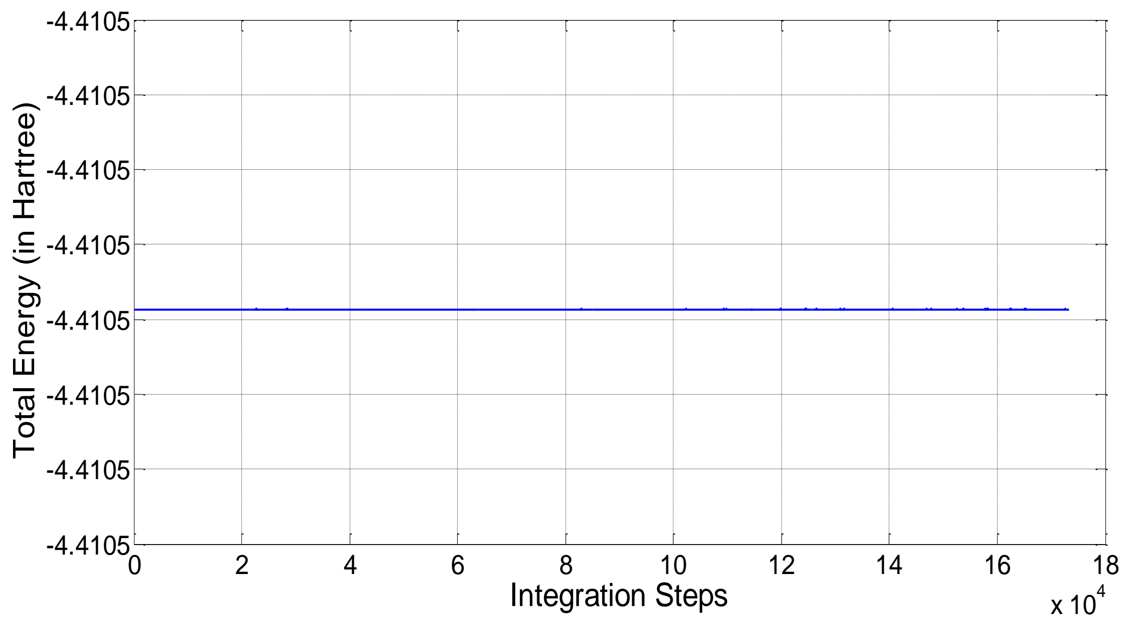

Figure 4.11: Total Energy conservation of the [Cu (H_2O) $_6$]$^{2+}$ system

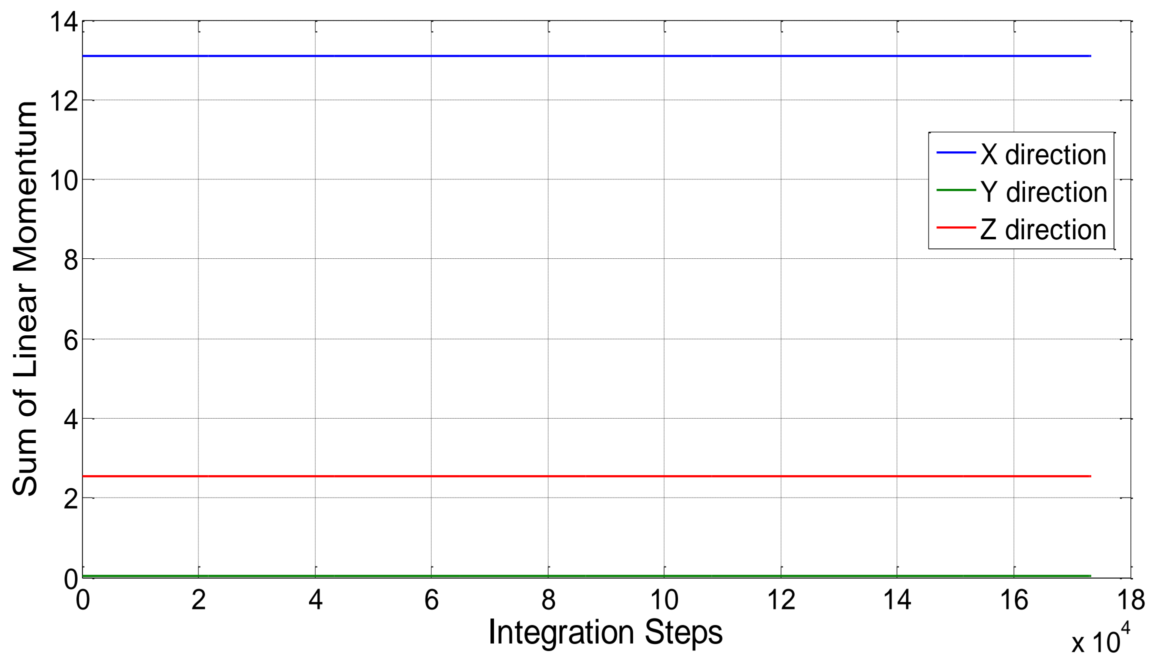

Figure 4.12: Conservation of Linear Momenta along X, Y and Z direction

The integration accuracy is then further tested accessed by back integration of the trajectory. In this procedure, after n integration steps, all the P_i are replaced by - P_i in Y. The trajectory is then "back integrated" n steps. The extent of agreement of the final values of the elements of Y with their corresponding initial values provides a measure of integration accuracy. In general, if an agreement to at least three significant digits is obtained, the integration will be sufficiently accurate.

First the trajectory between Cu-O ($R_{Cu\text{-}O}$) is tracked. Figure 4.13 shows the trajectory obtained as a result of forward integration with a time step of $\Delta t = 1$ time unit between an initial time, $t_0 = 0$ and final time, $t_{final} = 600$. Figure 4.14 shows the trajectory obtained as a result of backward integration with $\Delta t = 1$ between an initial time, $t_0 = 600$ and final time, $t_{final} = 0$.

We can observe from Figure 4.13 and Figure 4.14 that the trajectories perfectly overlap over each other. Next, the trajectory of $O-H_1$ is tracked, as shown in Figure 4.15 and Figure 4.16

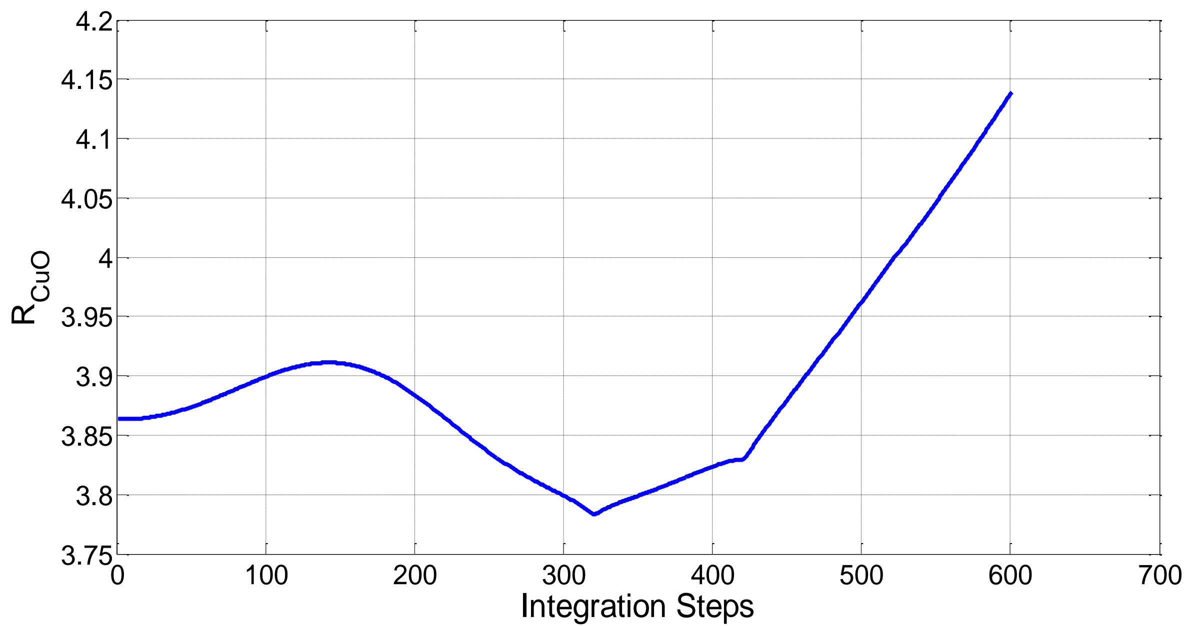

Figure 4.13: Forward integrated trajectory of Cu−O

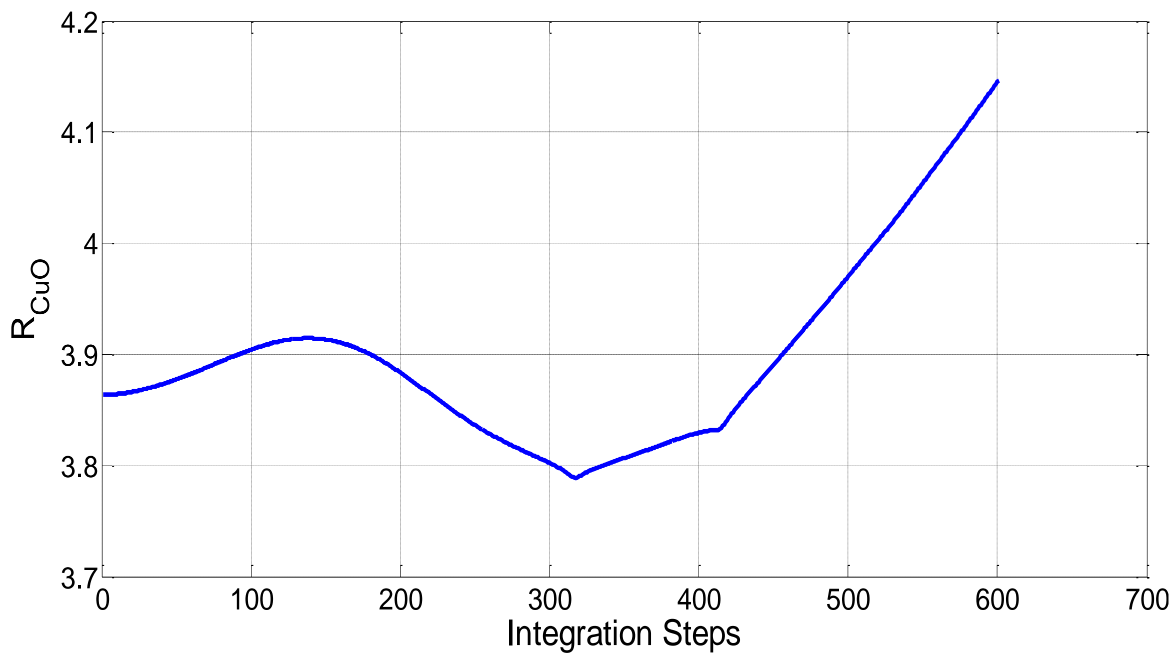

Figure 4.14: Backward integrated trajectory of Cu−O

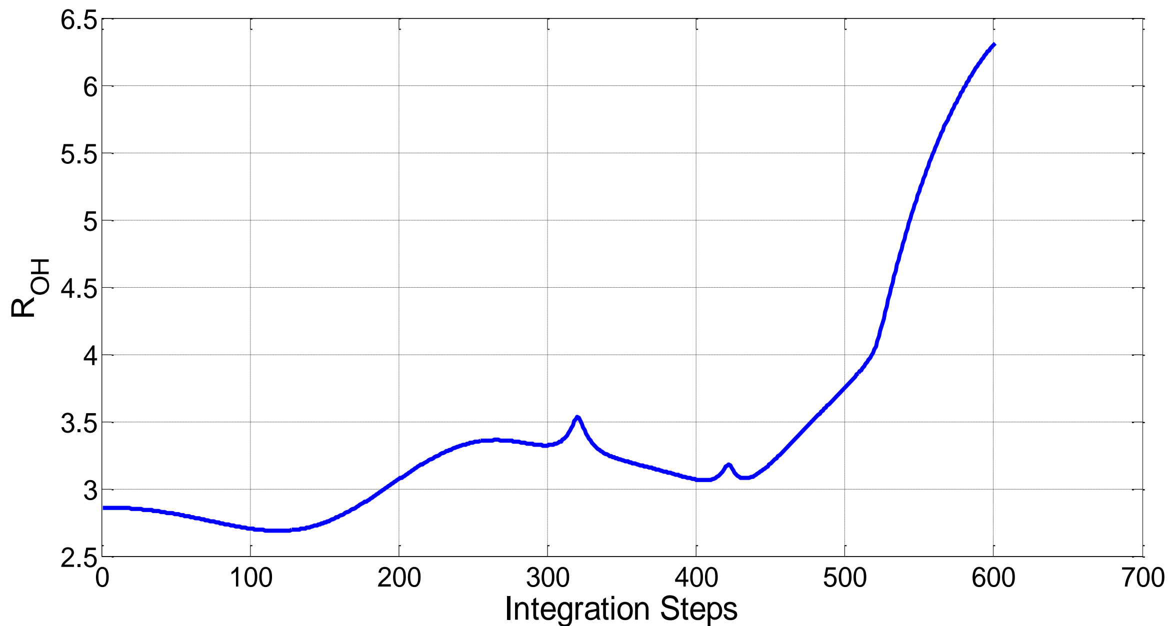

Figure 4.15: Forward integrated trajectory of O—H_1

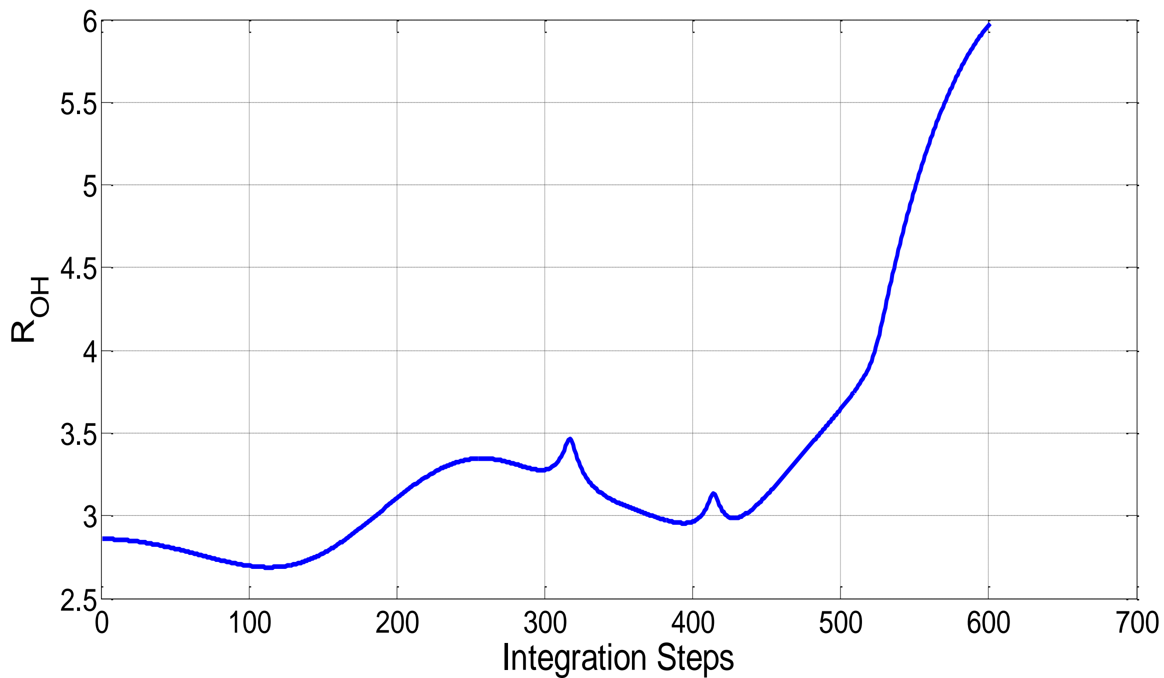

Figure 4.16: Backward integrated trajectory of O—H_1

Even in this case, we can observe from Figure 4.15 and Figure 4.16 that the trajectories perfectly overlap. Clearly, the integrator is sufficiently accurate.

4.8 Energy assignment based on vibration modes of water molecule

With three atoms in a nonlinear arrangement, H_2O has three vibrational modes, according to the formula $3N - 6$ $(i.e., 3(3) - 6 = 3)$. Their measured frequencies expressed in wave numbers are $\mathbf{3825.3}\ \boldsymbol{cm^{-1}}$ in the symmetric stretching mode ν_S (as shown in Figure 4.17), $\mathbf{1653.9}\ \boldsymbol{cm^{-1}}$ in the bending mode ν_B (as shown in Figure 4.18) and $\mathbf{3935.6}\ \boldsymbol{cm^{-1}}$ in the asymmetric stretching mode ν_A (as shown in Figure 4.19)

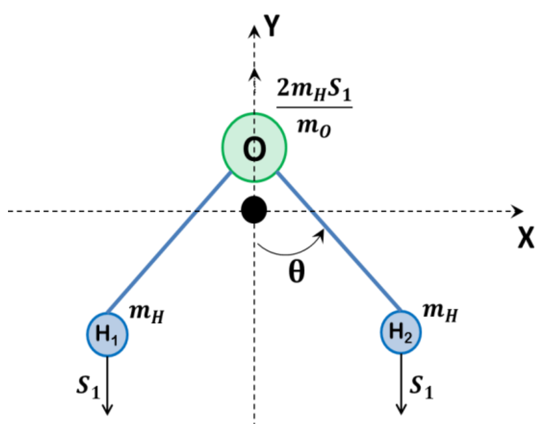

Figure 4.17: Symmetric Stretching mode

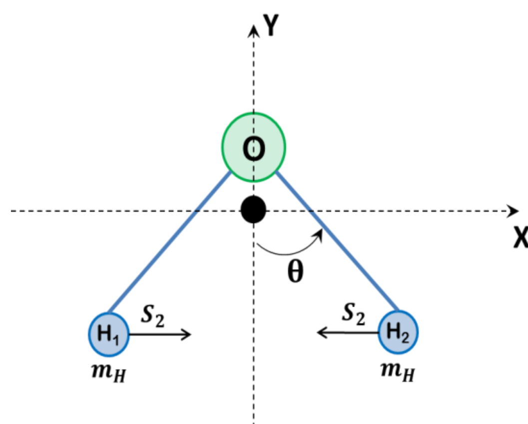

Figure 4.18: Bending mode

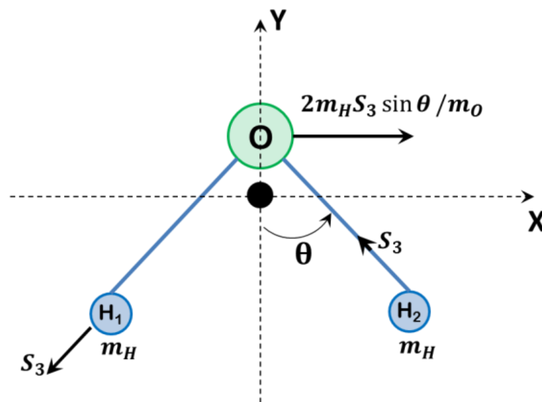

Figure 4.19: Asymmetric Stretching mode

The frequencies are converted into zero-point energy (E) values in hartree using the following conversion factor,

$$E = (\omega)\left[\frac{1 \text{ Hartree}}{2.19475 \times 10^5}\right]\left(\frac{1}{2}\right),$$

where ω is the wave number in cm^{-1}.

The zero-point energy values in hartree are shown below:

$$E(\nu_S) = 0.0087147 \text{ hartree}$$

$$E(\nu_B) = 0.0037679 \text{ hartree}$$

$$E(\nu_A) = 0.0089659 \text{ hartree}$$

The zero-point energies in the equilibrium configuration will all be in the form of kinetic energy of H_2O molecule. Hence the total zero-point energy value will be equal to the total kinetic energy when H_2O is in its equilibrium configuration.

In the symmetric stretching mode (shown in Figure 4.17), the hydrogen atoms are each displaced in the negative Y direction by an amount S_1, which, for moment we will assume is our normal mode vibrational coordinate. To maintain the center of mass fixed, the oxygen atom must be displaced upward by an amount Δy_o during this phase of the vibrational motion. The requirement that the center of mass remain fixed means we must have

$$-m_H S_1 - m_H S_1 + m_O \, \Delta y_o = 0$$

This gives an oxygen atom displacement in Symmetric mode.

$$\Delta y_o = \frac{2 m_H}{m_O} \, S_1$$

All other displacements are zero in this mode. These displacements are symmetric with respect to a 180^0 rotation about the Y-axis in that such a rotation does not change the magnitude of signs of the displacements. This makes it clear that this type of displacement symmetrically stretches the O-H bonds. Consequently, S_1 is termed as symmetric stretching coordinate.

In the bending mode (shown in Figure 4.18), the oxygen atom remains stationary while the hydrogen atoms H_1 and H_2 are displaced along the X-axis by amount $\Delta x_2 = -S_2$ and $\Delta x_3 = S_2$. All other displacements in this mode are zero. A 180^0 rotation about

the symmetric (Y-axis) produces no change in the displacements. Consequently, this mode is also symmetric. The predominate action of the vibrational coordinate is to bend the molecule. S_2 is, therefore, called a bending coordinate.

In the asymmetric bending mode (shown in Figure 4.19), the displacements are

$\Delta x_2 = -S_3 \sin\theta$ and $\Delta y_2 = S_3 \cos\theta$, $\Delta x_3 = -S_3 \sin\theta$ and $\Delta y_3 = -S_3 \cos\theta$.

To maintain the center of mass fixed, we must have

$$m_H \Delta x_2 + m_H \Delta x_3 + m_O\, \Delta x_o = -2S_3 m_H \sin\theta + m_O\, \Delta x_o = 0$$

Therefore, the oxygen-atom displacement must be $\Delta x_o = \frac{2m_H}{m_O} S_3 \sin\theta$. All other displacements are zero. If we rotate the molecule by 180^0 about the Y-axis, all the displacements change directions. Therefore, this vibrational coordinate is asymmetric. It also either stretches or compresses the O−H bonds. We can, therefore, reasonably refer to S_3 as an asymmetric coordinate.

In our case, the three vibrational coordinates are independent and each exhibits harmonic motion, we can set the vibrational coordinates such that the potential and kinetic energies can be written in the form

$$\text{Potential energy, } V(S_1, S_2, S_3) = \sum_{i=1}^{3} a_i Q_i^2 \tag{4.21}$$

$$\text{Kinetic energy, } T = \sum_{i=3}^{3} b_i v_i^2 \tag{4.22}$$

$where\ v_i = \frac{\partial Q_i}{\partial t}$ and the a_i and b_i are constants. The vibrational coordinates S_1, S_2 and S_3 are called “normal mode coordinates” and the three vibrational modes are called “normal modes”.

In order to make sure that their motion will be harmonic, the three vibrational coordinate S_1, S_2 and S_3, must satisfy Equations 4.21, 4.22. The total displacement for all atoms may be obtained by summing the displacement for the three modes.

The result is

$$\Delta x_o = \frac{2m_H}{m_O} S_3 \sin\theta,\ \Delta y_o = \frac{2m_H}{m_O} S_1,\ \Delta z_o = 0 \tag{4.23 a}$$

$$\Delta x_{H_1} = -S_2 - S_3 \sin\theta,\ \Delta y_{H_1} = -S_2 + S_3 \cos\theta,\ \Delta z_{H_1} = 0 \tag{4.23 b}$$

$$\Delta x_{H_2} = S_2 - S_3 \sin\theta,\ \Delta y_{H_2} = -S_1 + S_3 \cos\theta,\ \Delta z_{H_2} = 0 \tag{4.23 c}$$

In Cartesian coordinates, the kinetic energy is given by Eq. 4.24.

$$T = \sum_{i=3}^{3} 0.5m_i \left[\left(\frac{\partial \Delta x_i}{\partial t}\right)^2 + \left(\frac{\partial \Delta y_i}{\partial t}\right)^2 + \left(\frac{\partial \Delta z_i}{\partial t}\right)^2\right] \tag{4.24}$$

If we take the time derivatives of Equations 4.23 a, b and c, making sure that θ is fixed at the equilibrium angle for H_2O, square each result and the sum of derivatives for the three atoms multiplied by the appropriate mass factors, the result is

$$T = \left[m_H + \frac{2{m_H}^2}{m_O}\right]\left(\frac{\partial S_1}{\partial t}\right)^2 + m_H\left(\frac{\partial S_2}{\partial t}\right)^2 + \left[m_H + \frac{2{m_H}^2 \sin\theta}{m_O}\right]\left(\frac{\partial S_3}{\partial t}\right)^2 = \left[m_H + \frac{2{m_H}^2}{m_O}\right] v_{S_1}^2 + m_H v_{S_2}^2 + \left[m_H + \frac{2{m_H}^2 \sin\theta}{m_O}\right] v_{S_3}^2 \tag{4.25}$$

When calculated, both LHS and RHS of Eq.4.25 were equal to 0.0214 Hartree, verifying that the normal mode coordinates were accurate and the H_2O exhibits harmonic motion.

Figure 4.20 (a) shows the vibration of an O−H bond containing all 3 vibrational modes. Figure 4.20 (b) shows the FFT plot of the time series plot shown in Figure 4.20 (a). It can be clearly observed that the vibration has three prominent frequencies which correspond to the 3 modes of normal modes of vibration.

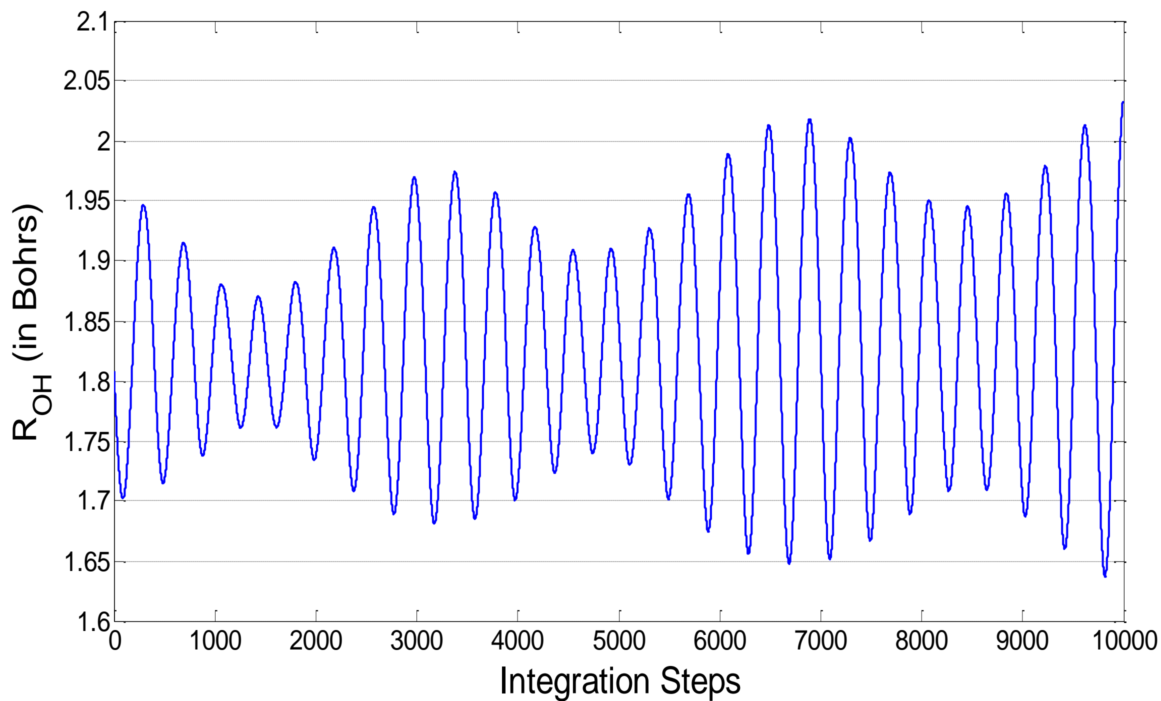

Figure 4.20 (a): Vibration of the O-H bond about the Equilibrium distance (1.8085 Bohrs)

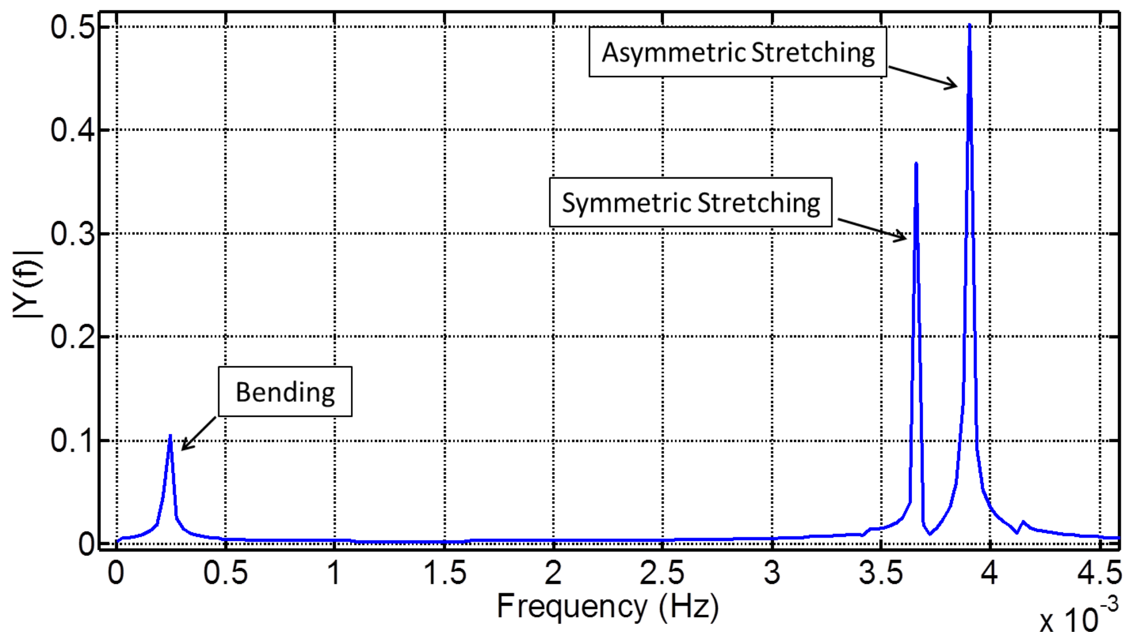

Figure 4.20 (b): FFT of vibration of the O—H bond

4.9 Octahedral structural arrangement of $[Cu\ (H_2O)_6]^{2+}$ complex molecule

Before determining the coordinates of all 6 water molecules, the center of mass is determined using the formulation depicted in Eq. 4.8

$$m_O X - 2m_H \left\{ \cos\left(\frac{\theta}{2}\right) R_{O-H} - X \right\} = 0 \tag{4.26}$$

where, m_O = mass of oxygen atom = 29165.7836 amu

m_H = mass of hydrogen atom = 1837.4041 amu.

θ = bond angle of water H − O − H = 104.5^0 = 1.8239 radians

X = Center of mass in bohrs

R_{O-H} = Euilibrium distance between O − H in H_2O molecule = 1.8085 Bohr

From Eq. 4.26 the center of mass of water is at 0.1239 bohrs. Hence, for all normal mode energy calculations, the oxygen atom is placed at distance of 0.1239 bohrs above Cu^{2+} assuming that Cu^{2+} is exactly located at the center of mass position. Now the system containing just one molecule of water i.e., $[Cu(H_2O)]^{2+}$ assigned with the energies calculated from normal mode coordinates is integrated until several thousand structures and their conjugate momenta values are obtained and saved.

The position of all O atoms about Cu^{2+} i.e., $R_{Cu\text{-}O}$ is then determined based on the density of H_2O model as 5.506 bohrs. In order to introduce a minimal randomness in $R_{Cu\text{-}O}$, Eq. 4.27 was used.

$$R_{Cu-O} = 5.506 \pm 0.02(5.506)\xi \qquad (4.27)$$

where, ξ is a random number such that $-1 \leq \xi \leq +1$

The coordinates of Cu^{2+} were fixed at [0 0 0]. Six random coordinates and their conjugate momenta values are chosen from the previously saved structures. The Z coordinates of the O, H_1 and H_2 atoms of the first water molecule are fixed as $5.506 \pm 0.02(5.506)\xi$, and X coordinates are made 0 as the molecule is placed in the Z-Y plane. Now the second structure is taken and rotated 180^0 about the Y axis using the Rotation matrix R_Y. Its conjugate momenta values are also rotated 180^0 about the Y axis. The Z coordinates of the atoms in the second water molecule are added with a factor of $5.506 \pm 0.02(5.506)\xi$. The third structure is chosen, and is rotated 90^0 about the Y axis using the rotation matrix R_Y and again rotated 45^0 about the Z axis using the rotation

matrix R_Z. Now the third water molecule is moved towards its final position by adding the X and Y coordinates with a factor of $\cos 45° \, [5.506 \pm 0.02(5.506)\xi]$. Its conjugate momenta values are subjected to the same treatment as the coordinates. Same procedure is adopted for fixing the fourth, fifth and sixth water molecules, but in the final step the coordinates are fixed by the following method,

For the fourth water molecule,

$$(Q_X) = (Q_X) - \cos 45° \, [5.506 \pm 0.02(5.506)\xi].$$

$$(Q_Y) = (Q_Y) - \cos 45° \, [5.506 \pm 0.02(5.506)\xi].$$

For the fifth water molecule,

$$(Q_X) = (Q_X) - \cos 45° \, [5.506 \pm 0.02(5.506)\xi].$$

$$(Q_Y) = (Q_X) + \cos 45° \, [5.506 \pm 0.02(5.506)\xi].$$

For the sixth water molecule,

$$(Q_X) = (Q_X) + \cos 45° \, [5.506 \pm 0.02(5.506)\xi].$$

$$(Q_Y) = (Q_X) - \cos 45° \, [5.506 \pm 0.02(5.506)\xi].$$

where, (Q_X) and (Q_Y) represents all the X and Y coordinates of O, H_1 and H_2 of fourth, fifth and sixth water molecule.

All the momenta values are subjected to the same treatment as their corresponding coordinates. The final octahedral arrangement of the copper (II) hexa-hydrate complex molecule is shown in Figure 4.21.

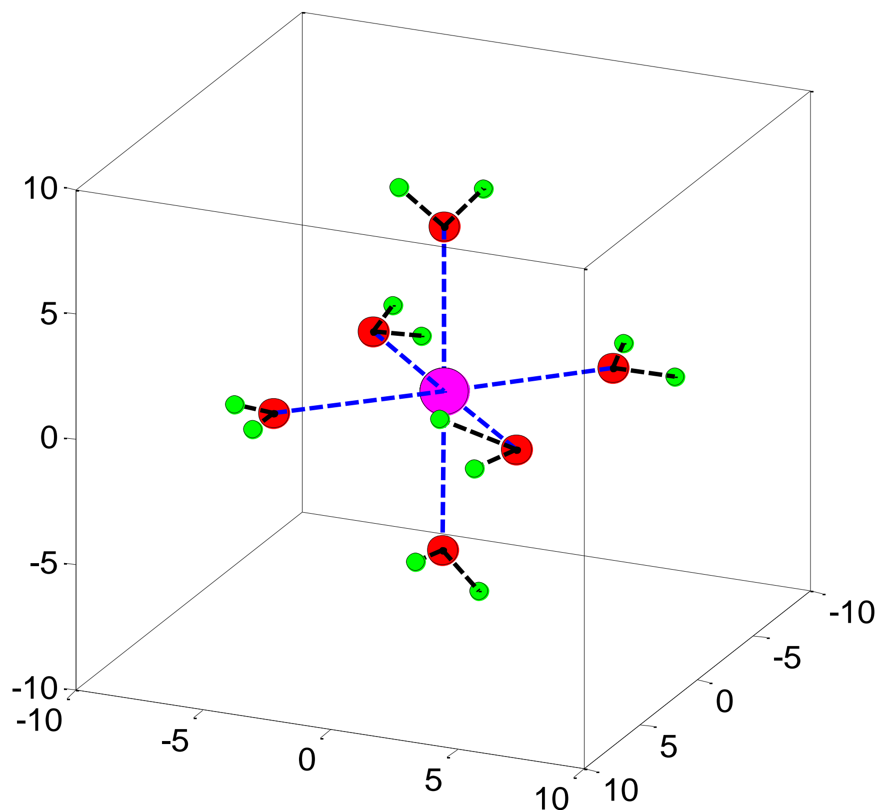

Figure 4.21: Octahedral structure of copper (II) hexa hydrate complex molecule

4.9.1 Damped Trajectory Calculation

After setting up the octahedral structure of the copper (II) hexa hydrate molecule, the average distance between $Cu^{2+}-O$ at the global minima position had to be determined. We know that nature will always place the molecules in the lowest energy position. So by performing damped trajectory calculation, we can determine the average distance between Cu^{2+} and O, which would depict the approximate positions of the atoms, at lowest energy possible.

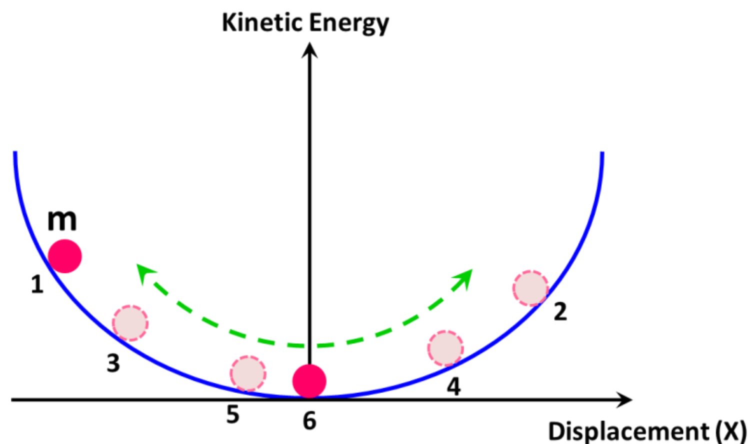

Figure 4.22: Marbel-Bowl experiment

In order to elucidate the concept of damped trajectory, consider an open bowl into which a marble 'm' is rolled, as shown in Figure 4.22. When m is in its initial position 1, it stores potential energy (PE), which eventually gets converted into kinetic energy (KE) until it reaches position 2. The marble loses its kinetic energy because of friction the exerted by the marble, in other words the momenta value becomes 0 at position 2. Again the marble rolls from position 2 to 3, loses some KE due to friction and rolls to position 3 where the momenta again become 0. This rolling action happens until the marble has reached the lowest energy position. Law of conservation of energy is the key principle behind this experiment.

To determine the average distance of Cu^{2+}−O a similar concept was formulated. The $[Cu\ (H_2O)_6]^{2+}$ system was set up in its initial conditions and was integrated through a particular time interval and the kinetic energy was monitored. Initially, the kinetic

energy was increasing (PE was getting converted into KE) and the simulation was stopped at the point where the KE started to decrease. The momenta values at this position were zeroed out and again the system was integrated through some time interval until the KE started decreasing again. This procedure was repeated until the KE value converged and remained constant. The position at this point was stored and from this set of coordinates all the $Cu^{2+}-O$ distances were calculated, in toto 6 distances corresponding to 6 O atoms in the system. The average $Cu^{2+}-O$ was calculated out to be 6.5484 Bohrs, which was updated in the coordinates assigning code and the new initial coordinates of the atoms were defined.

4.10 Water-water interaction potential

Having modeled octahedral arrangement of the complex molecule, next, the water-water interaction potentials were added based on the Coulombic forces of interaction between the pairwise partial charges.

4.10.1 O−O interactions (V_{O-O})

The total number of O−O interactions is given by $\frac{N(N-1)}{2}$. There are totally 6 water molecules hence there would be '15 O−O interactions', which are modeled using Eq. 4.28. q_O is the atomic charge on oxygen atoms = -0.6836. $\boldsymbol{\varepsilon}$ is the dielectric constant of water = 80 at 298K

$$V_{O-O} = \text{Sum of all O} - \text{O repulsion} = \frac{{q_O}^2}{\varepsilon} \sum_{i=1}^{N-1} \sum_{j>i}^{N} (r_{ij})^{-1} \quad (4.28)$$

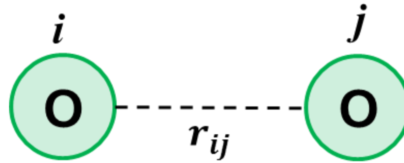

Figure 4.23: O − O interaction (repulsion)

4.10.2 O−H interactions (V_{O-H})

The total number of O−H interactions is given by 2N(N − 1). There are totally 6 water molecules hence there would be '60 O−H interactions', which are modeled using Eq. 4.29. q_O is the atomic charge on oxygen atoms = -0.6836 and q_H is the atomic charge on hydrogen atoms = 0.3418. ε is the dielectric constant of water = 80 at 298K

$$V_{O-H} = \text{Sum of all O} - \text{H interactions} = \frac{q_O q_H}{\varepsilon} \sum_{i=1}^{N-1} \sum_{j>i}^{N} \left[\frac{1}{r_{ij1}} + \frac{1}{r_{ij2}}\right] \quad (4.29)$$

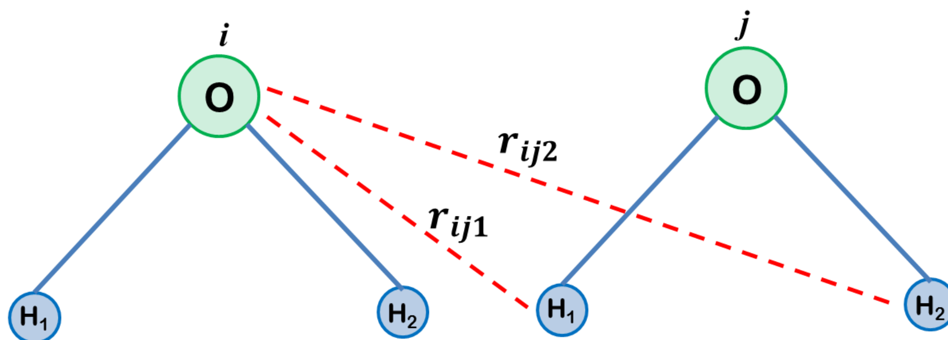

Figure 4.24: O−H interaction

4.10.1 H−H interactions (V_{H-H})

The total number of H−H interactions is given by $\frac{4N(N-1)}{2}$. There are totally 6 water molecules hence there would be '60 H−H interactions', which are modeled using Eq. 4.30. q_H is the atomic charge on hydrogen atoms = 0.3418. $\boldsymbol{\varepsilon}$ is the dielectric constant of water = 80 at 298K.

V_{H-H} = Sum of all H − H interactions

$$= \frac{{q_H}^2}{\varepsilon} \sum_{i=1}^{N-1} \sum_{j>i}^{N} \left[\frac{1}{r_{i_1 j_1}} + \frac{1}{r_{i_1 j_2}} + \frac{1}{r_{i_2 j_1}} + \frac{1}{r_{i_2 j_2}} \right] \tag{4.30}$$

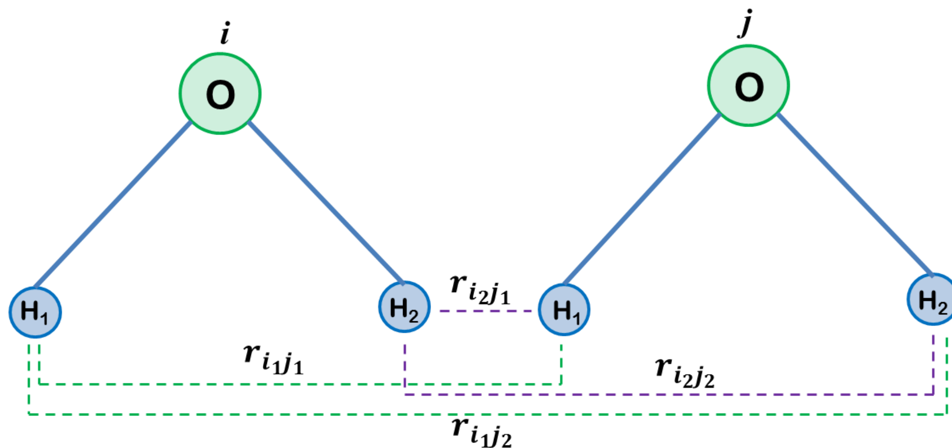

Figure 4.25: H − H interaction

Hence there are a total of '135 terms' in the inter water-water potential. The new V_{TOT} potential would have extra 135 terms in addition to the 18 intra water molecular

interactions, which have been already modeled. So totally there 153 terms in the model corresponding to 6 water molecules. Eq. 4.31 depicts the final V_{TOT} potential for N water molecules.

$$V_{TOT} = \sum_{i=1}^{N}(V_2) + \sum_{i=1}^{2N}\left(V_{H_2O}\right) + \sum_{i=1}^{2N+3} V_{O-O} + \sum_{i=1}^{10N} V_{O-H} + \sum_{i=1}^{10N} V_{H-H} \tag{4.31}$$

After adding the inter water potentials, the model was integrated over time to check whether the law of conservation of energy still holds well. It was observed that the energy was conserved with an accuracy of 9-10 digits, as shown in Figure 4.26.

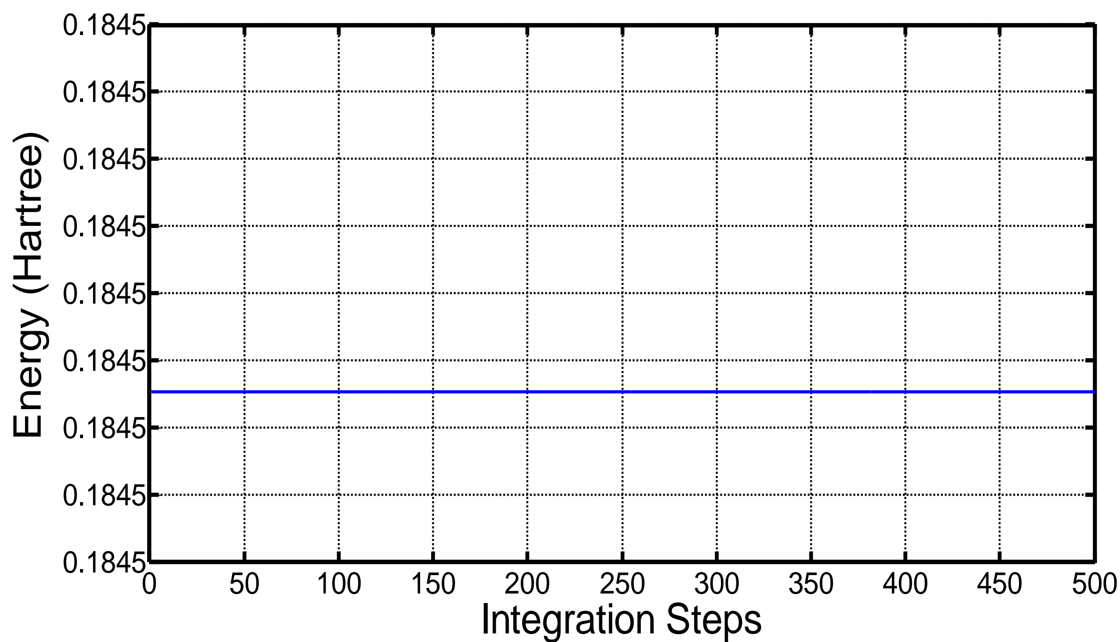

Figure 4.26: Total Energy conservation of the octahedral $[Cu(H_2O)_6]^{2+}$ system

4.11 Simulation of $[Cu(H_2O)_6]^{2+}$ molecule under electrode potential

In ECMP process, the Cu^{2+} ion gets liberated from the anode due to oxidation and travels towards cathode where hydrogen reduction happens. In order to observe the behavior of $[Cu(H_2O)_6]^{2+}$ complex molecule under electrode potential, the molecule is subjected to an external electric field. The electric field is assumed to be uniform in this case.

Figure 4.27 provides a pictorial representation of the application of uniform electric field between positively charged anode and negatively charged cathode. 'V' is the applied anodic potential and R is the distance between anode and cathode in meters.

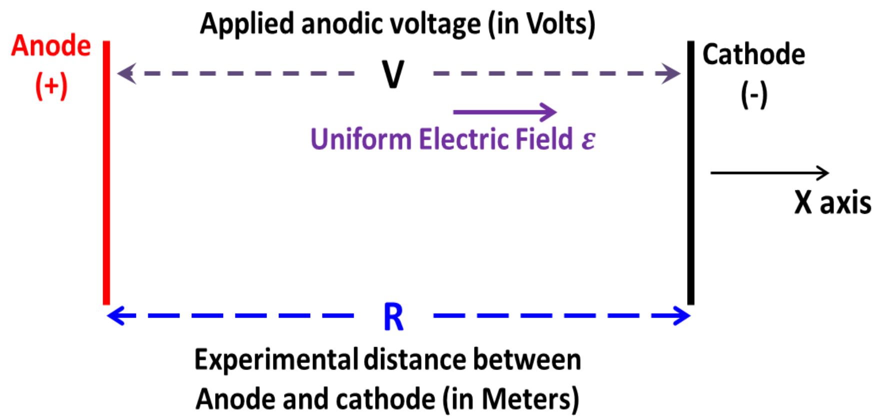

Figure 4.27: Application of external electric field

Uniform electric field (ε) can be calculated using Eq. 4.32.

$$\varepsilon = \frac{V}{R} \ (\text{volts m}^{-1}) \tag{4.32}$$

$$\text{External electric energy, } E_e = Vq \ (\text{in eV}) \tag{4.33}$$

$$= \text{Vq [eV]} \left[\frac{1 \text{ hartree}}{27.2114 \text{ eV}}\right] = \frac{\text{Vq}}{27.2114} \text{ hartree}$$

$$= \frac{\text{Vq}}{27.2114 \text{ R}} \left[\frac{\text{hartree}}{\text{m}}\right]\left[\frac{0.529177 \times 10^{-10}\text{m}}{\text{bohr}}\right]$$

$$E_e = \frac{\text{Vq}}{\text{R}} (1.944689 \times 10^{-12}) \frac{\text{hartree}}{\text{bohr}}$$

Assuming that the conversion factor, $\beta = 1.944689 \times 10^{-12}$, we can calculate the force exerted on the system along X axis due to the external electric field as shown in Eq. 4.34

$$\overrightarrow{\varepsilon_X} = \frac{\beta \text{Vq}}{\text{R}} \tag{4.34}$$

where, $\overrightarrow{\varepsilon_X}$ is the Electric force due to the uniform electric field

$$\beta = 1.944689 \times 10^{-12}$$

V is the applied experimental anodic potential = 4.5 V

q is charge on Copper = +2

R is Experimental distance between anode and cathode = 0.005 m

ε_r is the dielectric constant of water = 80 at 298K

As the external electric field is applied along the X axis, $\overrightarrow{\varepsilon_Y} = \overrightarrow{\varepsilon_Z} = 0$ and $\overrightarrow{F_Y} = \overrightarrow{F_Z} = 0$. V_{TOT} has to be added with $\overrightarrow{\boldsymbol{\varepsilon_X}}$ and

$$F^e_{Xi} = \text{electric force on particle i} = \frac{\beta \text{V} q_i}{\text{R}} = \left(-\frac{\partial V_i}{\partial X_i}\right)$$

Hence,

$$\frac{\partial P_{Xi}}{\partial x} = \left(-\frac{\partial V_{TOT}}{\partial X_i}\right) + F_{Xi}^{e} = \left(-\frac{\partial V_{TOT}}{\partial X_i}\right) + \frac{\beta V q_i}{\varepsilon_r R}$$

In the next section, Section 4.12, results obtained from the MD simulation at different condition has been presented.

4.12 Simulation results and discussions:

The copper (II) hexa hydrate molecule was simulated under 3 different conditions.

1) No voltage condition
2) Experimental voltage condition (4.5 V)
3) High voltage condition (50 V)

Some voltages are too high to be included in the real world ECMP process, but are considered here to investigate the effects of voltage on the shape of the complex molecule and also the movement of Cu^{2+} ion.

In all the results shown below, the following conventions would apply.

Magenta sphere: Cu^{2+} ion

Red spheres: O atoms

Green atoms: H atoms

Blue dotted lines: Cu−O bonds

Black dotted lines: O−H bonds

At the end of every simulation results, the corresponding energy curves have also been reported. All the simulations were run from an initial time, t_0 = 10 to final time, t_{final} = 50000, with a time step of 100.

The view angle of the molecular structure is at an azimuthal angle of 169 and an elevation angle of 9. This configuration was chosen after trying out different viewing angles and only this alignment could show the change of the molecular shape accurately.

4.12.1 No voltage condition:

At no voltage condition there is no external force applied to the system. The atoms are provided with minimal thermal energy at the room temperature (298K). The following snap shots from the MD simulation, shows the step by step change of the isolated complex molecule in aqueous solution with time. Snap shots are taken at time steps of 0, 50, 150, 200, 250, 300, 350, 400, 450 and 500.

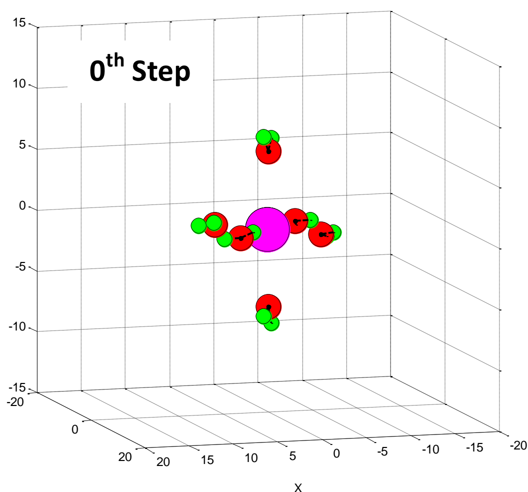

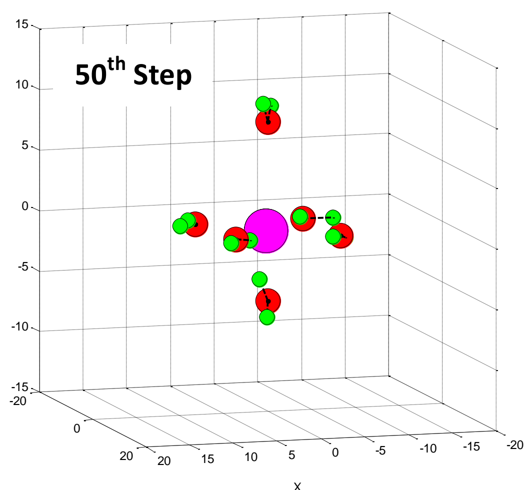

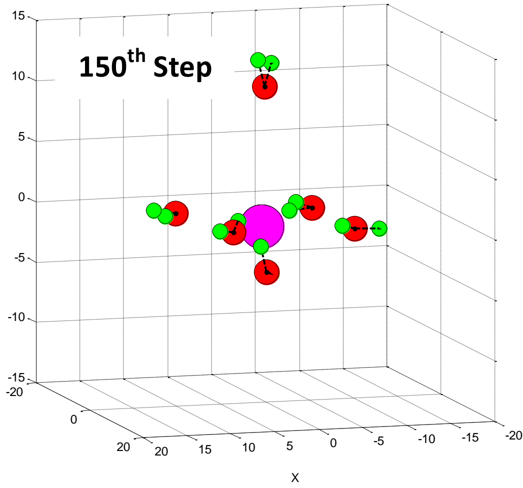
150th Step
x
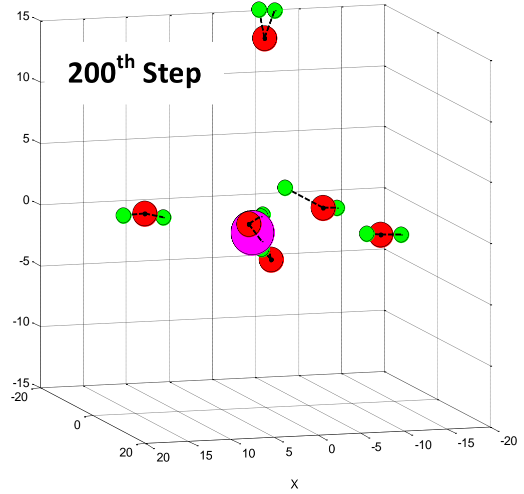
200th Step
x
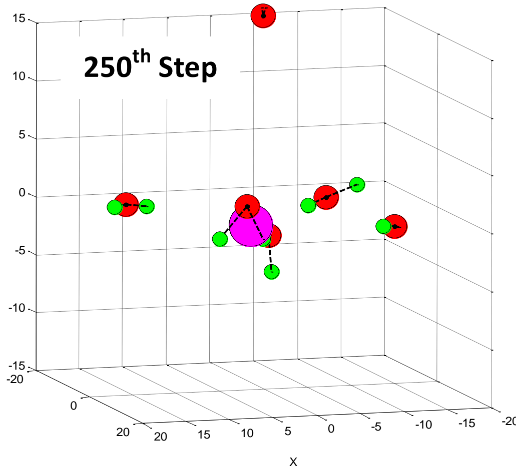
250th Step
x
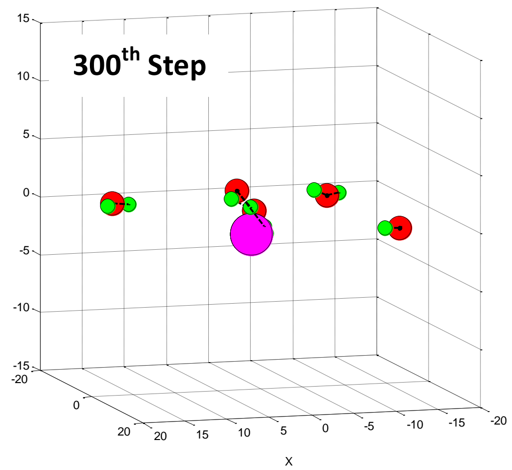
300th Step
x
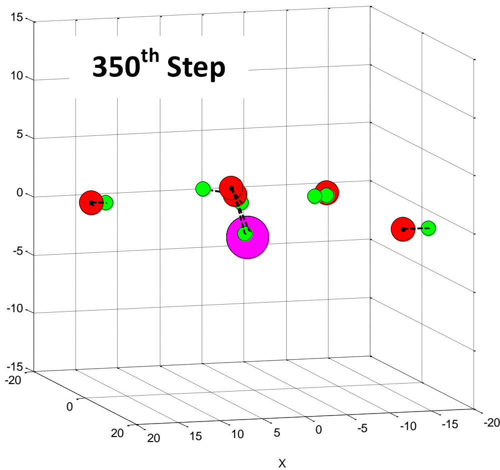
350th Step
x
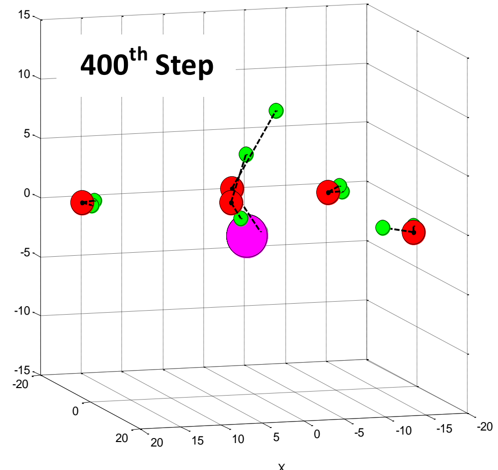
400th Step
x

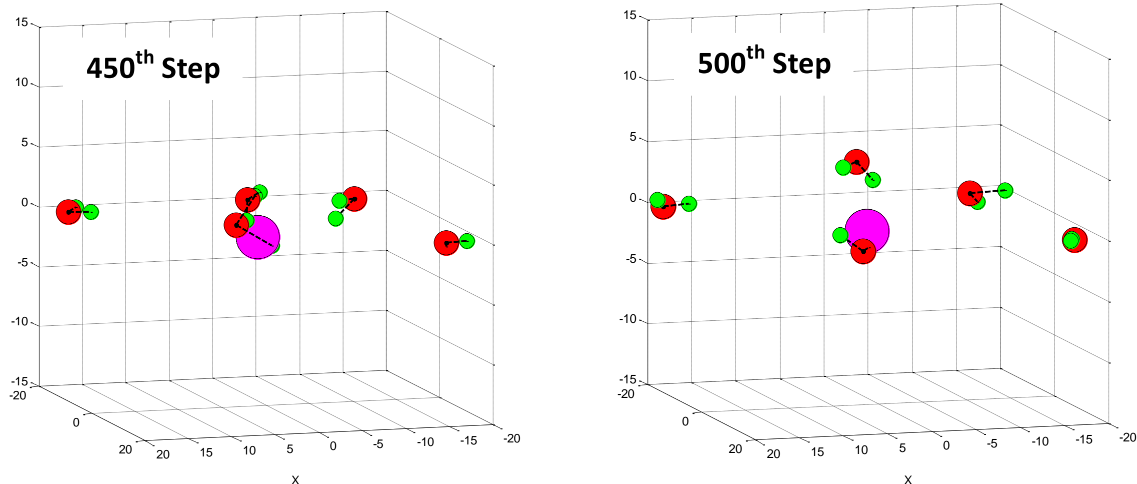

From the above snap shots, we can clearly see that at no voltage condition the atoms reorient themselves at random positions. Though the octahedral shape of the complex molecule is distorted the H atoms stay with the O atoms indicating that the water molecules are stable. But they exhibit three modes of vibration: symmetric stretching, asymmetric stretching and bending, in correspondence to the initial energy we have provided the atoms. As the repulsive force between Cu ion and water molecules increase owing to distance between Cu and H_2O, the water molecules are repelled away from the Cu ion, as they are governed by the V_2 potential, which has a greater well depth.

From Figure 4.28, we can observe the movement of Cu ion in the X and Y directions. Though we have not applied any voltage, we can observe minimal movement of Cu ion. This is caused due to the repulsive and attractive forces exerted on the Cu ion by the water molecules.

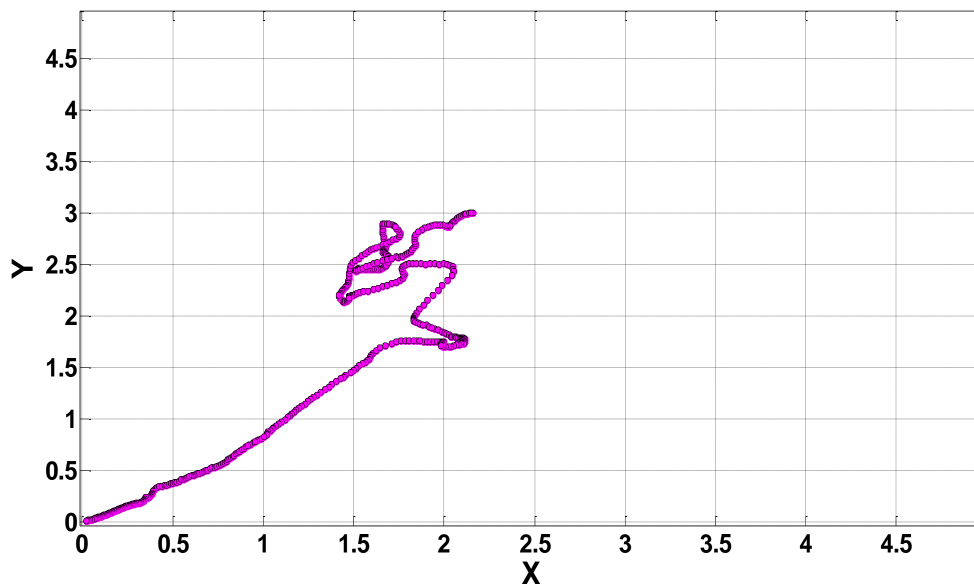

Figure 4.28: Movement of Cu ion at no volt condition

With no external force applied to the system, the energy is perfectly conserved as shown in Figure 4.29

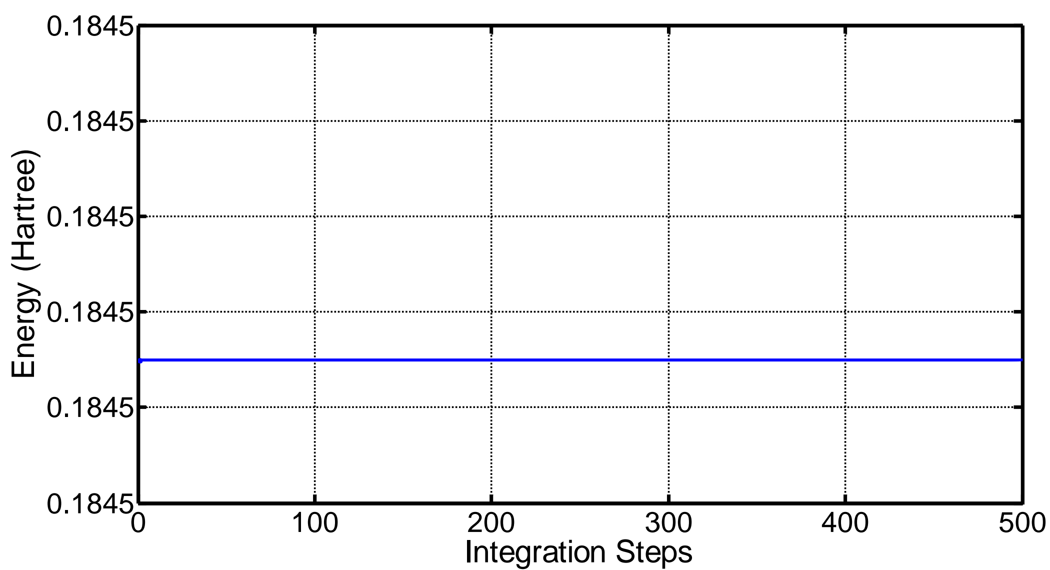

Figure 4.29: Energy plot at no volt condition

4.12.2 Experimental voltage condition

In order to observe the simulation under experimental voltage condition, a potential of 4.5 V was applied along the X direction. Snap shots of the system were taken at the same time steps as recorded in Section 4.12.1.

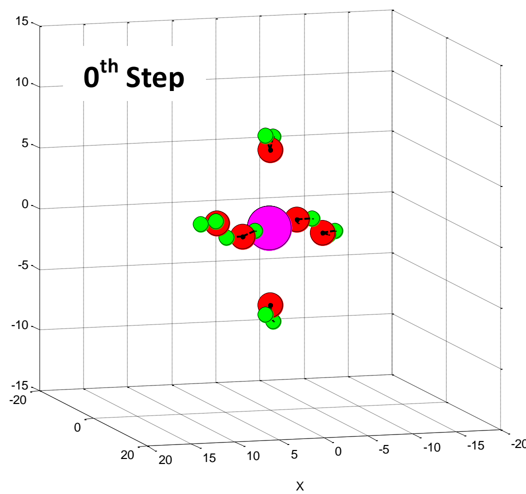

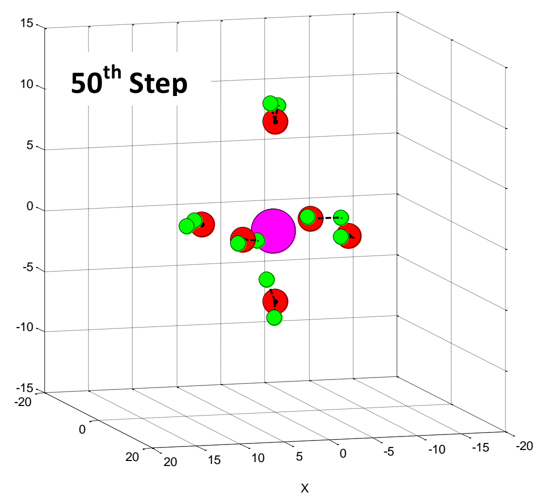

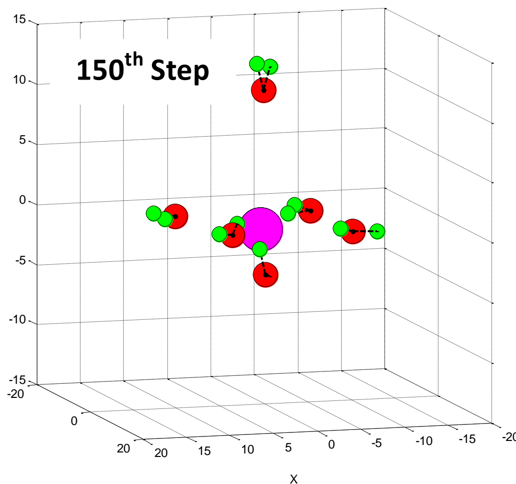

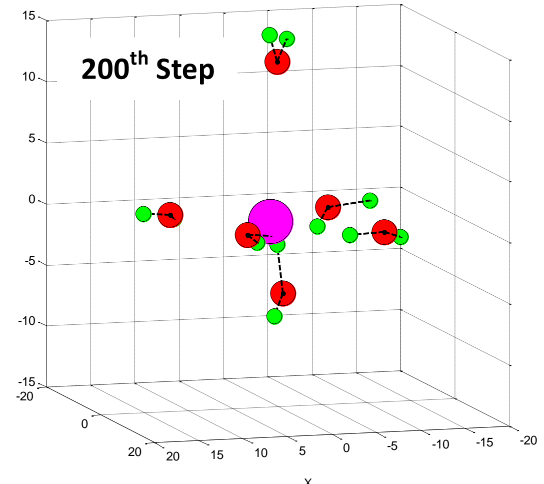

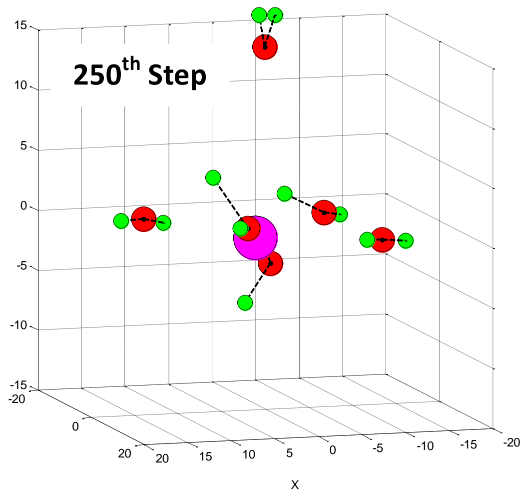
250th Step
15
10
5
0
-5
-10
-15
-20
0
20
20
15
10
5
0
-5
-10
-15
-20
x

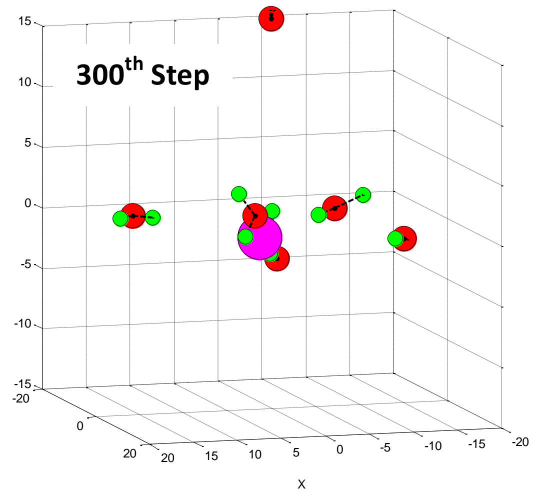
300th Step
15
10
5
0
-5
-10
-15
-20
0
20
20
15
10
5
0
-5
-10
-15
-20
x

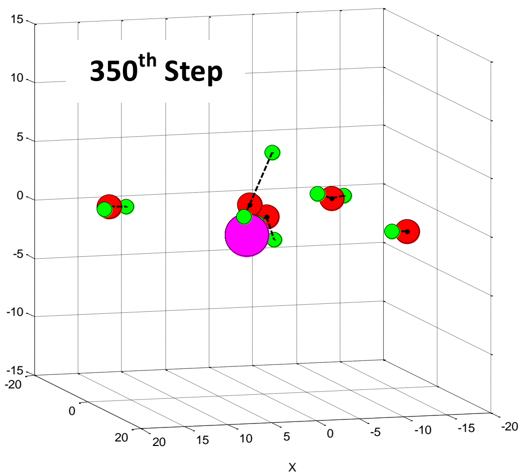
350th Step
15
10
5
0
-5
-10
-15
-20
0
20
20
15
10
5
0
-5
-10
-15
-20
x

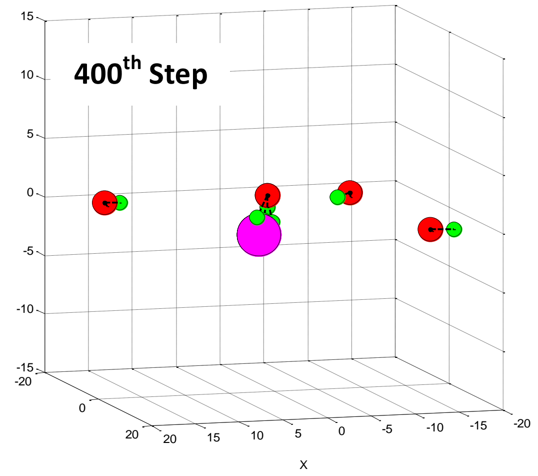
400th Step
15
10
5
0
-5
-10
-15
-20
0
20
20
15
10
5
0
-5
-10
-15
-20
x

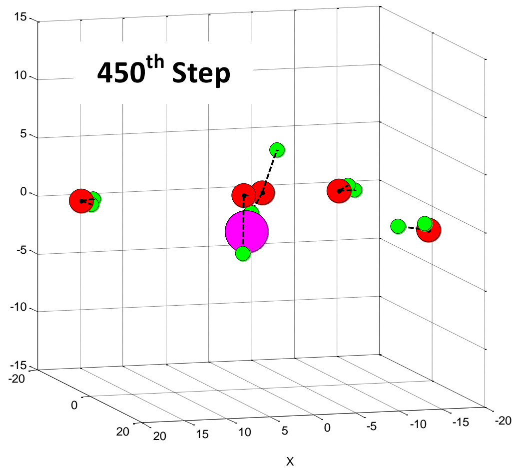
450th Step
15
10
5
0
-5
-10
-15
-20
0
20
20
15
10
5
0
-5
-10
-15
-20
x

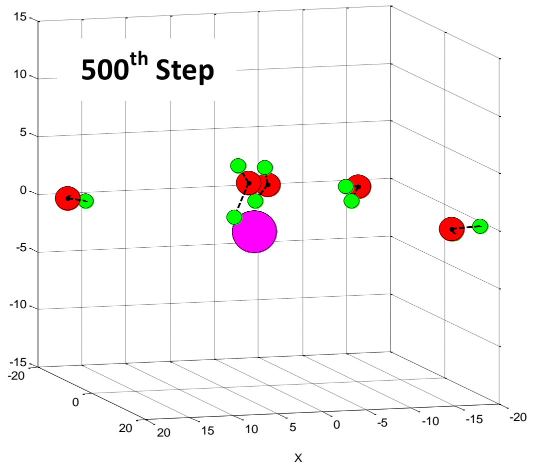
500th Step
15
10
5
0
-5
-10
-15
-20
0
20
20
15
10
5
0
-5
-10
-15
-20
x

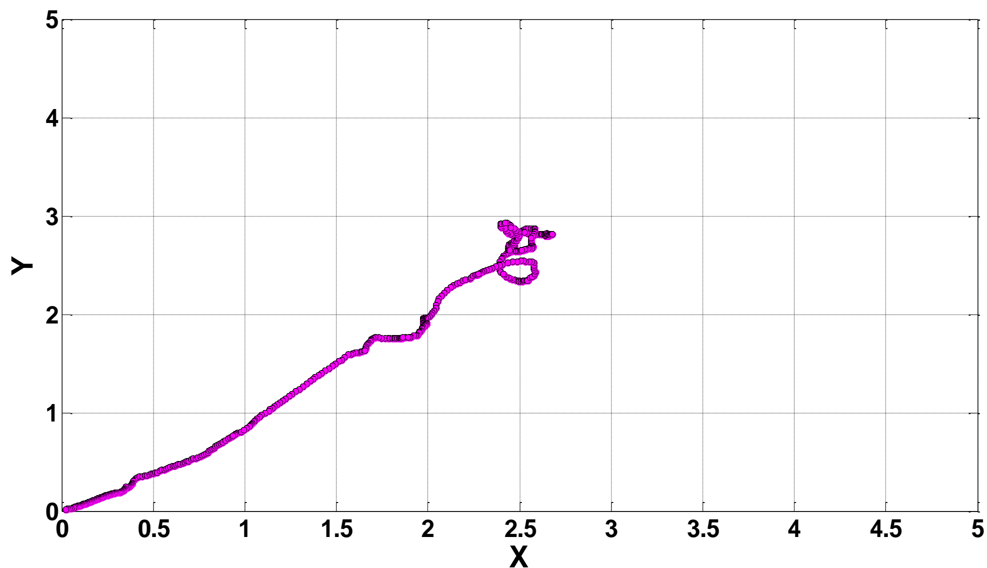

Figure 4.30: Movement of Cu ion at experimental potential condition

In this case, we can observe that the velocity of the Cu ion has increased, due to the applied voltage of 4.5V as observed in Figure 4.30.

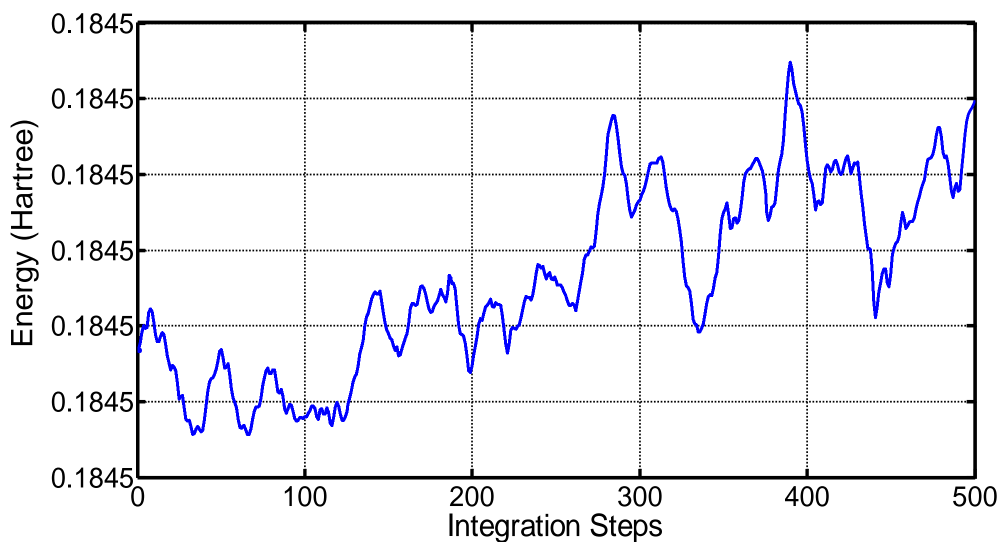

Figure 4.31: Energy plot at experimental potential condition

Figure 4.31 depicts the variation of energy with time. Due to application of the external electric force field the energy is no longer conserved.

4.12.3 High voltage condition

To observe the behavior of the Cu ion at a higher voltage condition, a voltage of 50 V was applied across the system along the X direction.

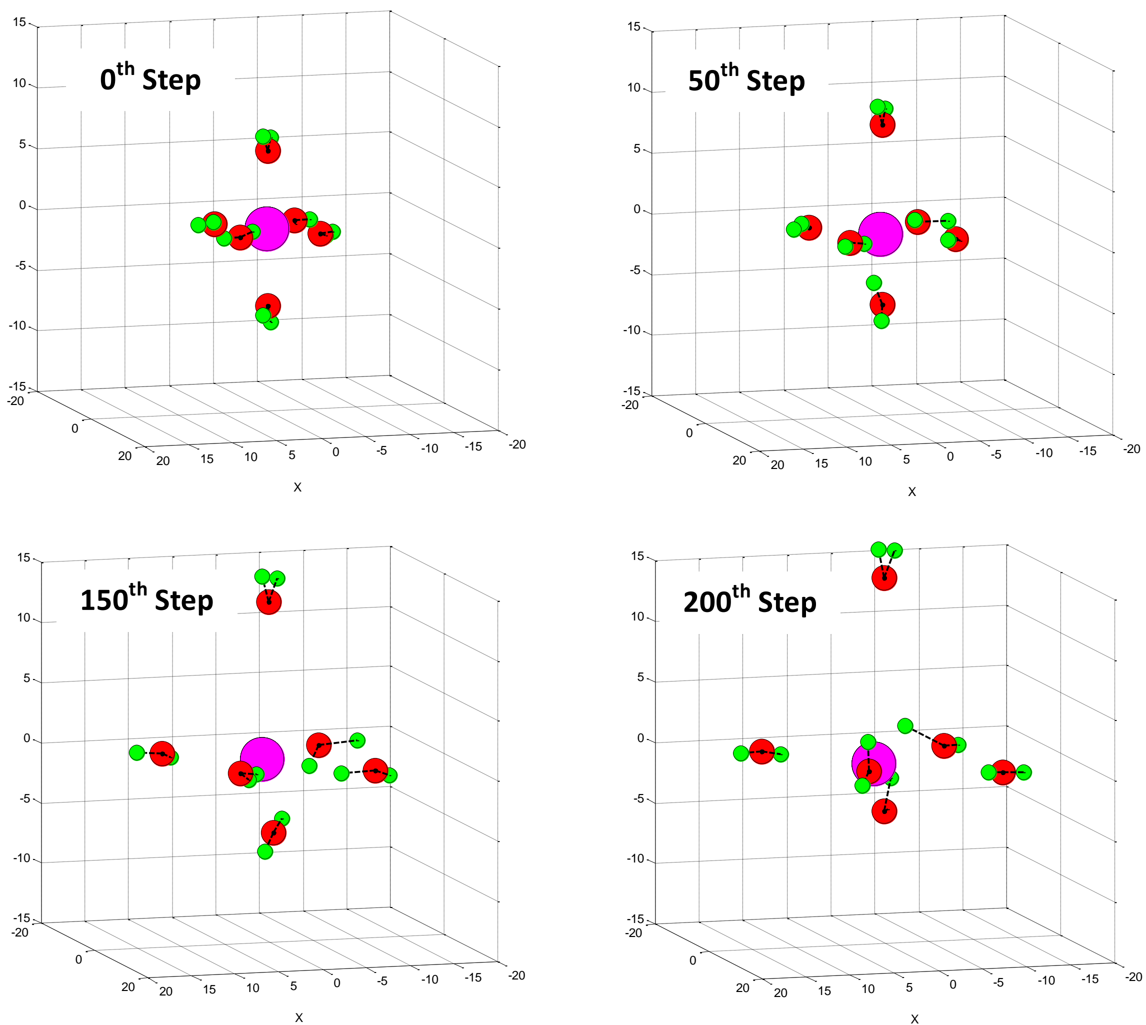

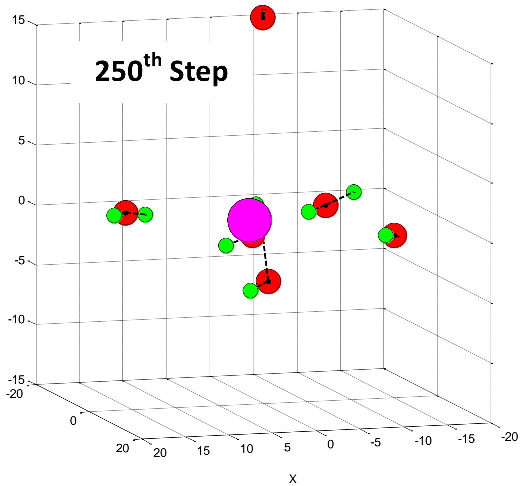
250th Step
x

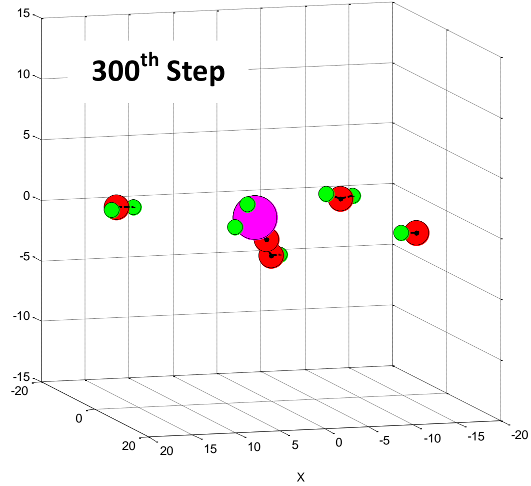
300th Step
x

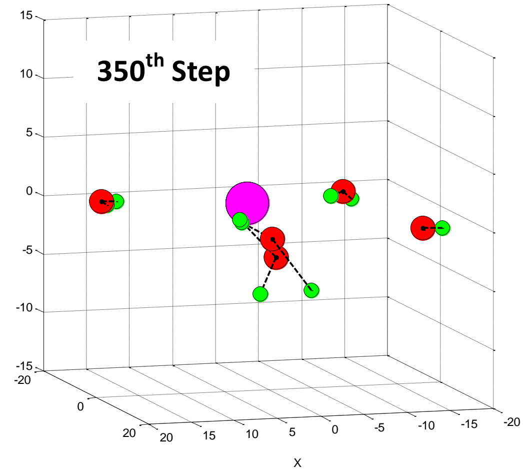
350th Step
x

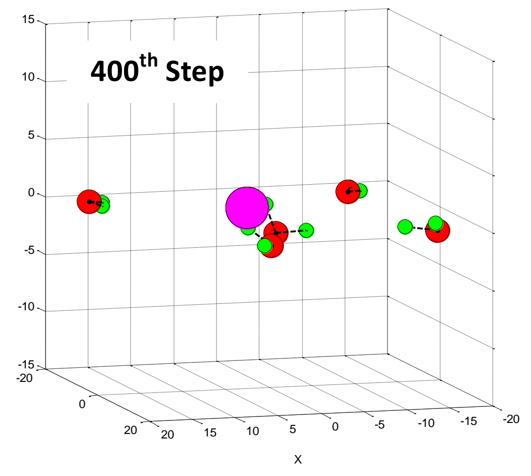
400th Step
x

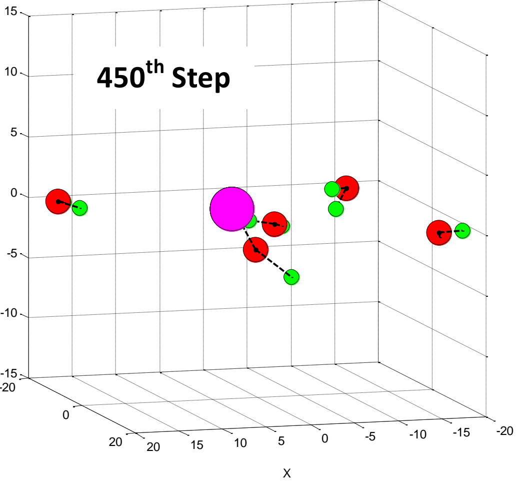
450th Step
x

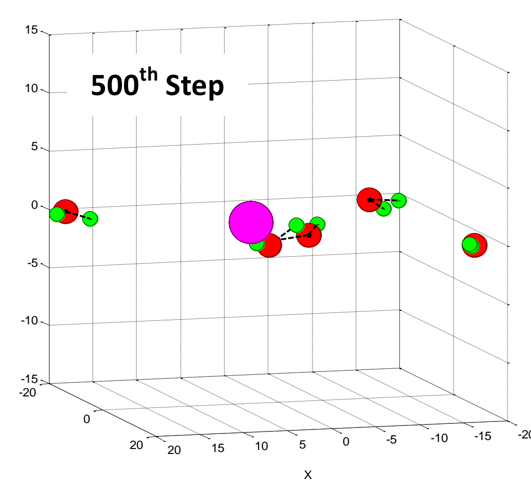
500th Step
x

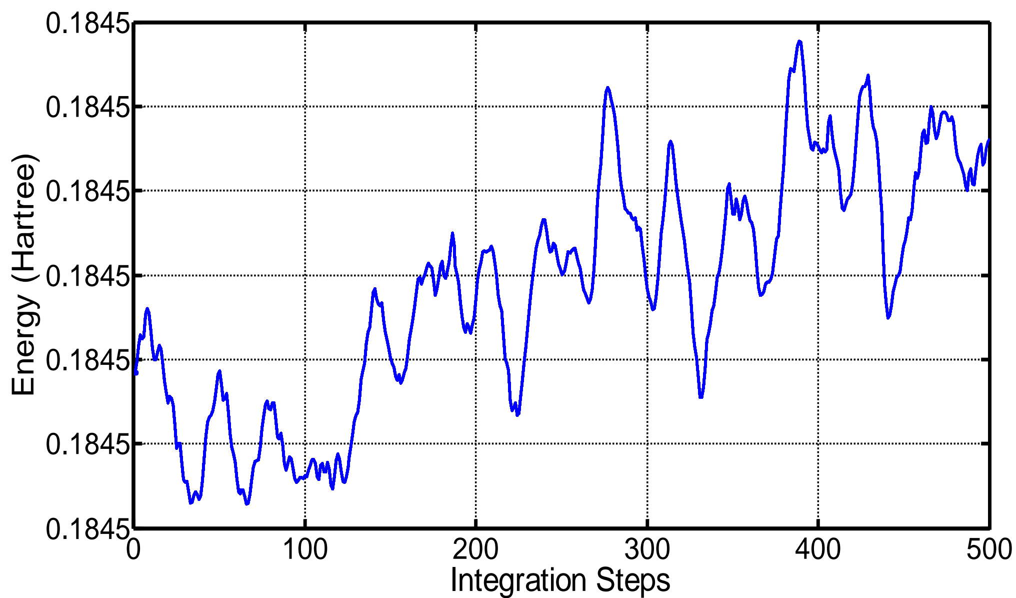

Figure 4.32: Energy plot at higher potential condition

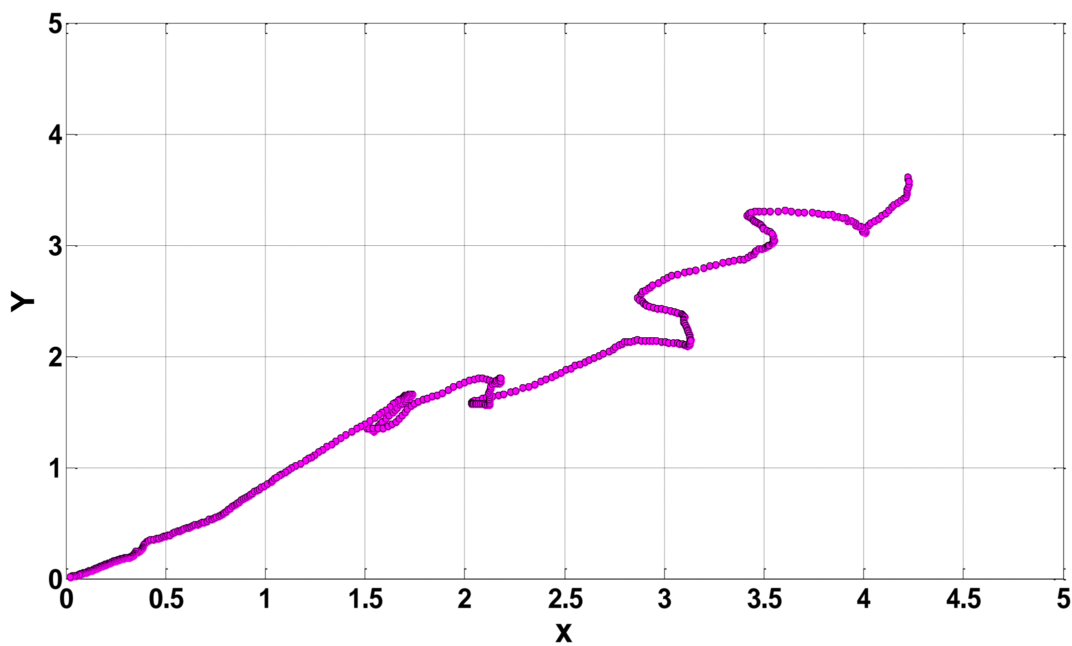

Figure 4.33: Movement of Cu ion at higher potential condition

From the snap shots at different time steps and from Figure 4.33, we can clearly observe that the distance moved by Cu ion with time is more than observed at 0V and 4.5V conditions. This shows that the velocity of the Cu ion has increased and it is mainly because of the increase in applied voltage. There are minimal movements in the Y direction, which is due to the repulsive and attractive forces exerted on it by water molecules. From Figure 4.32, we can see that the energy of the system has increased due to the high voltage applied to the system.

Although by running the simulation for more time, we will be able to track the movement of Cu^{2+} and water molecules in a more precise manner, the relative tolerance value of the numerical integrator was set to a very low value in order to obtain accurate results, hence the simulation would require more computation time and memory to store the results.

4.13 Computation of current carried by Cu^{2+}

The current carried by the cation, in our case Cu^{2+}, can be calculated from the velocity of Cu^{2+} at varied anodic voltage conditions.

$$\text{Time} = (500 \times 100)\ \text{time units} \times 2.41888 \times 10^{-17} = 1.2094 \times 10^{-12}\ \text{s}$$

$$\text{Distance} = \left(\frac{1\ \text{cm}}{10^{8}}\right) \times (\text{d}) \times \left(\frac{0.529\ \text{A}^{\text{o}}}{\text{bohr}}\right)$$

where, d = distance travelled by Cu^{2+} in bohrs

$$\therefore \langle v \rangle = \frac{\text{Distance}}{\text{Time}} \text{ in cm/s}$$

The current carried by a Cu^{2+} (cation),

$$I_+ = \frac{\partial Q_+}{\partial t} = \frac{N_+ z_+ e v_+}{D}$$

where, N_+ = Total number of Cu^{2+} in the system

z_+ = charge carried by Cu^{2+} = +2

e = charge carried by electrons = 1.602177×10^{-19} coloumb

v_+ = terminal velocity of Cu^{2+}

D = Distance between cathode and anode = 0.01 m

The current carried by a single copper ion at experimental and high voltage condition has been presented in Table 4.2

Table 4.2: Current carried by Cu^{2+} at different voltage conditions

Applied voltage (V)	Velocity (m/s)	I_+(amps/ion)
4.5	103.84	3.322×10^{-15}
50	166.53	5.335×10^{-15}

Hence, the total current carried by all the Cu^{2+}ions = $N_+ \times I_+$

where, N_+ = Total number of Cu^{2+} in the system

CHAPTER V

SUMMARY AND FUTURE WORK

In this study, the prime emphasis was on understanding the process mechanism from an experimental and atomistic standpoint. The focus was on understanding and delineating the various electrochemical phases as stated in the literature from the ECMP process and their influence on the process. The ECMP apparatus was redesigned and modified to integrate the setup with a data acquisition (DAQ) system to monitor the current signal and track the transition of electrochemical phases with respect to the process parameters. From the experimental study of Cu ECMP using phosphoric acid based slurry, the following observations are recorded and the mechanism behind it has been elaborately discussed in chapter III.

The next significant aspect of this work is to study and understand the process further from an atomistic standpoint. Using the molecular dynamics (MD) simulation technique, the copper (II) hexa hydrate molecule, one of the chief elements of the passivation layer, was modeled and simulated under different anodic conditions. Changes in the molecular shape with increases in voltage were also observed at different time steps. Without any voltage being applied, the atoms in the molecule reorient themselves

to a minimum energy configuration and energy is also conserved as there is no external force. The molecule began orienting itself, such that the copper ion moved towards the anode along the direction of application of the electric force (X direction), with application of the electric potential. As the voltage increased, the translation distance of Cu ion with time increased indicating that the velocity of the Cu ion has also increased.

Table 5.1: Summary of the experimental results

Process Parameter	**Conditions**	**Conclusions**
pH	Acidic (pH = 2)	• MRR increases with increase in anodic voltage • R_a increases with increase in anodic voltage
	Near Neutral (pH = 6.5)	• MRR increases with increase in anodic voltage but the values are way lower than the values observed at pH = 2. • R_a decreases with increase in anodic voltage
Anodic Voltage	Active	• R_a value is high • MRR value is low
	Passive	• R_a is improved than active region • MRR is slightly increased over the active region
	Transient/ Trans-passive	• Best R_a value and high MRR are achieved • Optimum regions to work with, in Cu ECMP

In the future, with respect to the experimental part, better control of the pad pressure can help in achieving better control over the process. Electrochemical analysis of the slurry can provide more information about the components formed in the slurry

after the ECMP process, which can provide us more insight into the composition of the passivation layer. In terms of atomistic simulation, more water molecules can be added to the system. In addition to observing the complex molecule under different anodic potentials, the effect of variations of the pH on the complex molecule can be studied. In this work, the interaction of Cu ions with water has been studied in detail, but the work can be extended by adding other slurry components to gain a better understanding of the Cu ECMP process. Furthermore, by calculating the number of copper ions in the system we can calculate the fraction of current carried by copper ions. With addition of H^+ and PO_4^{3-} ions to the system we can also compute the fraction of current carried by the corresponding ions. The total current I_{total} can then be calculated as,

$$I_{total} = i_{Cu^{2+}} + i_{H^+} + i_{{PO_4}^{3-}}$$

where, $i_{Cu^{2+}}$ = Current carried by Cu^{2+}

i_{H^+} = Current carried by H^+

$i_{{PO_4}^{3-}}$ = Current carried by ${PO_4}^{3-}$

If we can create a model which can express material removal rate as a function of I_{total}, we can very well predict MRR of ECMP process. To compute the transference numbers of H^+ and ${PO_4}^{3-}$ more experimental and computational works have to be carried out. By this way we can to make this molecular dynamic simulation model work from an engineering standpoint, to predict MRR.

REFERENCES

[1] J. Givens, S.G., O. Cain, W. Clark, C. Koburger, and J. Lee, “A Low-Temperature Local Interconnect Process in a 0.25 μm Channel CMOS Logic Technology with Shallow Trench Isolation”, Proceedings of the 11th International VLSI Multilevel Interconnection Conference1994, p. 43-48.

[2] M.Stravev et al., “Study of Ta (N,O) Diffusion Barrier Stability: Analytical and Electrical Characterization Of Low Level Cu Contamination in Si.”, Microelectronic Engineering, 1997, 37/38, p. 245-251.

[3] J.Baumann et al., “Investigation of Copper Metallization Induced Failure of Diode Structures with and without Barrier Layer”. Microelectronic Engineering, 1997, 33, p. 283-291.

[4] J.M. Steigerwald, S.P.M., R.J. Gutmann, D.J. Duquette, “Chemical processes in the chemical mechanical polishing of copper.”, Materials Chemistry and Physics 1995, 41, p. 217-228.

[5] Nadiia Kulyk et al., “Study on electrochemical mechanical polishing process of copper circuit on PCB” Korean J. Chem. Eng., 2010, 27(1), p. 310-314.

[6] X.G. An, Q.S., “Research on the Combined Electro Chemical Mechanical Polishing,. Electro Machining, 2002, 2

[7] N. Chandrasekaranz, S. Ramarajan, W. Lee, G. M. Sabde andS. Meikle, “Effects of CMP Process Conditions on Defect Generation in Low-k Material: An Atomic Force Microscopy Study”, Journal Of The Electrochemical Society, ISSN 0013-4651, 2004, Volume 151, Issue 12, pp. G882 - G889.

[8] Sato et al., “Newly developed Electro-Chemical Polishing process of Copper as Replaement of CMP suitable for Damascene Copper Inlaid in Fragile Low-k Dielectrics”, Electron Devices Meeting, 2001, IEDM '01. Technical Digest. International Conference, pp. 441- 444, 2001.

[9] Paul R. Bessera and Qing-Ting Jianga, “Mechanical strain evolution in Cu/low-K interconnect lines”, MRS Online Proceedings Library, ISSN 1946-4274, 01/2003, Volume 795.

[10] Yuan-Long Chena, S.-M.Z., Shuo-Jen Lee b, Jong C. Wang b, “The technology combined electrochemical mechanical polishing”, Journal of Materials Processing Technology, 2003, 140, p. 203-205.

[11] S. Jeong, J.B., H. Lee, H. Lee, Y. Lee, B. Park, H. Kim, S. Kim, and H. Jeong, “Effect of mechanical factor in uniformity for electrochemical mechanical planarization”, Sensors and Actuators A, Physical, 2010, 163, p. 433-439.

[12] Chen, C.-C.A. and C.-H. Hsieh, “Effect of Inhibiter Concentration on Cu CMP Slurry Analyzed by a Cu-ECMP System.” ECS Meeting Abstracts, 2010,1002(21), p. 1474-1474.

[13] F. Q. Liu, S.D.T., Y. Hu, and L. Y. Chen, " Method and composition for fine copper slurry for low dishing in ECMP ", 2004, United States.

[14] Seo. S. J, Han. Y. J., "Voltage-induced material removal mechanism of copper for electrochemical-mechanical polishing applications", Transactions of Nonferrous Metals Society of China, 2009. 19, p. 262-265.

[15] Han et al., "Electrochemical–mechanical polishing application: Monitoring of electrochemical copper removal from current–voltage characteristics in HNO_3 electrolyte" , Microelectronic Engineering, 2011. 88, p. 46-52.

[16] D. Padhi, J.Y., S. Gandikota, and G. Dixit, "Planarization of Copper Thin Films by Electropolishing in Phosphoric Acid for ULSI Applications", Journal of The Electrochemical Society, 2003,150(1), p. 10-14.

[17] S. Lee, Y.L., and M. Du, "The polishing mechanism of electrochemical mechanical polishing technology", Journal of Materials Processing Technology, 2003, 140, p. 280-286.

[18] Brown, A.S., "Flat, Cheap, and under control", IEEE Spectrum, 2005. 42: p. 40-45.

[19] Economikos, L et al., "Integrated electro-chemical mechanical planarization (Ecmp) for future generation device technology", in Interconnect Technology Conference, 2004, Proceedings of the IEEE 2004 International. 2004.

[20] R. Fang, D.K., and D. K. Watts, "Recycling of electrochemical-mechanical planarization (ECMP) slurries/electrolytes", 2010, United States.

[21] Goonetilleke P C, R.D., "Electrochemical-mechanical planarization of copper: Effects of chemical additives on voltage controlled removal of surface layers in electrolytes", Materials Chemistry and Physics, 2005, 94, p. 388-400.

[22] Samuel B. Emery, J.L.H., Maria A. Darling, Dipankar Roy, "Chemical factors for chemical–mechanical and electrochemical–mechanical planarization of silver examined using potentiodynamic and impedance measurements", Materials Chemistry and Physics, 2005, 89(2-3), p. 345-353.

[23] Kristin G ,Shattuck, K. and A. West, "An investigation of phosphate based ECMP electrolyte performance on feature scale planarization", Journal of Applied Electrochemistry, 2009. 39(10), p. 1719-1724.

[24] Lin J-Y, W.A., Wan C-C J Electrochem Soc, 2008, 155, p. 396.

[25] M, F et al., "A comparative electrochemical and quantum chemical calculation study of BTAH and BTAOH as copper corrosion inhibitors in near neutral chloride solution.", Electrochim Acta, 2008. 53(28), p. 8287-8297.

[26] Shattuck, K.G et al., "Characterization of phosphate electrolytes for use in Cu electrochemical mechanical planarization", Electrochimica Acta, 2008, 53(28), p. 8211-8216.

[27] Tripathi et al., "Cu Electrochemical Mechanical Planarization Surface Quality", Vol. 156. 2009, Pennington, NJ, ETATS-UNIS, Electrochemical Society.

[28] Tripathi A, C.B., I. I. Suni, Y. Li, F. Doniant, A. Barajas, and J. McAndrew, J. Electrochem. Soc., 2008, 155, p. H918.

[29] Babu, A.J.a.S.V., “Effect of pH on chemical-mechanical polishing of Cu and Ta”, Journal of Electrochemical Society, 2004, 151, p. 709.

[30] D. Ng, T. Sen, F. Gao, and H. Liang, “Friction and Wear-Mode Comparison in Copper Electrochemical Mechanical Polishing”, Journal of the Electrochemical Society, vol. 155, pp. H520, 2008.

[31] Y. Feng, K.S.S., W. K. Teo, K. L. Tan, and A. K. Hsieh, “Corrosion mechanisms and products of copper in aqueous solutions at various pH values”, Corrosion, 1997, 53(5), p. 389-398.

[32] V. Brusic, M.A.F., B. N. Eldridge, F. P. Novak, F. B. Kaufman, B. M. Rush, and G. S. Frankel, “Copper Corrosion With and Without Inhibitors”, Journal of the Electrochemical Society, 1991. 138(8): p. 2253-2259.

[33] Y.J. Oh, G.S.P.a.C.H.C., Journal of the Electrochemical Society , 2006, 153: p. G617.

[34] Munnangi, S.S., Thesis report titled “Fabrication and testing of apparatus for Electrochemical Mechanical Polishing (ECMP) of Copper for Semiconductor applications”, 2011, Oklahoma State University, USA.

[35] Joy Marie Johnson, Thesis report titled “Modelling of advanced integrated circuit planarization processes: Electrochemical-Mechanical Planarisation (eCMP), STI CMP using Non-conventional slurries”, June 2009, Massachusetts Institute of Technology, USA.

[36] Sharan S, “Electrochemical Mechanical Planarization” US patent 7527722, 2009.

[37] I. Kobata, A. Kondera, Y. Toma, T. Suzuki, and "Electrochemical Mechanical Polishing Method and Electrochemical Mechanical Polishing Apparatus " US Patent 20090078583, 2009.

[38] M. Melleir, T .Berger, and R. Duru, "Full Copper Electrochemical Mechanical Plnanrization (Ecmp) as a technology enabler for the 45 and 32nm Nodes," 2007.

[39] I. W. Wylie and S. P. Anjur, "Electrochemical Mechanical Polishing System," US Patent 7438795, 2008.

[40] R. Fang, D. Kulkarni, and D. K. Watts, "Recycling of electrochemical-mechanical planarization (ECMP) slurries/electrolytes," US Patent 7820051, 2010.

[41] A. Fukuda, A. Kodera, Y. Toma, T. Suzuki, H. Hiyama, T. Doi, S. Kurokawa, and O. Ohnishi, "Removal Rate Simulation of Dissolution-Type Electrochemical Mechanical Polishing," Japanese Journal of Applied Physics, vol. 49, p. 076701.

[42] J. Tiley, K. Shiveley Ii, G. B. Viswanathan, C. A. Crouse, and A. Shiveley, "Novel automatic electrochemical–mechanical polishing (ECMP) of metals for scanning electron microscopy," Micron, vol. 41, pp. 615-621, 2010.

[43] S. Lee, Y. Lee, and M. Du, "The polishing mechanism of electrochemical mechanical polishing technology," Journal of Materials Processing Technology, vol. 140, pp. 280-286, 2003.

[44] I. I. Suni and B. Du, "Cu planarization for ULSI processing by electrochemical methods: a review," Semiconductor Manufacturing, IEEE Transactions on, vol. 18, pp. 341-349, 2005.

[45] A. Muthukumaran, N. Venkataraman, and S. Raghavan, "Evaluation of Sulfonic Acid-Based Solutions for Electrochemical Mechanical Removal of Tantalum," Journal of The Electrochemical Society, vol. 155, p. H184, 2008.

[46] Y. Li, "Method and Apparatus for Electrochemical Mechanical Polishing NiP Substrates," US 2010/0059390, 2007.

[47] T. Doyle and L. Karuppiah, "Platen assembly utilizing magnetic slip ring," US Patent 2006/0154569, 2005.

[48] C. M. Sulyma and D. Roy, "Voltammetric current oscillations due to general and pitting corrosion of tantalum: Implications for electrochemical–mechanical planarization," Corrosion Science, vol. 52, pp. 3086-3098, 2010.

[49] L. Sun, S. D. Tsai, and F. C. Redeker, "Method and apparatus for electrochemical-mechanical planarization," US Patent 6739951, 2004.

[50] A. Duboust, S. S. Chang, L. Y. Chen, Y. Wang, S. Neo, L. Sun, and F. Q. Liu, "Method and apparatus for face-up substrate polishing," US Patent 6776693, 2004.

[51] Z. Wang, A. Duboust, W. Hsu, and Y. Wang, "ECMP Polishing Sequence To Improve Planarity And Defect Performance," US Patent App. 20,090/061,741, 2007.

[52] V. Hardikar, "Methods of multi-step electrochemical mechanical planarization of Cu," US Patent 7468322, 2008.

[53] S. Tominaga, D. Abe, T. Enomoto, S. Kondo, H. Kitada, and T. Ohba, "Hybrid Electrochemical Mechanical Planarization Process for Cu Dual-Damascene

Through-Silicon Via Using Noncontact Electrode Pad," Japanese Journal of Applied Physics, vol. 49, p. 05FG01, 2010.

[54] S. Kondo, S. Tominga, A. Namiki, K. Yamada, D.Abe, K. Fukaya, M. Shimada, and N. Kobayashi, "Novel Electro-Chemical Mechanical Planarization using Carbon Polishing Pad to Achieve Robust Ultra low-k/Cu Integration," 2005.

[55] H. Hocheng, H. Tsai, and M. Tsai, "Effects of kinematic variables on nonuniformity in chemical mechanical planarization," International Journal of Machine Tools and Manufacture, vol. 40, pp. 1651-1669, 2000.

[56] C. E. Uzoh and J. M. K. E. Harper, "Method of electrochemical mechanical planarization," US Patent 5807165, 1998.

[57] W. G. Easter, J. A. Maze III, and F. Miceli, "Electrochemical mechanical planarization apparatus and method," US Patent 6368190, 2002.

[58] M. Zhu and W. G. Catabay, "Electro chemical mechanical polishing method and device for planarizing semiconductor surfaces," US Patent 7285145, 2007.

[59] C. E. Uzoh and J. M. K. E. Harper, "Method of electrochemical mechanical planarization," US Patent 5807165, 1998.

[60] R. Wadensweiler, A. Duboust, L. Y. Chen, M. Birang, R. Morad, and P. D. Butterfield, "Method and apparatus for substrate polishing," US Patent 6841057, 2005.

[61] M. Zhu and W. G. Catabay, "Electro chemical mechanical polishing method," US Patent 6858531, 2005.

[62] R. Mavliev, B. A. Swedek, A. N. Wiswesser, and M. Birang, "Endpoint system for electro-chemical mechanical polishing," US Patent 2005/0173259, 2004.

[63] B. M. Basol and H. Talieh, "System for electrochemical mechanical polishing," US Patent App. 20,050/173,260, 2005.

[64] B. M. Basol and H. Talieh, "System and method for electrochemical mechanical polishing," US Patent App. 20,060/006,073, 2005.

[65] A. P. Manens, "Electropolish assisted Electrochemical Mechanical Polishing Apparatus," US Patent App. 20,070/221,495, 2007.

[66] R. Jia, Y. Wang, G. J. Alonzo, Y. Hu, Z. Wang, J. Diao, S. D. Tsai, A. Yilmaz, L. Karuppiah, and L. Y. Chen, "Process for high copper removal rate with good planarization and surface finish," US Patent 2007/0235344, 2006.

[67] Kobata, Y. Toma, A. Kodera, T. Suzuki, Y. Makita, and T. Saito, "Electrochemical mechanical polishing apparatus conditioning method, and conditioning solution," US Patent App. 20,080/188,162, 2008.

[68] W. Huang and W. Lee, "Methods of Planarization and Electro-Chemical Mechanical Polishing Processes," US Patent App. 20,090/239,379, 2008.

[69] W. Lee, "Methods and Apparatuses for Electrochemical Mechanical Polishing," US Patent 2010/0116685, 2010.

[70] V. Brusic, M. F. Richardson, D. J. Schroeder, and J. Zhang, "Electrochemical mechanical polishing composition and method for using the same," US 2005/0263407, 2004.

[71] J. K. So, "Conductive polishing pad with anode and cathode," 6893328, 2005.

[72] J. G. Ameen and D. B. James, "Method for electrochemical mechanical polishing," US Patent App. 20,100/000,877, 2009.

[73] Zhenyu Lu, Seung-Ho Lee, S.V. Babu, and Egon Matijevi, “The use of monodispersed colloids in the polishing of copper and tantalum”, Journal of Colloid and Interface Science 261 (2003) 55–64

[74] P. Ahlström, A. Wallqvist, S. Engström, and B. Jönsson, "A molecular dynamics study of polarizable water," Molecular Physics, vol. 68, pp. 563-581, 1989.

[75] L. X. Dang, J. E. Rice, J. Caldwell, and P. A. Kollman, "Ion solvation in polarizable water: molecular dynamics simulations," Journal of the American Chemical Society, vol. 113, pp. 2481-2486, 1991.

[76] J. Caldwell, L. X. Dang, and P. A. Kollman, "Implementation of nonadditive intermolecular potentials by use of molecular dynamics: Development of a water-water potential and water-ion cluster interactions," Journal of the American Chemical Society, vol. 112, pp. 9144-9147, 1990.

[77] F. H. Stillinger and A. Rahman, "Improved simulation of liquid water by molecular dynamics," The Journal of Chemical Physics, vol. 60, p. 1545, 1974.

[78] Hodgson A, Haq S, “Water adsorption and the wetting of metal surfaces”, Surf Sci Rep 64, pp. 381–451, 2009.

[79] Henderson M, “The interaction of water with solid surfaces: Fundamental aspects revisited”, Surf Sci Rep 46, pp. 1–308, 2002

[80] Thiel P, Madey T, “The interaction of water with solid surfaces: Fundamental aspects”, Surf Sci Rep 7, pp. 211–385, 1987.

[81] Michael P.Allen, “Introduction to Molecular Dyanamics Simulation”, NIC Series, Vol.23, ISBN 3-00-012641-4, pp. 1-28, 2004.

[82] Godehard Sutmann, Classical Molecular Dynamics, NIC Series, Vol.10, ISBN 3-00-009057-6, pp. 211-254, 2002.

[83] Izvekov et al., “Ab initio Molecular dynamics simulation of the Cu(110)-water interface”, J.Chem.Phys. 114, 3248 (2001).

[84] G. Sutmann, "Classical molecular dynamics,” vol. 10, ed: Citeseer, 2002, pp. 211-254.

[85] C. F. Schwenk and B. M. Rode, "Extended ab initio quantum mechanical/molecular mechanical molecular dynamics simulations of hydrated Cu," The Journal of Chemical Physics, vol. 119, p. 9523, 2003.

[86] L. X. Dang and T.-M. Chang, "Molecular dynamics study of water clusters, liquid, and liquid–vapor interface of water with many-body potentials," The Journal of Chemical Physics, vol. 106, p. 8149, 1997.

[87] N. De Leeuw and S. Parker, "Molecular-dynamics simulation of MgO surfaces in liquid water using a shell-model potential for water," Physical Review B, vol. 58, p. 13901, 1998.

[88] L. X. Dang, "The nonadditive intermolecular potential for water revised," The Journal of Chemical Physics, vol. 97, p. 2659, 1992.

[89] T. P. Lybrand and P. A. Kollman, "Water–water and water–ion potential functions including terms for many body effects," The Journal of Chemical Physics, vol. 83, p. 2923, 1985.

[90] Milind Malshe, Thesis report titled “Development of interatomic potntials based on ab initio methods and neural networks for Molecular Dynamics Simulations”, 2004, Oklahoma State University, USA.

[91] Nadler et al., “First principles Molecular dynamics simulations of H_2O/Cu(111) interface”, Journal of Molecular Modeling (2012) 18, pp. 2433-2442.

[92] Toney M, Howard J, Richer J, Borges G, Gordon J, Melroy O, Wiesler D, Yee D, Sorensen L, “Voltage Dependent ordering of water molecules at an electrode-electrode interface”, 1994, Nature, 368, pp. 444-446.

[93] Schnur S, Gross A, “Propertis of metal-water interfacesstudied from first principles”, New Journal of Physics, 2009, 11,125003, pp. 1367-2630.

[94] Cooley, J.W.a.J.W.T., “An Algorithm for the Machine Computation of the Complex Fourier Series”, Mathematics of Computation, 1965, 19, pp. 297-30.

[95] Rahman A., “Correlations in the Motion of Atoms in Liquid Argon,” 1964, Phys. Rev. 136, A405.

[96] Rahman, A., and F. H. Stillinger, Molecular Dynamics Study of Liquid Water, 1971, J. Chem.Phys. 55, 3336-3359.

[97] Lionel M.Raff, “Principles of Physical Chemistry”, 1st Edition, Prentice-publication Inc, New Jersey, USA

[98] Natalia. M et al., Ab Initio Copper-Water Interaction Potential for the Simulation of Aqueous Solutions, 1993, Journal of Computational Chemistry, Vol. 14, No.6, 629-638.

[99] A Gonzalez- Lafont, J.M.Lluch, A.Olivia, and J. Bertran, 1986, Int. J. Quant. Chem., 29, 1373; A. Gonzalez-Lafont, J.M. Lluch, A. Olivia, and J. Bertran, 1986, International Journaln of Quantum Chemistry., 30, 663.

[100] Terry P. Lybrand and Peter A. Kollman, “Water–water and water–ion potential functions including terms for many body effects”, 1985, J. Chem. Phys. 83, 2923 (1985); doi: 10.1063/1.449246.

APPENDIX

ATOMIC UNIT CONVERSIONS

Time

1 *time unit* = 2.41888×10^{-17} *s*

Length

$1\ bohr\ radius = 5.29177 \times 10^{-11} m$

Energy

1 *hartree* = 2625.5 *kJ/mol*

Angle

1 *radian* = 57.295 *degrees*

Weight

1 *amu* = $1.6605 \times 10^{-27} kg$

VITA

ANANT KANDASAMY ARULMOZHI

Candidate for the Degree of

Master of Science

Thesis: EXPERIMENTAL AND MOLECULAR DYNAMICS STUDIES ON COPPER ELECTRO CHEMICAL MECHANICAL POLISHING (Cu-ECMP)

Major Field: Industrial Engineering and Management

Biographical:

Education:

Completed the requirements for the Master of Science/Arts in your major at Oklahoma State University, Stillwater, Oklahoma in July, 2011.

Completed the requirements for the Bachelor of Engineering in Mechanical Engineering at Sri Venkateswara College of Engineering, Anna University, Chennai, India in 2011.

Experience:

Graduate Research Assistant, IEM, OSU, Stillwater (Jan 2012 – July 2013)
Graduate Teaching Assistant, CEAT, OSU, Stillwater (Aug 2012-Dec 2012)
Graduate Teaching Assistant, MAE, OSU, Stillwater (Aug 2011-Dec 2011)

Professional Memberships:

Student member of Alpha Pi Mu (APM)
Student member of American Society for Mechanical Engineers (ASME)